

UNIVERSITY OF TECHNOLOGY, SYDNEY

**Design of a Parallel Shoulder Assistive Robot with  
Pneumatic Muscle Actuators**

by

Ruiyi Tang

A thesis submitted for the degree of Master by Research

in the

Faculty of Engineering and IT

Physical Human Robot Interaction Group

February 2013



## Declaration of Authorship

I, Ruiyi Tang, declare that this thesis titled “Design of a Parallel Shoulder Assistive Robot with Pneumatic Muscle Actuators” and the work presented in it are my own. I confirm that:

- this work was done wholly or mainly while in candidature for a research degree at this University
- where any part of this thesis has previously been submitted for a degree or any other qualification at this University or any other institution, this has been clearly stated
- where I have consulted the published work of others, this is always clearly attributed
- where I have quoted from the work of others, the source is always given. With the exception of such quotations, this thesis is entirely my own work
- I have acknowledged all main sources of help
- where the thesis is based on work done by myself jointly with others, I have made clear exactly what was done by others and what I have contributed myself.

Signed: \_\_\_\_\_

Date: \_\_\_\_\_

## Abstract

Given the increasing stroke incidence and ageing population, robotic assistance for people suffering from physically weak upper limbs in their activities of daily life (ADL) is becoming more promising. However, most of the current upper limb assistive robots (or upper limb exoskeletons) are bulky and heavy when designed to meet the requirements of sufficient degrees of freedom (DoFs), workspace and joint torques. The objective of this thesis is to develop dynamic models of pneumatic actuators and design a new mechanism towards developing a compact and lightweight upper limb exoskeleton, while providing proper kinematic capability to assist a human's upper limbs in their ADL.

This research first focused on parallel mechanisms given their advantages of compactness and high stiffness. Multiple parallel mechanisms are reviewed in terms of their capability in delivering 3D rotational motion and safety concerning the forces transmitted to the shoulder joint when mechanisms are applied as a shoulder joint. Then, a *3UPU wrist* mechanism is selected given its superior kinematic capability. An alternative forward kinematics solution for the *3UPU wrist* mechanism is presented so that the upper limb's orientation can be estimated using the universal joint's rotation angles on the base, rather than measuring the mechanism's limb length.

Pneumatic muscle actuators (PMAs) are then selected for driving the robotic exoskeleton because of their superiority of high strength-to-weight ratio and inherent elasticity. An enhanced dynamic force model is developed to depict the PMA's nonlinear relationship between its length, pressure and external load. By introducing a model of Coulomb friction element, this dynamic force model overcomes the problems related to the current over-simplified models. The improvement of this enhanced model is evidently witnessed in situations where softer and more elastic PMAs are pressurised to perform large contractions.

A *3UPU wrist* mechanism test rig that can measure the universal joint angles is developed for verifying the mechanism's inverse kinematics and the proposed alternative forward kinematics. Experimental results validated the inverse kinematics of this mechanism in most cases and verified the solutions of platform orientation obtained from the alternative forward kinematics. A prototype exoskeleton is developed based on the *3UPU wrist* mechanism, and is used to test the performance

of the PMAs and the *3UPU wrist* mechanism. A proportional–integral (PI) controller is used for the PMA position control. Two basic ADL movements are tested on the prototype. The experimental results and future work are then discussed.

## ***Acknowledgements***

I would like to thank my supervisor Professor Dikai Liu for his continual encouragement and belief in me, and most importantly, for his assistance throughout my course. Without his conscientious attitude and uncountable hours of intellectual interaction, I couldn't have completed this thesis.

Thank you to the rest of the team at CAS, especially the physical human robot interaction team, Marc Carmichael, Gabriel Aguirre-Ollinger and others; the weekly meetings helped me a lot in providing suggestions for problems I met during the project. Many thanks also to Chris Hamid, who worked together with me in accomplishing the mechanical parts of this project.

I extend my gratitude to the knowledgeable and obliging engineers in the FEIT faculty, Mr Chris Chapman, Mr Richard Dibbs and the UTS Motorsports Team, for their intellectual and hardware support. Thanks also to the UTS workshop who manufactured the prototype parts.

A special thank you goes to my family and close friends—my loving parents who have supported and cared for me from far away the whole time. Thank you to Mr Xiao Lan, my closest friend who supported me financially.

# Contents

<b>DECLARATION OF AUTHORSHIP .....</b>	<b>I</b>
<b>ABSTRACT .....</b>	<b>II</b>
<b><i>ACKNOWLEDGEMENTS</i> .....</b>	<b>IV</b>
<b>CONTENTS.....</b>	<b>V</b>
<b>LIST OF FIGURES .....</b>	<b>VII</b>
<b>LIST OF TABLES .....</b>	<b>IX</b>
<b>ABBREVIATIONS .....</b>	<b>X</b>
<b>NOMENCLATURE.....</b>	<b>XI</b>
<b>CHAPTER 1 INTRODUCTION.....</b>	<b>1</b>
1.1 Background .....	1
1.2 Methodology .....	2
1.3 Scope .....	3
1.4 Contribution .....	5
1.5 Thesis Outline.....	5
<b>CHAPTER 2 REVIEW OF RELATED WORK.....</b>	<b>7</b>
2.1 Shoulder Joint: Modelling, Kinematics and Kinetics.....	7
2.1.1 <i>Biomechanical Model of Human Shoulder Joint</i> .....	7
2.1.2 <i>Shoulder Kinematics and Kinetics</i> .....	8
2.2 Mechanism Design .....	10
2.2.1 <i>Serial Mechanism</i> .....	11
2.2.2 <i>Parallel Mechanisms</i> .....	13
2.2.3 <i>3UPU wrist Mechanism</i> .....	19
2.3 Artificial Muscle.....	20
2.3.1 <i>Review of Conventional Actuator and Artificial Muscle</i> .....	20
2.3.2 <i>Pneumatic Muscle Actuator</i> .....	24
2.4 Conclusion .....	28
<b>CHAPTER 3 DYNAMIC MODEL OF A PMA .....</b>	<b>30</b>

3.1	Dynamic Model .....	31
3.2	The Development of the Dynamic Model's Coefficients.....	37
3.2.1	<i>The Static Model</i> .....	39
3.2.2	<i>The Dynamic Model</i> .....	45
<b>CHAPTER 4</b>	<b>3UPU WRIST PARALLEL MECHANISM DESIGN .....</b>	<b>50</b>
4.1	Mechanism Structure.....	50
4.2	Kinematics of the 3UPU Wrist Mechanism .....	53
4.2.1	<i>Inverse Kinematics</i> .....	54
4.2.2	<i>Forward Kinematics</i> .....	55
4.3	Other Related Works of 3UPU Wrist Mechanism .....	70
<b>CHAPTER 5</b>	<b>PROTOTYPE DEVELOPMENT AND EXPERIMENTAL VERIFICATION.....</b>	<b>71</b>
5.1	The 3UPU Wrist Mechanism Kinematics Experiment .....	71
5.1.1	<i>The Test Rig</i> .....	71
5.1.2	<i>Experiments and Results</i> .....	72
5.2	The Shoulder Assistive Exoskeleton Prototype.....	77
5.2.1	<i>Overall System</i> .....	77
5.2.2	<i>Dummy</i> .....	79
5.2.3	<i>Exoskeleton</i> .....	80
5.3	Control.....	84
5.4	Position Tracking Experiment.....	86
5.4.1	<i>Preliminary Tests on 3D Rotation Capability</i> .....	86
5.4.2	<i>ADL task test</i> .....	91
5.4.3	<i>Deficiency Analysis and Possible Strategies</i> .....	98
<b>CHAPTER 6</b>	<b>CONCLUSIONS AND FUTURE WORK.....</b>	<b>100</b>
6.1	Conclusions .....	100
6.2	Future Work .....	101
<b>REFERENCE</b> .....		<b>102</b>
Appendix A	Experiments for Obtaining a Static Model for the PMA.....	112
Appendix B	Estimation Results of the PMA's Dynamic Model .....	120
Appendix C	Workspace Optimisation for the 3UPU wrist Mechanism .....	129
Appendix D	Shoulder Joint Reaction Force Analysis .....	134

## List of Figures

Figure 2-1: Biomechanical model of a shoulder joint .....	8
Figure 2-2: Examples of a serial mechanism .....	11
Figure 2-3: $nSPS + S$ mechanism and its application [45] .....	14
Figure 2-4: Actuator force analysis of $3SPS + S$ mechanism.....	15
Figure 2-5: Force on shoulder joint simulation results with/without minimising cable tensions [49].....	16
Figure 2-6: $3RRR$ mechanism and its application .....	17
Figure 2-7: $3RPS$ mechanism and its application.....	18
Figure 2-8: Structure of $3UPU$ wrist mechanism.....	20
Figure 2-9: SMA bundle actuator developed in [26].....	23
Figure 2-10: EAP actuator in the configurations of: a) roll, b) tube and c) double helix [75] ...	23
Figure 2-11: Pneumatic muscle [22] .....	24
Figure 2-12: Nonlinear processes in PM actuation [82].....	26
Figure 3-1: Schematic experimental setup .....	38
Figure 3-2: Sample response of the test with pre-set pressure of $4\text{ bar}$ , hanging weight $22.74\text{ N}$ ) .....	39
Figure 3-3: Comparison of results: experimental response (contraction length) with a pre-set pressure of $3.6\text{ bar}$ and load of $20\text{ N}$ ; the simulation results from the case with constant Coulomb friction force of $2.5\text{ N}$ suggested by [23], and the simulation data obtained by the model (Equation (3-31)).....	48
Figure 3-4: Comparison of results: experimental response (contraction length) with a pre-set pressure of $3.6\text{ bar}$ and load of $10\text{ N}$ ; the simulation results from the case with constant Coulomb friction force of $2.5\text{ N}$ suggested by [23], and the simulation data obtained by the model (Equation (3-31)).....	49
Figure 4-1: Geometry of the $3UPU$ wrist mechanism.....	51
Figure 4-2. A $3UPU$ wrist mechanism applied on a left shoulder joint after rotation .....	52
Figure 4-3: Universal joints that are capable of acquiring rotation angles.....	57
Figure 4-4: Local coordinate frame and neutral position of the $i$ th universal joint on the base .	59
Figure 4-5: Visual illustration of the passive forward kinematics approach .....	63
Figure 4-6: Geometric illustration of Scenario Two of the alternative forward kinematics .....	69
Figure 5-1: Test rig for the $3UPU$ wrist mechanism experiment .....	72

---

Figure 5-2: Calculated results of platform orientation and the measured orientation (IMU $\theta_x$ , IMU $\theta_y$ , IMU $\theta_z$ ) in the alternative forward kinematics verification test.....	77
Figure 5-3: Overall scheme of the Prototype .....	79
Figure 5-4: Structure of the 3D rotational unit emulating shoulder joint .....	80
Figure 5-5: Structure of the exoskeleton.....	81
Figure 5-6: Photo of the prototype.....	82
Figure 5-7: Assembly meeting the geometric requirements of the “3UPU wrist” mechanism ..	83
Figure 5-8: Position control scheme of the prototype.....	84
Figure 5-9: Orientation Calibration Block.....	85
Figure 5-10: Schematic diagram for the PMA PI controller test .....	86
Figure 5-11: Rotation angle in Abduction Experiment .....	88
Figure 5-12: PMA length trajectory of abduction experiment .....	89
Figure 5-13: Rotation angle in flexion experiment.....	90
Figure 5-14: PMA length trajectory of flexion experiment .....	91
Figure 5-15: Conversion of kinematic model for the prototype [32].....	92
Figure 5-16: The status value of each task in the prototype workspace .....	94
Figure 5-17: Actuator contraction response in the position tracking test.....	96
Figure 5-18: Shoulder joint angle tracking response, the red line denotes the practical response and the blue solid line denotes the desired trajectory .....	97
Figure 5-19: 3D plot of task trajectory and desired trajectory .....	97
Figure 5-20: 3D rotational unit with additional flange bearing .....	98
Figure 5-21: Pneumatic muscle contraction response after shoulder joint enhanced for task “Hand to mouth” .....	99
Figure A-1: Experimental setup of the PMA .....	112
Figure A-2: Sample data of experiments with the $\Phi 6-300\text{ mm}$ PMA .....	113
Figure A-3: $\Phi 6-300\text{ mm}$ PMA static experiment results: pressure-force relationship with different muscle length .....	114
Figure A-4: A polynomial fitting of $L_i$ , $J_i$ , $L_j$ and $J_j$ for the static model.....	117
Figure A-5: Test rig setup for the static model verification test.....	118

## List of Tables

Table 2-1: Maximum ranges of rotation and shoulder joint moments in ADL tasks.....	10
Table 2-2: Workspace of serial linked exoskeletons.....	12
Table 2-3: Comparison of actuators .....	21
Table 2-4: Quasi-static model for PMA in reviewed literature.....	25
Table 3-1: Average value of pressure for the steady-state period of each instant compressed air flow input test.....	40
Table 3-2: Average of contraction length for the steady-state period of each instant compressed air flow input test.....	41
Table 3-3a: Estimated actuation force of the PMA in the stable period calculated from group of (2.0bar, 20N), (2.8bar, 40N), (3.6bar, 20N), (3.6bar, 50N), (4.0bar, 20N) and (4.0bar, 30N).....	42
Table 3-4: Optimal coefficients of ( $N_2$ , $N_1$ , $N_0$ , $D_1$ , $D_2$ ) in dynamic force model for PMA in Equation (3-22) .....	47
Table 5-1: Test results of static replication test .....	73
Table 5-2: Calculation results of the alternative forward kinematics verification test .....	76
Table 5-3: Geometry of prototype exoskeleton .....	81
Table 5-4: Mass and moment of inertia of the platform of the prototype.....	84
Table 5-5: PID Coefficients of PMAs .....	86
Table 5-6: Reachable position condition in the prototype workspace.....	93
Table 5-7: Workspace verification result of four tasks .....	94
Table A-1: The linear fitting results of $L_i$ and $J_i$ for the relaxation process of the PMA $\Phi 6-300\text{ mm}$ .....	116
Table A-2: Coefficients of the static model for the PMA $\Phi 6-300\text{ mm}$ .....	117
Table A-3: Verification results of the PMA quasi-static model .....	119

## Abbreviations

ADL	Activities of Daily Life
CVT	Continuously Variable Transmission
DoF(s)	Degree(s) of Freedom
EAP	Electroactive Polymer
IMU	Inertial Measurement Unit
PI	Proportional–integral (Controller)
PID	Proportional–integral–derivative (Controller)
PMA/PM Actuator	Pneumatic Muscle Actuator
PWM	Pulse width modulation
ROM	Range(s) of Motion
SMA	Shape Memory Alloy
<i>2D</i>	Two dimensional
<i>3D</i>	Three dimensional
<i>3UPU</i>	Three Universal-Prismatic-Universal joint limbs (Mechanism)
<i>nSPS+S</i>	<i>n</i> Spherical-Prismatic-Spherical joint limbs plus one passive Spherical joint (Mechanism)
<i>3RRR</i>	Three Revolute-Revolute-Revolute joint limbs (Mechanism)
<i>3RPS</i>	Three Revolute-Prismatic-Revolute joint limbs (Mechanism)
<i>3UPS+S</i>	Three Universal-Prismatic-Spherical joint limbs plus one passive Spherical joint (Mechanism)
<i>3UPU wrist</i>	Three Universal-Prismatic-Universal joint limbs pure rotational (Mechanism)

## Nomenclature

### *General Style*

$\{O_A: X_A Y_A Z_A\}$  Coordinate frame with origin at point  $O_A$  and axis  $X_A$ ,  $Y_A$ , and  $Z_A$

$\dot{I}, \ddot{I}$  Differentiation and quadratic differentiation of a variable

$\vec{l}$  Vector

$\vec{l}^{\{O\}}$  Vector  $\vec{l}$  in coordinate frame  $\{O\}$

$|\cdot|$  Absolute value

$\|\cdot\|$  Vector length and normalised vector

$\angle O_1 O_A A_i$  Angle between vector  $\overline{O_1 O_A}$  and  $\overline{O_A A_i}$  at point  $O_A$

$\cdot^T$  Transpose of a matrix

$\delta L, \delta \theta$  Virtual displacement, virtual rotation angle

$\partial \theta$  Partial derivative of variable  $\theta$

$P(t)$  Variable  $P$  as a time dependent

### *Specific Symbol Usage for 3UPU Wrist Mechanism*

#### *Geometric Points*

$O, O_A, O_B$  The intersection point of the revolute pairs' axes from both the platform and the base, from the base, and from the platform in the *3UPU wrist*, respectively

$A_i, B_i (i = 1, 2, 3)$  Rotation centre of universal joints on the base and platform connected to the  $i^{\text{th}}$  limb, respectively

$O_1, O_2$  Plane centre (circular centre) of the base and platform plane, respectively

#### *Geometric Constants and Variables*

$r_A, r_B$  Length of  $|A_i O_1|$  and  $|B_i O_2|$ , respectively

$h_A, h_B$  Distance from rotation centre  $O$  to the circular centre of base  $O_1$  and  $O_2$

platform plane, respectively

$\theta_x, \theta_y, \theta_z$  Rotation angles of the platform relative to the base at point  $O$ , around  $X$ ,  $Y$  and  $Z$  axis, respectively

$\vec{\omega} = (\omega_x, \omega_y, \omega_z)$   
 $\vec{\eta} = (\eta_x, \eta_y, \eta_z)$  Angular velocity and angular acceleration of the platform

$\theta_{x_{Ai}}, \theta_{y_{Ai}}$  Rotation angles in the  $i^{th}$  universal joint on the base around axis  $X_{Ai}$  and axis  $Y_{Ai}$ , respectively

$\omega_{x_{Ai}}, \omega_{y_{Ai}}$  Angular velocity in the  $i^{th}$  universal joint on the base around axis  $X_{Ai}$  and axis  $Y_{Ai}$ , respectively

$l_i$  Length of the  $i^{th}$  limb

### ***Coordinate Frames***

$\{O_A\}, \{O_B\}$  Coordinate frame with origin at point  $O_A$  and  $O_B$ , attached to the immobile base and moving platform, respectively

$\{A_i: X_{Ai}Y_{Ai}Z_{Ai}\}$  Immobile that is attached to immobile part of the  $i$ th universal joint that is adjacent to the base.

$\{O_{Ai}: X_{O_{Ai}}Y_{O_{Ai}}Z_{O_{Ai}}\}$  mobile that is attached to the moving part of the  $i$ th universal joint that is adjacent to the base.

### ***Matrices***

$R, R_x, R_y, R_z$  Rotation matrix from platform to base, rotation matrix for around  $X$ ,  $Y$  and  $Z$  axis alone, respectively

$R_{O_{Ai}}$  Rotation matrix from coordinate frame  $\{A_i\}$  to frame  $\{O_{Ai}\}$

$R_{A_i}$  Rotation matrix from coordinate frame  $\{O_A\}$  to frame  $\{A_i\}$

$J$  Jacobian matrix

$\vec{l}_i, \vec{s}_i$  The vector representing the  $i^{th}$  limb part and unit vector in the same direction, respectively

$\Phi$  Objective function index of workspace optimisation

### ***Specific Symbol Usage for PMA***

$F(x, P)$  PMA force determined by variable contraction length  $x$  and pressure  $P$

$F_{static}(x, P)$	Static PMAA force determined by variable contraction length $x$ and pressure $P$
$F_{ce}(P)$	Force exerted by the contractile element
$F_{adjust}(x)$	Adjustment force added on static force to eliminate estimation error
$F_{coulomb}(x)$	Coulomb friction force
$F_{Damp}(x)$	Damping force
$x(t), \dot{x}(t), \ddot{x}(t)$	Contraction length, linear contraction velocity and contraction acceleration
$L(t)$	Length of the PMA
$D(t)$	Diameter of the PMA
$L_0$	Normal length of the PMA
$P(t)$	Pressure in the $i^{th}$ PMA
$K(x, P)$	Stiffness of spring element parameterised by contraction length and pressure
$K_1, K_2$	Coefficients of stiffness of spring element
$S_1, S_2, S_3$	Coefficients of passive element
$C_1$	Coefficients of contractile element
$N_1, N_2, N_0$	Coefficients of Coulomb friction force
$D_1, D_2$	Viscous damping friction force coefficient
$b$	Total length of the outer mesh threads of the PMA
$n$	Turns of threads of the outer mesh of the PMA
$\mu$	Viscosity of air gas
$v(t)$	Velocity of air



# Chapter 1 Introduction

## 1.1 Background

Physically weak upper limbs can cause numerous problems in people's daily lives. Having limited range of movement and upper limb load capability means that those affected will have trouble feeding or dressing themselves or in fetching items, making them unable to tend to their personal care needs. Stroke and ageing are seen as the leading cause of upper limb weakness. According to Lawrence et al. [1], up to 77.4% of stroke patients suffer from upper limb weakness, which makes it the most common stroke-induced impairment. A high prevalence of stroke has been estimated and reported in the Australian population, with approximately 60,000 stroke incidents estimated to have occurred in 2011 alone [2]. Moreover, the trend is for increasing prevalence of strokes, with an Australian Institute of Health and Welfare (AIHW) report [3] predicting that over half a million Australians could suffer from a stroke between 2006 and 2016. Furthermore, this is estimated to cost the Australian community \$2.14 billion each year [2]. The ageing population leads to an increase in the incidence and severity of upper limb weakness, with the majority of stroke patients (up to 80%) being aged 55 years or older [4]. As the proportion of ageing Australians increases from 13% to 30% by 2051 [5], it is estimated that there will be a considerable increase in the prevalence of upper limb weakness. As such, enhancing a stroke patient's upper limb function serves the dual purpose of improving the affected individual's personal health, as well as improving the overall health and welfare of the Australian society.

It has been found by physiologists that intensive rehabilitation at an early stage after a stroke helps to enhance the motor reflection function and strengthen the upper limb muscle, thereby effectively recovering the affected limbs [6]. However, repetitive training requires demanding and continuous supervision by therapists, and this can be a hefty financial burden for the patient. The labour-intensive work of therapy can be alleviated by assistive robots, which are introduced to take part in the repetitive rehabilitation training tasks. Researchers such as Masiero et al. [7] have used robot-assisted rehabilitation in addition to conventional therapist-assisted rehabilitation, and found that this approach resulted in less impairment of upper limb function. This shows the potential of robotic rehabilitation as a more effective rehabilitation approach for upper limb recovery training.

Conventional assistive robots [9, 10, 11] have been developed in reduced number of degrees of freedom (DoFs) for specific therapeutic training tasks, thus they can only accomplish limited motions. In addition to conventional assistive robots, full DoFs wearable exoskeleton robots [12, 13] that fully characterise human upper limb motions have been intensively researched in recent years. These robots have more DoFs and are capable of delivering a larger range of motion (ROM), thus the rehabilitation tasks can expand from simple motor function and muscle strength training to assisting people's activities of daily life (ADL). Advanced control algorithms, like force feedback interaction control [13] and electromyographic (EMG) signal-based control [14], have been developed and integrated with platforms [16, 17, 18] for various rehabilitation applications. The majority of these exoskeleton robots, however, have been designed using conventional motors and gears, in serial link configuration, and for the purpose of providing rigid motion and large forces. They are normally heavy and large in scale. In recent years, there has been a growing trend for designing compact, lightweight and affordable upper limb assistive robots, such as cable-driven and pneumatic actuated upper limb exoskeletons.

## 1.2 Methodology

The aim of this thesis is to design a lightweight and compact shoulder joint assistive robot, which can be potentially portable and mobile, and applied to assist humans in their daily lives. The main challenge in this ambition is to find a trade-off between the robot's capability and weight. In other words, it is important to have the exoskeletons satisfy the kinematic and strength requirements while still being portable and compact.

Ideally, the kinematic and strength requirements for the shoulder assistive exoskeleton should:

- (1) be able to replicate the motion and satisfy the biomechanical model of a human shoulder;
- (2) address safety issues regarding implementing the exoskeleton to assist a person's shoulder joint by reducing the resultant reaction forces applied on a shoulder joint when different mechanisms are applied;
- (3) be capable of providing a range of motion (ROM) that covers the essential tasks in a human's ADL, and a sensible torque assistance capability that is able to support at least the weight of a human arm in various gestures; and
- (4) be light and compact shoulder assistive robots.

The human shoulder joint ROM and torque capabilities are listed in Table 2-1.

For designing an exoskeleton robot that meets the requirements, several essential issues need to be addressed. As for the mechanical structure, the challenge lies in reducing the weight of the conventional serial linked mechanism. Each DoF is composed of an individual actuator and its mechanical power transmission part. Simply removing some of the bulky components inside the mechanism will weaken the system's motion ability and strength. Substituting traditional motors and gears using small, highly geared actuators is currently limited by existing motor technology. In addition, the serial linked mechanism introduces an accumulated inertia at the end effector. One solution is to use a parallel mechanism. A parallel mechanism outperforms a serial mechanism in terms of higher load-to-weight ratios, higher velocity and lower inertia. Therefore, it is regarded by some researchers as more suitable for lightweight assistive exoskeleton design [18–20].

However, problems do exist in the developed parallel mechanisms for assistive shoulder exoskeletons. Some of the exoskeletons are not capable of providing sufficient 3D rotation around the shoulder joint or they experience limited workspace, which is attributed to the parallel mechanism characteristics. As for actuators, artificial muscle actuators have been considered [21] because of their high power-to-weight ratio. McKibben pneumatic muscle actuators (PMA) are selected for use in this research as they have very good comprehensive performance among many other different pneumatic muscle actuators. According to Caldwell et al. [22], a power-to-weight ratio ranging from 1.5 kW/kg at 200 kPa to 3 kW/kg at 400 kPa is achieved using PMAs. The modelling and control issues of PMAs have been studied by numerous researchers. Nevertheless, there is still no proper dynamic actuator model that accurately estimates the contraction displacement response of a soft PMA, in which case, a more sophisticated friction force model can be used to better deal with the large underdamped displacement response because of low stiffness.

### **1.3 Scope**

The goal of this research is to develop a compact, parallel mechanism robot with artificial muscle actuation to assist a human shoulder in moving when engaged in ADL. To achieve this goal, the following research and design tasks are conducted. Firstly, an enhanced dynamic force model system for the PMAs is developed and investigated through various experiments. It is noticed that the current existing static or dynamic models oversimplified the friction component in the modelling of the PMA. In some cases (e.g. when the PMA's stiffness is low and underdamped

displacement response is likely to occur given a step initial displacement input [23]), this leads to insufficiency and relatively large errors in predicating the PMA's dynamic displacement response. As such, by integrating a more sophisticated friction element model in the dynamic force model, this research developed an enhanced model. Through calibration tests and verification processes, the enhanced model has been found to be effective in providing a more accurate displacement response than other models.

Secondly, a parallel mechanism is designed to provide 3D rotation around a fixed rotation centre to emulate a shoulder joint. The kinematics of a *3UPU wrist* mechanism is conducted. In addition, other than the conventional forward kinematics approach, we presented an alternative approach to analytically solve the forward kinematics of the *3UPU wrist* mechanism by using the angles of the joints that are connected to the base.

Finally, a test rig consisting of the *3UPU wrist* parallel mechanism and the developed PMA model is built. We applied a simple yet effective proportional–integral–derivative (PID) position tracking control to control the system. Then, two sets of full range motion (flexion and abduction) tasks were conducted to test the motion limitation of the system. Experiments to test the prototype's capability in accomplishing ADL tasks were executed as well. We firstly selected one task from four surveyed ADL tasks by comparing the proportion of each task's trajectory within the simulated prototype workspace to its full trajectory track. Since the results of the simulation and the first experimental trial were disappointing, possible factors affecting the result and the according solutions were analysed. Then a method to enhance one of the affecting factors is developed, with experimental results showing an improvement in performance.

A number of assumptions are made throughout this thesis. Firstly, the shoulder joint is simplified as a three rotational joint, and in practical presentation is consisted as a universal joint linked with a swivel ball bearing. Secondly, during the experiment, the dummy torso (where the parallel robot's base plate is attached) is considered as immovable. This means that the inertial measurement unit (IMU) sensor attached on the dummy's upper arm can measure the relative rotation angles between the dummy torso and the arm. The effect of attrition wear on the purchased PMA is neglected.

## 1.4 Contribution

The contributions of this thesis are:

- An enhanced dynamic force model of PMAs integrated with the sophisticated friction element. This model successfully reduces the response delay, and estimates the response well under the impact of varied external loads on.
- A parallel mechanical design that meets the kinematic requirements of shoulder biomechanics for building a shoulder robotic exoskeleton. Compared to serial linked robots, this has the inherent advantage of parallel mechanisms, including multiple degrees of freedom while maintaining structural simplicity, and a high level of kinematic stiffness. A way to analyse the reaction force caused by the mechanism is presented.
- An alternative forward kinematics approach, based on the angles of the universal joints attached to the base, is presented for calculating the *3UPU wrist* mechanism platform orientation.

## 1.5 Thesis Outline

This thesis is structured as follows:

Chapter 2 presents a review of related literature. By firstly investigating a human shoulder's biomechanical, kinematic and dynamic characteristics, the requirement is developed for designing a robotic exoskeleton that effectively assists the human shoulder joint. Subsequently, various preceding mechanical designs that emulate or assist a shoulder joint are reviewed.

Based on the review, a new parallel mechanism is introduced for developing the shoulder exoskeleton. The advantages and disadvantages of this mechanism are identified from the relevant literature. Various actuation techniques are also reviewed in this chapter. From this review, the pneumatic muscle (PM) actuator is considered to be a reasonable compromise between weight, size, performance and safety.

Chapter 3 presents an enhanced dynamic model for the PMA, in which the friction element in a

dynamic situation is analysed and expressed as a polynomial function. This is similar to the other elements of a PMA dynamic model. Finally, the coefficients of the enhanced model were determined through static and dynamic experiments, and then verified respectively.

Chapter 4 presents the design of a *3UPU wrist* parallel shoulder assistive robot. The *3UPU wrist* mechanism's structure and characteristics are reviewed, and then its kinematics are reviewed and studied. An alternative forward kinematics approach for this type of mechanism is presented. Then the reaction forces transmitted to the human shoulder when applying the *3UPU wrist* design are analysed. Finally, the case studies are conducted.

In Chapter 5, a test rig is firstly developed to validate the kinematics approaches of the *3UPU wrist* mechanism. Then, the design of a prototype exoskeleton is presented. After this, position tracking control schemes and the single PMA PI position controller are introduced. Finally, the prototype is tested. Based on analysis of the experimental results, possible ways to improve the performance of the prototype is discussed. The experimental results indicate that the *3UPU wrist*-based prototype is capable of accomplishing ADL tasks.

Finally, Chapter 6 presents the conclusions of this research and a discussion on future work.

## Chapter 2 Review of Related Work

To comprehend the specific requirements in developing a shoulder assistive exoskeleton, the shoulder's biomechanical models, as well as the kinematic and dynamic performance of the shoulder joint are reviewed. The related works are then discussed in two sections addressing the two essential components—mechanism and actuation.

### 2.1 Shoulder Joint: Modelling, Kinematics and Kinetics

#### 2.1.1 Biomechanical Model of Human Shoulder Joint

Anatomically, a human shoulder joint represents a complex closed kinematic chain consisting of the thorax, clavicle, humerus and scapula, and is articulated by the sternoclavicular (SC) joint, the acromioclavicular (AC) joint and the glenohumeral (GH) joint (Figure 2-1(a)) [24]. Among these joints, the GH joint delivers most of the rotational motion, and therefore the common simplified biomechanical model for a shoulder joint is analogous to a GH joint. As for the mechanical GH joint model, it is defined as a spherical joint whose rotation centre superimposes a humeral head centre [25]. Whether the GH rotation centre can be viewed as a fixed centre has been a topic of debate in recent decades. In vitro and in vivo approaches have both been applied to determine the position of a moving GH rotation centre. Multiple test results emerging from studies by Veeger [25] and Van der Helm et al. [26] suggest that the GH joint rotation centre is stabilised using muscle constraint force when the rotation is within the range of  $(-40^\circ, 40^\circ)$ , and that in a sensible range, its excursion is negligible. Large translation only occurs as described by Galinat [27] in “extreme positions or forces”, or as described by Harryman et al. [28] “because of structural damage”. However, it is also indicated that the rotation centre coincides with a humeral head centre in the sagittal plane, but it does not align well in a coronal plane [29]. Klopčar et al. [30] introduced a shoulder girdle model that moves the 3D rotation centre away from the torso to replicate this movement.

In summary, the human shoulder joint is normally modelled as a spherical joint rotating in three orientations. Whether the rotation centre is better modelled as fixed or translating in a certain pattern is still being debated. Nevertheless, a simplified biomechanical model neglecting the excursion of the rotation centre is widely used. To this end, the 3D rotation movement is the most

essential motion in a biomechanical model of a human shoulder. This is the case whether the rotation centre translates or not. The focus in this thesis is on the centre-fixed 3D rotation model as shown in Figure 2-1(b), and only the human left shoulder joint is canvassed.

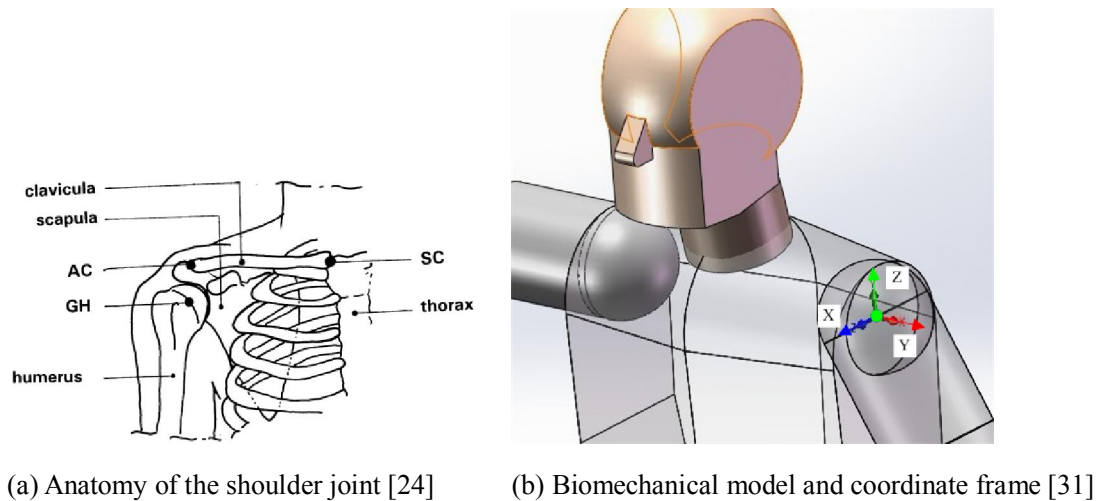


Figure 2-1: Biomechanical model of a shoulder joint

### 2.1.2 Shoulder Kinematics and Kinetics

Numerous studies have been conducted on subjects in ADL, with various recording techniques and marker positions to acquire the angle trajectory of an upper limb joint rotation [32], its range [32, 34] and anatomic limitation [34]. Unlike studies on lower limbs, which focus on gait as the main motion, the results of studies of upper limb kinematics and dynamics are task-dependent. Specific tasks generally relate to activities like feeding, hygiene, dressing, and reaching for items. Some studies even include full motion tasks, e.g. the subjects are required to move from the limit of their possible gesture in one direction to the limit in another direction [32, 35]. The recorded trajectories are translated into rotation angle trajectories by an inverse kinematics approach. This is based on the coordinate frame used in the test and the geometry. In addition, the torque capability of a human's upper limb joints was also studied in [34, 36, 37].

Since the coordinate frame in each survey is different, the presentation of joint angles is varied. In most studies anatomical terms such as “Flexion”, “Abduction” and “Shoulder internal rotation” as in Table 2-1 are used. “Flexion” indicates upper arm's movement towards anterior side of the torso [37], which is the rotation around Y axis of the immobile coordinate frame as in Figure 2-1(b) ,

“Abduction” indicates the movement away from middle line of the torso [37], it is in accordance with the rotation around X axis of the coordinate frame in Figure 2-1(b). However, “Shoulder internal rotation” indicates the rotation along upper arm’s humerus axis in the direction moving the flexed forearm towards body’s middle line, which doesn’t align with any axis in Figure 2-1(b). In this way the anatomical axis line (humerus) or middle planes (torso) of human’s parts are used in the presentation, thus it is straightforward. Nevertheless, since two different coordinate frames are involved in describing shoulder rotations (flexion and abduction in the immobile coordinate frame and shoulder internal rotation in the mobile coordinate frame), this method causes some confusion. The other type of representation describes the shoulder joint as a 3-DOF spherical robotic manipulator, of which the orientation workspace can be parameterised in various ways, such as Euler angles, unit quaternions and even a more advanced approach describing shoulder’s rotation workspace in a curved space ([38]). The method of Euler angles is applied on measuring shoulder rotations in [31]. In it the Euler angles are in the sequence of axis Y-X-Z, starting at the position overlapping the immobile coordinate frame in Figure 2-1(b).

Besides the joint trajectories, human upper limb dynamic performance in ADL was also studied by Murray and Johnson [33], Rosen et al. [31], as well as Letier et al. [36].

Table 2-1 shows the maximum angles in each rotation for each survey. The presented angles represent the mean values of all the subjects. Both ways of presenting the rotation angles are displayed in Table 2-1 accordingly. Essentially, the rotations around Y axis (1<sup>st</sup> axis) and Z axis (3<sup>rd</sup> axis) in the means of Euler angles are equivalent to Flexion and Shoulder internal rotation respectively, for their rotation axes are the same according to their definitions. The generated torque around each axis is shown; similarly, the mean value (or maximum value) in each survey is shown as well. One thing to note is that the survey results of Rosen et al. [31] adopted the means of Euler angles to present shoulder’s workspace and it didn’t specify a specific starting and ending angle.

With this transformation, we can observe a similar angle range in different surveys around each axis. Around the Y-axis, a shoulder barely moves to the back plane, while its moving forward range approximates  $-110^\circ$  ( $-108^\circ$ ,  $-111.9^\circ$ ). However, the abduction varies, and this may be attributed to the different ADL tasks from different surveys. The largest outwards abduction is  $+96^\circ$ , with Rosen et al. specifying that if the range of abduction is  $100^\circ$ , the rough range of abduction is assumed to

be ( $-4^{\circ}\sim+96^{\circ}$ ). In the axial rotation around the upper limb itself, it is easy to detect a large range in the internal rotation up to around  $-85^{\circ}$  ( $-85.9^{\circ}$ ,  $-85^{\circ}$ ), while the external axial rotation is quite limited, reaching only  $+20^{\circ}$  in one survey. Based on the preceding discussion, we summarise a set of angle ranges for the purpose of simulation in later research.

Table 2-1: Maximum ranges of rotation and shoulder joint moments in ADL tasks

Anatomical Rotations	Flexion		Abduction		Shoulder Internal/ External Rotation	
	Angle	Torque (Nm)	Angle	Torque (Nm)	Angle	Torque (Nm)
Murray & Johnson [33]	$-111.9^{\circ}\sim-14.7^{\circ}$	14.3/Null	$-20.1^{\circ}\sim-39.7^{\circ}$	- 3.7/4.2	$-85.9^{\circ}\sim-18.7^{\circ}$	3.9
Rosen et al. [31]	$110^{\circ}$	42.0	$100^{\circ}$	35.4	$135^{\circ}$	13.1
Buckley et al. [34]	$-108^{\circ}\sim-7^{\circ}$	/	$+15^{\circ}\sim+96^{\circ}$	/	$-85^{\circ}\sim+20^{\circ}$	/
Letier et.al [36]	/	10	/	9.6	/	3.1
Summarised Range	$-110^{\circ}\sim-0^{\circ}$	/	$-4^{\circ}\sim+96^{\circ}$	/	$-85^{\circ}\sim+20^{\circ}$	/
Euler Angles	Y-Axis (1 <sup>st</sup> axis)		X-Axis (2 <sup>nd</sup> axis)		Z-axis(3 <sup>rd</sup> axis)	
Rosen et al. [31]	$110^{\circ}$	42.0	$100^{\circ}$	35.4	$135^{\circ}$	13.1

As Table 2-1 shows, the mean values for shoulder torque vary considerably from one study to another, and we were unable to produce a ‘typical’ torque value. A torque value largely depends on the requirements of the task, as well as the subjects. We also noticed that the torque around the Y-axis (the flexion direction) is usually the largest compared to the other directions. This is followed by the X-axis, and the external and internal rotation torques were rated last.

## 2.2 Mechanism Design

This section discusses the mechanical design related works of the shoulder robotic exoskeletons. The essential goal of designing a shoulder exoskeleton is to replicate the 3D rotation model of a shoulder joint and to enable as much workspace close to a shoulder’s workspace as possible. The exoskeleton’s performance can be evaluated using various criteria, such as workspace, uniqueness

of the solution, the computational expense and singularities. The design also affects the weight and stiffness of the exoskeleton, partially because of the selection and arrangement of actuators and sensors. In this section, two main categories of mechanisms are discussed, conventional serial linked mechanism and parallel mechanism. The applications of these mechanisms to shoulder exoskeletons are presented. A comparative analysis is included prior to presenting a novel parallel mechanism—the *3UPU wrist* mechanism. Finally, related research is reviewed and further research options are presented.

### 2.2.1 Serial Mechanism

A serial mechanism is widely adopted in shoulder humanoid robots and exoskeletons. They usually consist of three serially connected revolute joints. By mounting three ring bearings perpendicular to each other, their axes end up intersecting at a fixed spatial point. When the axes intersection point of the mechanism is aligned with a human shoulder rotation centre, it drives the upper arm and replicates 3D rotational motion. Motors and gears are often directly mounted onto the exoskeleton and attached to each ring bearing. Figure 2-2(a) shows a typical serial mechanism design for a shoulder joint [39]. It is a 7DoF upper limb exoskeleton, among which joints 1, 2 and 3 contribute to the rotation motion of the shoulder joint. Additional to the simple spherical joint model, Carignan and Liszka [16] dealt with the translation of a shoulder joint's rotation centre. They achieved this by adding an extra revolute joint (joint 1 in Figure 2-2b) to elevate the rotation centre.

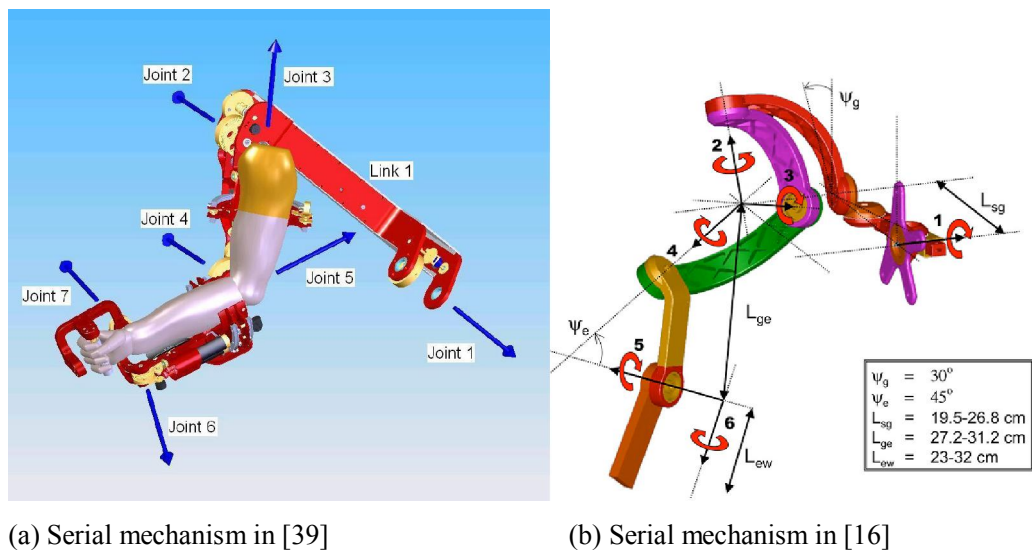


Figure 2-2: Examples of a serial mechanism

From the aspect of joint workspace, the serial mechanism is superior due to its decoupled configuration. In other words, each rotation's angle range and generated torques are determined individually by the attached motors. Thanks to the continuous rotation angle of the motors and gears, the workspace in all three directions is quite impressive. Table 2-2 lists some of the serial link shoulder exoskeletons and their workspaces.

Table 2-2: Workspace of serial linked exoskeletons

Author ( Anatomical Rotation Axis & Weight)	Flexion	Abduction	Internal Rotation	Weight
Carignan [17]	-45°~180°	-65°~90°	-30°~210°	12 kg
Nef & Riener [39]	-59°~44°	130°~50°	-60°~95°	/
Letier et al. [37]	/	/	/	6kg
Author (Euler Angle Axis \ Weight)	Y-Axis (1 <sup>st</sup> axis)	X-Axis (2 <sup>nd</sup> axis)	Z-axis(3 <sup>rd</sup> axis)	Weight
Rosen et al. [32]	180°	180°	166°	6.8 kg

Note: The flexion/abduction/internal rotation angle range only represents the joint range in corresponding exoskeletons.

'Singularity' is defined as the case when the end effector loses one or a few DoFs. Mathematically, it is defined as the occasion with a rank deficient Jacobian. In the serial linked 3D rotational mechanism, singularity takes place when the first and third joint axes align with each other. The effects of singularities can be effectively avoided when they are arranged on the edge of the reachable workspace [39]. For instance, in Figure 2-2(a), the axis of Joint 1 is aligned with the vector pointing from its origin to an obliquely upper space. In this case, singularity does not normally occur until the user's arm is raised high up or backward on the side.

The serial link mechanism can provide large joint torques compared to a human's upper limb capability. For instance, the upper limb exoskeleton developed by Carignan and Liszka [16] provides a shoulder with the torque ability of 92 Nm in each direction; whilst the human shoulder torques are normally much smaller. In Table 2-1, the maximum torques around flexion, abduction and internal rotation axis studied by Murray and Johnson in [33] are 14 Nm, 4.2 Nm and 3.9 Nm, respectively.

The weight of each exoskeleton reviewed is displayed in Table 2-2. Although the motor and gear

assembly contributes largely to the superior kinematic and torque performance in a serial linked exoskeleton, it causes issues such as big size, heavy weight and high inertia. Therefore, to compensate their large weights, the majority of upper limb exoskeletons are ground/platform mounted and powered with weight compensation algorithms [38, 17, 39]. One solution to this issue is to replace the conventional motors and gear sets with actuators of a higher power-to-weight ratio. Small and high geared actuators (such as the Harmonic Drive [41]) are adopted by several researchers [41, 9, 37] for achieving a reduced weight and high torque capacity. This method depends on the availability of a high power-to-weight ratio motor and gear sets. In addition, the effective inertia at the end effector is still accumulated as DoFs increase. An alternative strategy of improving a robot's power-to-weight ratio is to adopt a parallel mechanism [43].

### 2.2.2 Parallel Mechanisms

A parallel mechanism is regarded as being able to outperform the serial linkage exoskeleton as it can have greater stiffness, reduced inertia and most importantly, has a compact design [44]. In this section, several parallel mechanisms are reviewed in terms of their capability of delivering rotations around the shoulder joint. Existing and potential applications in shoulder assistive exoskeletons are also assessed. The ones that are capable of generating a sufficient range of motion are elaborated first, followed by their application in exoskeletons.

#### ◆ **3UPS + S Mechanism**

The  $3UPS + S$  mechanism consists of three limb actuators and an extra spherical joint connecting the base and the platform.  $3UPS$  denotes the three linearly moving components between the base and platform, denoted as the limbs.  $UPS$  stands for universal joint, prismatic joint and spherical joint, respectively, which denotes each limb's connection type on the base, the linear motion itself and the connection type to the platform. The number of DoFs of a  $3UPS$  mechanism is calculated as six (6), which means the platform can translate in three orthogonal directions and rotates around three orthogonal axes. In order to make the mechanism only rotate around a fixed point, an extra constraint is needed. Therefore the “+  $S$ ” joint is applied and denotes one extra spherical joint, which directly links the base and the platform.

Since the “+  $S$ ” passive spherical joint is analogous to the human shoulder's biomechanical model,

the  $3UPS$  mechanism can then be adopted as an exoskeleton for the shoulder. While realistic exoskeletons were not found in the literature, the  $3UPS + S$  mechanism is still the basis for the  $nSPS + S$  mechanism to be discussed below.

#### ◆ $nSPS + S$ Mechanism

The  $nSPS + S$  mechanism is essentially equivalent to the  $3UPS + S$  mechanism. It is for the particular case of using cable as the actuation. The difference is that the universal joint on one end of each limb actuator is replaced by a spherical joint. The purpose of this is to enable the one extra passive DoF for the cable to rotate around itself. The reason for using “ $n$ ” ( $n \geq 3$ ) limbs (i.e.  $nSPS$  instead of  $3SPS$ ) is because cable actuation can only perform tension rather than a pushing force, and the redundant actuators cover more workspace. The application of the  $nSPS + S$  mechanism can be found in exoskeletons of [44, 45, 46]. In the test rig built in [46], a ball socket joint is used to represent the shoulder spherical joint, and six cables are used to pull the upper arm rotating around the ball socket joint. In the test rig built in [45], a customised universal joint is serially linked to a revolute flange to consist a 3D rotational joint as the “ $+S$ ” passive spherical joint in the mechanism. Encoders are mounted on both the customised universal joint as well as the revolute flange to record the rotation angles, which are used as the feedback in position tracking control. Four cables are used to generate shoulder rotation. Given its straightforward and compact design, the  $nSPS + S$  mechanism has been intensively studied and applied in exoskeletons, like in [43, 46]. The kinematics and workspace optimisation were solved in both designs.

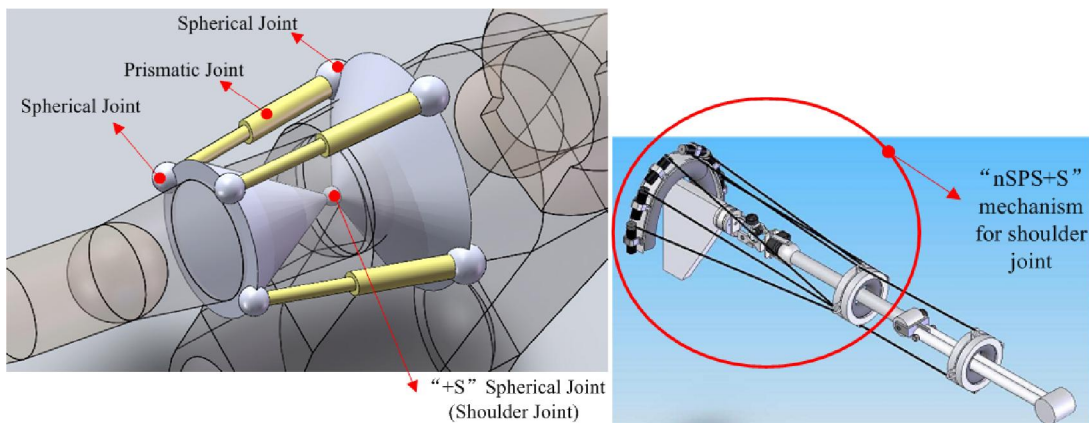


Figure 2-3:  $nSPS + S$  mechanism and its application in [45]

However, the passive “ $+S$ ” spherical joint in these designs brings about safety issues on the

human's shoulder joint, which is caused by the reaction forces acting upon the shoulder joint. This critical issue in the  $nSPS + S$  mechanism makes it more suitable for humanoid robots, rather than shoulder assistive exoskeletons. As mentioned, the  $3SPS$  mechanism [19, 44] or the equivalent  $3UPS$  [47] mechanism alone, is an underactuated parallel mechanism [18], i.e. the number of actuators (in this case the number of limbs), which equals three, is less than the DoFs of the platform, which is six. Therefore, an extra “+  $S$ ” (spherical) joint is applied to constrain the platform rotation around one point [19, 20], thereby reducing the DoFs to three. (shown in Figure 2-3 ) Consequently, the spherical joint bears and absorbs forces from the actuators that tend to move it away from its original position. As illustrated in Figure 2-4, the actuator force  $F_i$  is presented as  $F_{ir}$  and  $F_{it}$ . Force  $F_{ir}$  acts to rotate the lower part (platform) around the passive shoulder joint (the “+  $S$ ” joint), and force  $F_{it}$  passes through the “+  $S$ ” joint, thus moving the passive spherical joint along the direction of the force  $F_{it}$ . The composition of force  $F_{it}$  from all the actuators does not necessarily cancel each other out. In addition, in the cable actuation case, where all the actuators are delivering pulling forces, the “+  $S$ ” joint bears a resultant force of  $F_{it}$  that tends to push it to the direction of the base. This resultant force makes the human's shoulder joint move against human anatomy, thus causing safety concerns.

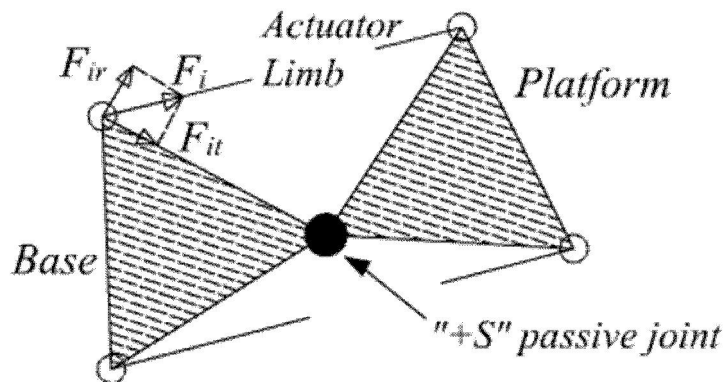


Figure 2-4: Actuator force analysis of  $3SPS + S$  mechanism

As a matter of fact, Agrawal and his team developed a control algorithm aiming to alleviate the negative impact of the force acting on the shoulder joint. In [49], a scheme for trajectory planning and control that minimises the reaction joint force was presented. As the simulation results in Figure 2-5 show, the reaction force on the shoulder joint with minimising cable tensions (red line in the graph) is lower compared to forces without minimising cable tensions. In this case, starting

from 5 seconds, the cable tension minimisation optimisation began to be effective in reducing around 25% of the original reaction force on the shoulder joint.

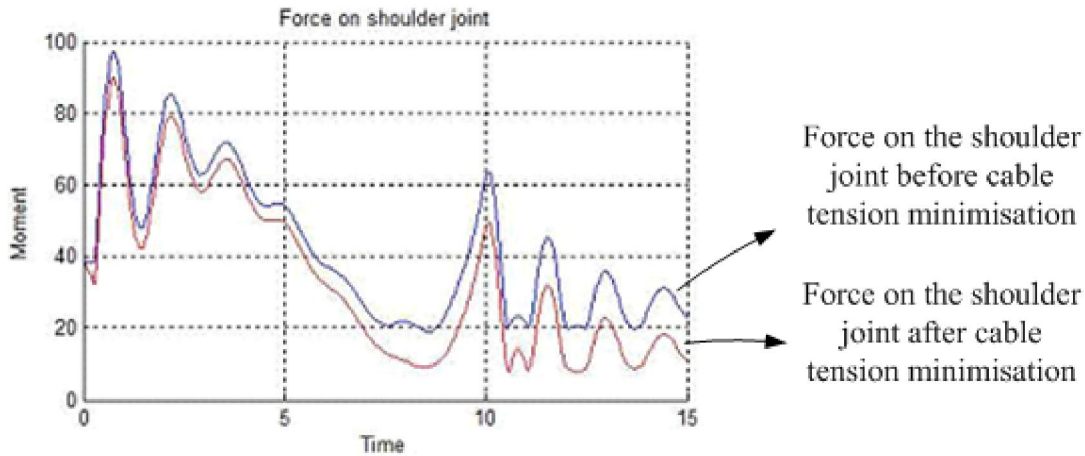


Figure 2-5: Force on shoulder joint simulation results with/without minimising cable tensions [49]

Moreover, one way to measure shoulder rotation angles is to use three encoders coupled with the universal joint and revolute flange. This way may not be practically feasible when the mechanism is applied on the human shoulder because the encoders cannot be mounted. Thus, a non-intrusive measuring approach is needed. Alternatively, in the exoskeletons presented in [18] and [45], cable lengths can be recorded, thus forward kinematics can be implemented to estimate upper limb orientation. The shoulder rotation angles are usually calculated numerically [26, 48].

Due to the above reasons, although the  $nSPS + S$  or equivalent  $3UPS + S$  mechanism is able to deliver 3D rotation around the shoulder joint, we found them more suitable for humanoid robots, rather than for shoulder assistive exoskeletons.

#### ◆ **3RRR Mechanism**

The  $3RRR$  (i.e. three limb revolute-revolute-revolute) parallel mechanism is found to be able to meet the requirement of generating 3D rotations around a fixed rotation centre. It was also called agile eye, initially introduced by [51] for camera positioning devices. This mechanism also consists of a base, a platform and links between them. The connection types of all the three limbs are revolute-revolute-revolute joints, making three revolute joints in one limb and nine revolute joints

in total for three limbs. The total number of DoFs of this mechanism is three [17]. The conditions for this mechanism to perform pure rotation around a space point are that: the axes of all the nine revolute joints have to converge at one point in space, and the converging point is the rotation centre of the platform [17]. The  $3RRR$  parallel mechanism has been adopted in the “REACH” exoskeleton in [17]. As illustrated in Figure 2-6(a), each limb consists of two braces rotating around each other through a revolute joint. Both braces are connected to the base and platform also by revolute joints, thus making it a  $3RRR$  mechanism. Optimisation for preventing singularity was performed, and a continuously variable transmission (CVT) actuation system is developed to drive each limb’s revolute joint (Figure 2-6(b)). This mechanism shows potential in generating 3D rotation around the shoulder joint, and the CVT actuation system is promising in terms of providing stiff yet inherently safe actuation. However, due to the CVT system used, the exoskeleton is still heavy and bulky. In addition, multiple collision conditions in the workspace have to be addressed.

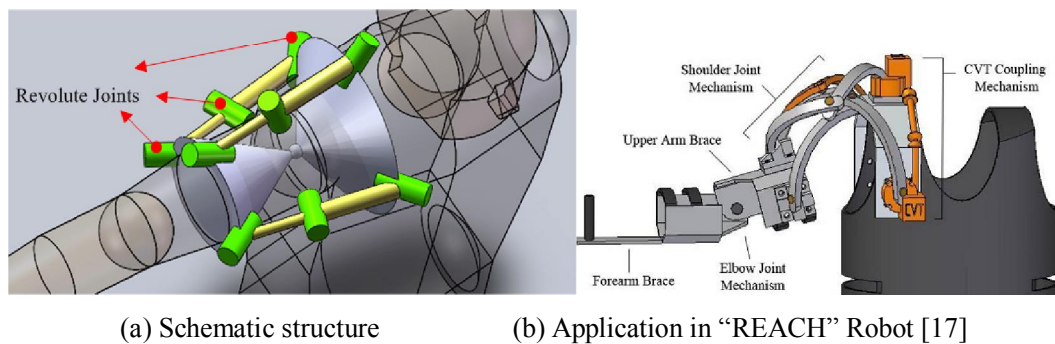


Figure 2-6:  $3RRR$  mechanism and its application

#### ◆ $3RPS$ Parallel Mechanisms

As previously demonstrated, the  $3UPS$  ( $nSPS$  in the cable drive scenario) parallel mechanism is underactuated. Its platform has six degrees of freedom and there are only three linear actuators (“ $P$ ” joint, the prismatic joint) to drive the robot. To modify it so that the mechanism’s DoFs is reduced to three, we could either replace the “ $U$ ” (universal joint) with “ $R$ ” (revolute joint) to acquire the  $3RPS$  mechanism, or replace the “ $S$ ” (spherical joint) with “ $U$ ” (universal joint), obtaining a  $3UPU$  three DoF system.

Jeong et al. presented a  $3RPS$  (three limb revolute-prismatic-spherical) shoulder exoskeleton in [20] (Figure 2-7(b)). It features one DoF in translation and two DoFs for rotation around the human

shoulder joint. The 2DoFs rotation allows the upper limb to reach a desired point in Cartesian space, and the 1DoF translation helps the exoskeleton to be adjusted to fit each individual in the axis perpendicular to the lateral section of a human. In their research, workspace optimisation was performed in the design process to obtain optimal geometric parameters, and finally a pneumatic cylinder actuated prototype was tested.

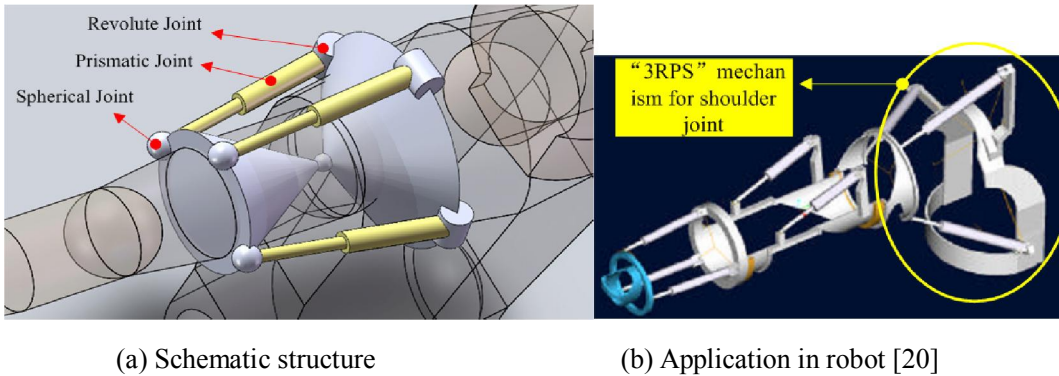


Figure 2-7: 3RPS mechanism and its application

#### ◆ Other Parallel Mechanisms

Other parallel mechanisms include: the truss 2DoF design in the wearable robot Pneu-Wrex in [10], in which 1DoF is lacking; and the BONES system [43] which acquired sufficient DoFs and range of motion, as well as good dynamics control. However, the BONES design requires a complex base structure and specially designed spherical joints to support the pneumatic cylinders.

In summary, both the  $3SPS + S$  and the  $3RRR$  mechanisms have full three degrees of freedom and can be designed to reach sufficient range of motion in three orientations. The  $3SPS + S$  mechanism has the problem of generating harmful forces on the shoulder that is not in accordance with human's natural movement. The  $3RRR$  mechanism has been successfully developed as a shoulder exoskeleton, yet multiple collision conditions in the workspace needs to be solved. Kinematic and dynamic performance evaluation of three DoFs rotational parallel mechanisms ( $3RRR$ ,  $3UPU$  wrist and  $2UPS-IRU$ ) are presented by Saltaren et al. in [52]. Among the three mechanisms,  $3UPU$  wrist was believed to have achieved the best workspace performance, and  $3RRR$  surpasses it in dynamic performance such as maximum torque and dexterity.

### 2.2.3 *3UPU wrist Mechanism*

The pure rotational three DoFs *3UPU* (three limb universal-prismatic-universal) mechanism called *3UPU wrist* [53] was introduced by Karouia and Herve in 2000. This mechanism has two geometric conditions so that it can rotate around a fixed point. The first condition is that each axis of the six universal joints (axis  $Y_{Ai}$ ,  $i = 1, 2, 3$ ) all intersect at point  $O$  in space, as illustrated in Figure 2-8. The second condition is that the other revolute axis ( $X_{Ai}$ ,  $i = 1, 2, 3$ ) in each universal joint must be parallel with the one on the other end of the connected limb ( $X_{Bi}$ ,  $i = 1, 2, 3$ ). For example, in Figure 2-8, axis  $X_{Ai}$  is parallel with  $X_{Bi}$ .

Similar to other parallel mechanisms, the inverse kinematics of the *3UPU wrist* mechanism is straightforward and uniquely determined. The solutions for forward kinematics were also presented in analytical forms in [44] and [54]. In other words, the forward kinematics of this mechanism does not require expensive numeric calculations to obtain a unique solution. Singularity condition is discussed in [55] and [56]. An inverse dynamic method was presented in [56]. The *3UPU wrist* mechanism was compared with the other two rotational mechanisms in [52] in terms of workspace and dexterity; the conclusion was that *3UPU wrist* achieves the best workspace performance but the singularity problem needs to be addressed.

To the author's knowledge, this mechanism has not been applied in exoskeletons before, nor is there a practical prototype of this mechanism. Given the advantage of this mechanism's capability in generating 3D rotation around a rotation centre, as well as its workspace performance [52], the *3UPU wrist* mechanism is adopted in this thesis and developed as the mechanism for the shoulder assistive exoskeleton.

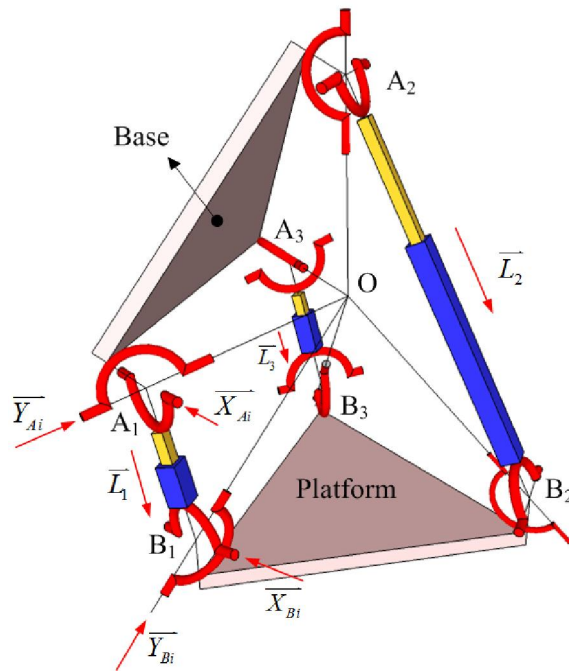


Figure 2-8: Structure of 3UPU wrist mechanism

## 2.3 Artificial Muscle

### 2.3.1 Review of Conventional Actuator and Artificial Muscle

Actuators provide moving power for the exoskeleton. Besides force (torque) capability, the actuator's weight, size, controllability, as well as safety performance, are all crucial factors in selecting and evaluating actuators.

In Table 2-3, conventional actuators, such as motor and gear train systems, pneumatic actuators, and some newly introduced artificial muscle actuators are compared. In the table, SMA stands for shape memory alloy [57], EAP stands for the electroactive polymer actuator [58], and PM stands for pneumatic muscle [59].

Table 2-3: Comparison of actuators

Actuations		Power-to-weight ratio (W/kg)	Stroke	Operating Speed	Compliance	Actuator model and parameters for control
DC Motor <sup>[60]</sup>		100–200	Infinite	Fast(thousands rpm)	No	Linear model, voltage
Pneumatic Cylinder <sup>[60]</sup>		50–100	<100%	Typical 1m/s	No	Linear model, pressure
Artificial	SMA <sup>[61]</sup>	3500	< 8%	1Hz [62]	/	Nonlinear model, temperature
Muscle	EAP Material <sup>[61]</sup>	Up to 3500	> 300%	in milli-seconds	Yes	Nonlinear model, Voltage
	PMA <sup>[63],etc.</sup>	1500~3000	25%~35%	1 ~ 10Hz [59]	Yes	Nonlinear model, pressure

In Table 2-3, the index power-to-weight ratio is calculated as generated torque divided by the actuator's weight. For electric motors, the weights of both motors and reduction gear trains are accounted. For pneumatic cylinders, the weight of the pneumatic cylinder and the additional pneumatic valves units are considered. Although it is evident that the artificial muscle group has better performance in power-to-weight ratio than conventional DC motors do, it is believed that only the material of these artificial muscle actuators are accounted.

Stroke denotes the working distance of each actuator, thus affecting the exoskeleton's workspace. Motor and gear trains have the best stroke. Inherent compliance describes an actuator's capability of passively absorbing external shock and forces, which is an important characteristic in evaluating the actuator's safety performance. Thanks to their soft and resilient materials, EAP and PMAs have intrinsic compliance. For other actuators, variable stiffness actuation should be developed for safe human robot physical interaction because it helps to diminish unwanted large shock forces and to restore forces [64]. Also, in some cases such as walking, compliant actuation is able to adapt to various operation conditions and provide assistance in a more natural way. Conventional motor and gear train systems are built as stiff as possible in order to provide fast and accurate position. There have been research works in developing stiffness variable control on conventional actuators. Active compliance is introduced to measure output force and apply compliant control strategy in the controller [65], but it has the problem of continuous energy dissipation. Impedance control acquired some success in [66]; however, it requires complex control and the cost is high. Serial elastic actuators are developed in [67]; it serially links a spring to a stiff actuator, but the system stiffness is a constant which is determined by the attached springs. Other mechanical structures or adjustable

stiffness were introduced in [64] and [68]. Overall, it is considered that conventional actuators and control systems developed for these actuators to achieve compliance are not suited for lightweight and compliant assistive shoulder exoskeletons because of their low power-to-weight ratio, complex gear train system, and the additional components required to produce variable stiffness. Therefore, artificial muscles are considered more suitable for assistive shoulder exoskeleton development. Three categories of artificial muscles are reviewed in this section.

There has been controversy on the weight advantage of PMA over conventional motors and gears when the weight of pneumatic devices such as valves, regulators and air compressors are included. Tavakoli and etc. argued in [42] that based on their experiment on the developed serial linked manipulators, providing the same angle and torques, the weight difference between PMA (together with pneumatic valves, regulators and controller) and DC motors and gears is small, and that given the poor control of PMA, it is not favourable. On the other hand, many research works have demonstrated their compact and light weight robot designs with PMA and related compressed air devices and sources. In [69] a specially designed lightweight unit of pressure regulator, pressure sensor and valves as well as controllers is introduced to control the humanoid upper limb robot, which makes the total weight of the upper limb only about 1.8kg. As for the PMA actuated humanoid infant robot developed by Kobayashi in [70], which has multiple joints and degrees of freedom, the total weight is 3.9 kg, which even includes a CO<sub>2</sub> cartridge as compressed air source. To summarise the comparison between conventional DC motors and PMA, both actuators can be properly designed to be lightweight and compact to drive robots. PMA's power to weight ratio advantage becomes more obvious with the increase of the number of DOFs, because the weight (and inertia) of DC motors and gear trains for more DOFs accumulates much faster than the weight of PMA and compact valves.

As illustrated in Figure 2-9, SMA (shape memory alloy) [67, 68, 69] is a special shape memory metal that contracts and provides constant force when heated. It has the advantage of being extremely compact. The disadvantages of current SMA actuators are the very small stroke (10% contraction rate), limited actuating force, and the issue of providing a practical cooling system. For example, the 150 micron wire on the humanoid robot in [72] can only lift one pound in weight. Larger amount bundles can produce power that multiplies; however, the cooling condition of each wire in a bundle varies, which makes it impossible to control. Furthermore, the inherent compliance

of SMA is not comprehensively studied.

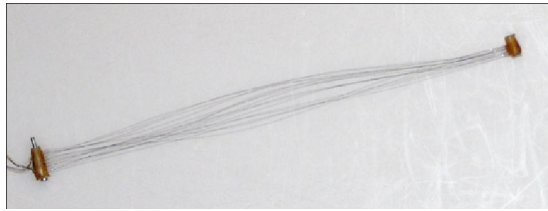


Figure 2-9: SMA bundle actuator developed in [26]

Electroactive polymer (EAP) actuators are made by smart polymer material that changes its shape when applied with transient high voltage excitation. The index of characteristics shown in Table 2-3 reveals the superiority of this smart polymer material. Nonetheless practical performance of each EAP actuator depends on its type and manufacturing in various configurations. Figure 2-10 shows the material in a roll, tube and double helix configuration. Currently EAP based actuators are still at research stage and are only manufactured in labs. EAP macroscopical applications [70, 71, 72] validated EAP's potential for use in exoskeletons. For example, in [74], a finger force enhancing device was developed. It exerted forces under 10 N with high voltage excitation between 1 kV and 6 kV produced by miniature DC to high voltage converters. The drawback of this actuator is the requirement of high voltage (up to several kilo voltages) for actuation.

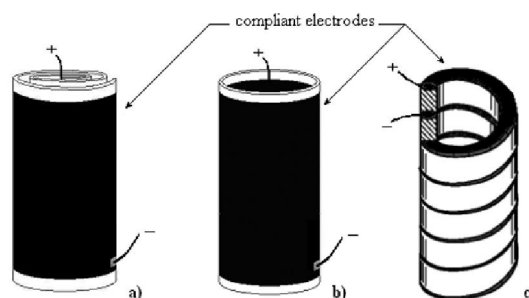


Figure 2-10: EAP actuator in the configurations of: a) roll, b) tube and c) double helix [75]

Pneumatic muscle (PM) has the advantage of high power-to-weight ratios, inherent safety, low cost and light weight. It can be coupled to the joint or mechanisms directly, thus no complex power transmission gears are required. The drawbacks with PMs are the nonlinear force-length performance, long response time and hysteresis.

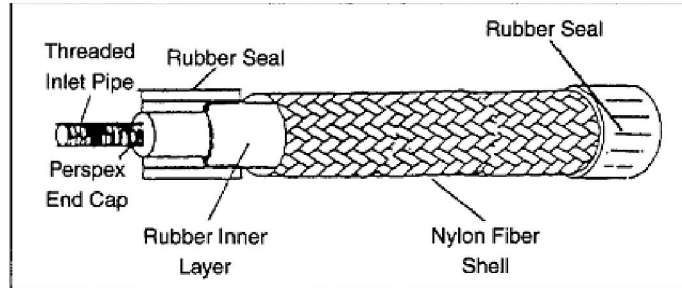


Figure 2-11: Pneumatic muscle [22]

### 2.3.2 Pneumatic Muscle Actuator

The McKibben type PMA was introduced in the 1950s [76]. As Figure 2-11 shows, it consists of an inner expandable rubber tube covered by an outer braided mesh sheath. One end is crimped as a dead end, and the other end connects to an air inlet hose. When compressed air is charged into the inner rubber tube, it expands and pushes the outer braided sheath in a radial direction, and contracts in the axial direction. Therefore, a pulling force along the PMA is generated. As Section 2.3.1 states, the PMA is found to be comparatively more effective and powerful among all the artificial muscles. However, modelling the PMA is a challenge because of its nonlinear characteristics. In order to drive the shoulder assistive exoskeleton to a desired position or pose, an accurate model which can predict the PMA's contraction length is needed. The PMA models generally fall into two categories: the quasi-static model and the dynamic model.

The quasi-static model describes the nonlinear relationship between the PM's length, inner pressure and the contracting force. This nonlinear relationship can be derived from the virtual work principle, as stated in [59]. The output work, i.e. the work done by contraction force alongside the PMA's axis, equals to the input work which is the work done by the pressure pushing on the surface of the inner tube. This relationship is expressed in Equation (2-1), in which  $F$ ,  $dL$ ,  $P'$  and  $dV$  stand for the contraction force, transient contraction length, pressure and transient volume change, respectively. The left part of the equation represents the output work and the right part represents the input work.

$$-FdL = P' dV \quad (2-1)$$

This analytical model cannot accurately predict the nonlinear relationship. The derived theoretical models [59] and [77] either produce results that deviate from practical results or contain too many

geometrical parameters that are impossible to correctly measure. Therefore, empirical quasi-static models are often used based on the tested PMAs. Some researchers made amendments to the analytical models. For example, [78] introduced a correction factor to determine the practical force as a percentage of the calculated theoretical actuation force. This correction factor is related to the inner pressure. In [77], some parameters that take into account the non-cylindrical shape on the two ends are suggested, and it is stated that the force model was improved. Recently, the quasi-static force model was assumed as a simple polynomial function of length and pressure [76, 77, 78]. Then multiple experiments were conducted with various lengths and pressures. With recorded force, length and pressure values, the unknown coefficients in the polynomials were determined. Table 2-4 shows some of the empirical models. It is believed that few of these models can be used to accurately represent the force, length and pressure relationship of the PMA. For different PMAs, experiments are needed to determine the coefficients of the models. It is observed that, except for the model in [81], in other models, the variable  $P(t)$  (pressure) always has a linear relationship with  $F(t)$  (force). This is in accordance with the theoretically derived expression of force in [59]. In the experiments in Section 3.1, this linear relationship between pressure and force is utilised.

Table 2-4: Quasi-static model for PMA in reviewed literature

Researchers	Model
Colbrunn et al. [78]	$F(P_g, L) = \frac{P_g(t)b^2}{4\pi n^2} \left( \frac{3L(t)^2}{b^2} - 1 \right) \cdot \text{Eff}(P_g(t)) + F_{\text{max limit}} \text{ if } (L(t) > L_{\text{min}}) \quad (1)$
Tondu and Lopez [77]	$F(\varepsilon, P) = (\pi r_0^2)P(t)[a(1 - \varepsilon(t))^2 - b] \quad (2)$
Pujana-Arrese et al. [80]	$F(P, q) = (D_1 + D_2 \cdot q(t) + D_3 \cdot q(t)^2)P(t) + \varphi(q(t)) \quad (3)$
Wickramatunge and Leephakpreeda [81]	$F_{\text{elastic}} = K(P, L_s)L_s; \quad K = a_0P^2(t) + a_1P(t)L_s(t) + a_2L_s(t)^2 + a_3 \quad (4)$

(1).  $F(P_g, L)$  is a function of Pressure  $P_g(t)$  and length of the PMA  $L(t)$ .  $L_{\text{min}}$  is the minimum contraction length of the PMA,  $F_{\text{max limit}}$  is the maximum force the PMA generates given the pressure. Constants  $b$  and  $n$  indicate geometric constants related to the actuator.  $\text{Eff}(P_g(t))$  is an empirical function to amend the theoretical model to practical performance.

(2).  $F(\varepsilon, P)$  is a function of pressure  $P(t)$  and contraction ratio  $\varepsilon(t)$ ,  $r_0$  is the radius of the PMA when it's at resting status. coefficients  $a$  and  $b$  are constants that are empirically determined to make the model applicable on particular PMAs.

(3).  $F(P, q)$  is a function of pressure  $P(t)$  and contraction ratio  $q(t)$ ;  $D_1, D_2$  and  $D_3$  are empirical coefficients.  $\varphi(q(t))$  is an amendment function to cancel off the passive forces in the PMA.

(4).  $F_{\text{elastic}}$  is a function of pressure  $P(t)$  and Stretched length  $L_s(t)$ ,  $a_0, a_1, a_2, a_3$  are experimentally obtained coefficients.

The dynamic model of the PMA is more complex. It can be defined as the relationship of force, pressure and length in the transient state. Besides the quasi-static model, coulomb friction and viscous friction forces are accounted for in the dynamic model. The dynamic model can also be described as the integrated effect of several major nonlinear processes in the dynamic case. One nonlinear process is the PMA model with coulomb friction and viscous friction. Another process is the pressure dynamically affected by an air bladder and air flow dynamics. These two nonlinear processes are expressed by the Air Bladder model and Valve Flow Rate model. In this way, the inner pressure of the PMA can eventually be estimated by the on and off time of the solenoid valve, or by the proportion of open area of the proportional valve. These nonlinear processes are integrated in the way described in the following diagram (Figure 2-12) [82].

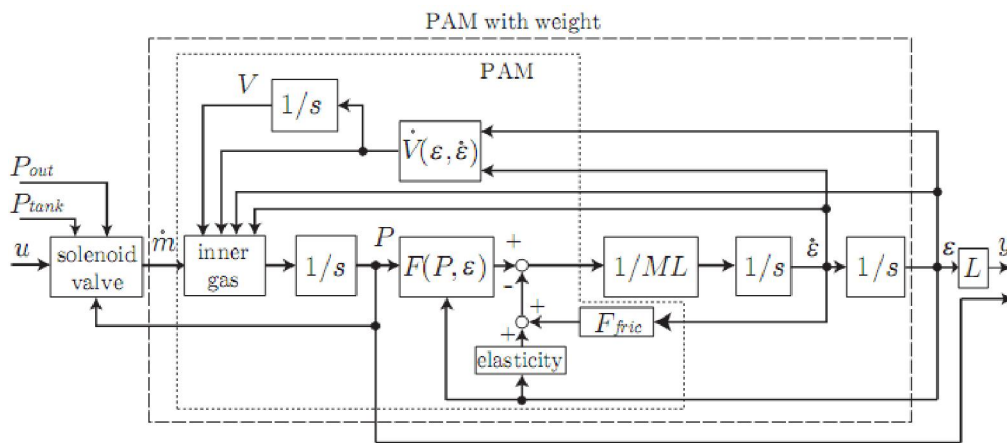


Figure 2-12: Nonlinear processes in PM actuation [82]

In this thesis, the PM dynamic model only refers to the nonlinear relationship between PMA length  $L(t)$  and its internal pressure  $P(t)$ :  $F(L, P)$ . Other nonlinear elements (as shown in Figure 2-12) have been well studied in pneumatic theories and will not be discussed in this thesis.

The dynamic model of the PMA is tested in various ways. [82] and [83] simply used the empirical quasi-static model as the transient dynamic model without considering the friction forces. Given the instant flow of compressed air by turning on the solenoid valve, the simulation results of contraction length versus time and pressure versus time, from the integrated dynamic model were found in coincidence with the practical test result. The contraction length delivered an overdamped response and took around 20 seconds to settle. Actually, in the lower frequency scenario, it was found that friction forces can be neglected. In [81], Wickramatunge and Leephakpreeda developed

an empirical quasi-static model and tested this model by changing the pressure variable in the model. The test results showed an almost coincidence contraction length response between the simulation and practical results during a period of about *1.5 seconds*. In [78], Colbrunn et al. developed a PM dynamic model on the modified quasi-static model and introduced a constant viscous damper. Colbrunn et al. performed a constant air mass test, in which the integrated model of air bladder process and PM dynamic model were simulated and tested, rather than the PM dynamic model alone. It was found that the results match in frequency at the beginning of movement, but as time elapsed, the displacement deviated from the test results. This test is one of the few experiments that tested the PMA dynamically at a high frequency of around *5 Hz*. Reynolds et al. [84] proposed a simple three element dynamic model that consisted of a contractile force element, a spring element and a damper element. These three elements are assumed to relate to pressure only. The corresponding coefficients were determined by using experimental results. A test with the input of instant provided compressed air flow and a test with triangle signals of pressure were carried out. The results proved this model's validity. However, there is an average error of around *15%* in position estimation, given the low frequency of around *0.2 Hz*. In [85], Balasubramanian et al. argued that Reynolds et al.'s three element model needs justification on its variation with external load and on the assumption of only pressure-related coefficients in the model. They then quantified the dynamic displacement response of the PMA given instant compressed air flow input, and created a map of the corresponding "damping ratio" as well as "natural frequency" of the constant weight displacement response at a given load and pressure values.

In the test of a 6 mm diameter PMA in [23], a constant weight was hung on the PMA and the inlets, and the outlets were sealed to create a constant air mass environment. An underdamped contraction length response was produced after the given initial displacement. The obtained model failed to accurately replicate the actual response. Despite the fact that "the frequency of estimated and actual displacement response was in good agreement" ([23]), the model failed to accurately, completely estimate the impact of friction forces on contraction length response, nor is there any discussion on this model's adaptability in simulating the response of varied external loads.

In summary, the current developed PM dynamic models can depict the inherent characteristics of a PMA; however, they are oversimplified, which lead to discrepancies between the experimental

response and estimation results.

Moreover, it was observed by the author that the opening of the valve has considerable effect on the dynamic performance of contraction length. In general, a small opening of a valve makes the PMA respond slowly. When the valve is fully opened for even in a short time period, it causes the length response to oscillate for a long time. Therefore, in order to achieve a smooth and fast response, an optimal valve area in accordance with the selected PMA's volume needs to be found.

A wide variety of control approaches were discussed for control of the PMA response. Simple proportional–integral (PI) and proportional–integral–derivative (PID) were widely adopted in counter-balanced configurations [86]. In order to compensate for nonlinearities, computational methods are integrated with traditional linear control methods. Carbonell et al. introduced the gain scheduling method [87]. Fuzzy PID was also adopted by the same team in [88]. Chan et al. developed a sliding mode control for an antagonistic PM pair [89], while Shen introduced the same method for a single PM [90], and Thanh and Ahn discussed the PID controller with neural networks [91]. As the control results vary with different coefficients, different dynamic frequencies and other uncertain factors, an overall comparison simply based on a mathematical model simulation is not realistic [92]. From the comparative experimental study presented in [92], it was argued by Chillari et al. that PID feedback control with pressure signal as a reference is a good choice.

## 2.4 Conclusion

This chapter firstly discussed the biomechanical model of the human shoulder joint, which can be simplified as a spherical joint. Then, the workspace and torque capability of a human shoulder joint is reviewed as a reference for the kinematics and actuation requirement for the design of a shoulder assistive exoskeleton. Next, the mechanical design of previously developed exoskeletons is discussed. The pros and cons of both serial and parallel linkage mechanisms are also reviewed. To find a compact and lightweight mechanical design that emulates 3D rotational motion around the shoulder, several parallel mechanisms are compared, and their application analysed. Consequently, a *3UPU wrist* parallel mechanism is selected for use in the design of our shoulder assistive exoskeleton.

Various actuation technologies were reviewed. Subsequently, artificial muscle was found to

outperform conventional actuators in terms of higher power-to-weight ratios and safety. Out of the three mature artificial actuation technologies, pneumatic muscle was selected for our exoskeleton. Several PMA models are reviewed and it was concluded that there is still a lack of proper dynamic PM model that can accurately predict the dynamic response.

## Chapter 3 Dynamic Model of a PMA

This chapter presents a methodology for developing an enhanced dynamic model for a PMA. A dynamic model of a PMA characterises the relationship of multiple variables such as inner pressure  $P(t)$ , contraction length  $x(t)$  and dynamic force  $F(t)$  as  $F(x, P)$ . As was discussed in Chapter 2, developing a generic theoretical dynamic model of a PMA is a challenge mainly because many geometric parameters are not easy to get (such as the outer mesh's thread length and turns). Alternatively, various polynomial-based empirical models or empirically modified theoretical models have been developed, such as quasi-static models [79–81] and dynamic models [81].

A dynamic model that can accurately predict the PMA's response in various cases is important in dynamic control. To verify the accuracy of dynamic models, one approach is to make one variable in the nonlinear model  $F(x, P)$  a constant value, and then apply either a step change or a sophisticated signal like sinusoidal signal to another variable in the experiments as in [59]. By recording and comparing the actual displacement responses with the calculated displacement response from the model, the accuracy of the developed model can be analysed. For example, Itto [82] applied a constant hanging weight on the free end of the PMA, and applied an instant compressed air flow input. The PMA fully contracted in around *10 to 20 seconds* and the contraction ratio response verified as congruent with the model's calculated response. In the experiments conducted by Wickramatunge and Leephakpreeda[81], the pressure was regulated at a stable level by a regulator and reservoir, and the load on the free end of the PMA was applied incrementally by the connected motor. A previously developed quasi-static model was found to be sensible for predicting the contraction response as *1.5 seconds*.

We noticed that, in most of the studies, researchers used large PMAs with diameters over *10 mm*, and these PMAs have higher stiffness when pressured. Given comparatively stiff PMAs that have accordingly large volumes and regulated input air flow rate, the recorded PMA responses in the experiments mentioned above (usually displacement responses) can be estimated by simple PM models. For instance, in the study in [84], Reynolds et al. developed a simplified empirical dynamic force model and successfully used it to predict and control the response of a stiff PMA.

A more complicated displacement response (with more and large oscillations in response) of the PMA was recorded in [23] where a PMA with a small diameter (*6 mm*) was pressured with constant

air mass, loaded with constant weight on its free end and applied with an initial displacement. Although the proposed dynamic force model in [23] is complex because of a nonlinear quasi-static force element, a viscous friction element and a non-constant Coulomb friction element, it is still insufficient to accurately estimate the actual response of the PMA in this case. This was despite the fact that “the natural frequency of estimated and actual displacement response was in good agreement” [23].

Therefore, this research aims at developing a comprehensive model for a type of small and soft PMA that is capable of estimating the response more accurately. To achieve this goal, each element in the dynamic force model of a PMA is discussed and existing dynamic force models for PMAs are reviewed.

### 3.1 Dynamic Model

#### 1. Static Model:

The static model is considered to be one part of the dynamic model. According to Chou and Hannaford in [59], based on the virtual work principle, the following equation/model is derived to characterise the quasi-static force of a PMA:

$$F_{static-chou} = -P(t) \frac{dV(t)}{dL(t)} \quad (3-1)$$

where  $P(t)$  stands for the pressure inside the PMA,  $L(t)$  is the actuator length,  $V(t)$  is the volume of the PMA, approximated as a cylinder.

$$V(t) = \frac{1}{4} \pi D(t)^2 L(t) \quad (3-2)$$

where  $D(t)$  denotes the diameter of the cylinder.

It is proposed in Chou and Hannaford [59] that  $L(t)$  and  $D(t)$  are related by proposed the following equations:

$$L(t) = b \cdot \cos \theta(t) \quad (3-3)$$

$$D(t) = \frac{b \cdot \sin \theta(t)}{n\pi} \quad (3-4)$$

in which  $n$  is the thread turns of the outer mesh;  $b$  is the thread total length of the outer mesh of a particular PMA; and  $\theta(t)$  denotes the angle between the PMA's axis and the outer mesh's thread direction, which is a variable determined by the length of the actuator  $L(t)$ .

Substituting Equations (3-2), (3-3) and (3-4) into (3-1), we obtain:

$$F_{static-chou} = P(t) \frac{3(L_0 - x(t))^2 - b^2}{4\pi n^2} = P(t) \frac{3x^2(t) - 6L_0x(t) + (3L_0^2 - b^2)}{4\pi n^2} \quad (3-5)$$

where  $L(t)$  and  $P(t)$  stand for the length and pressure of a PMA, and  $L_0$  is the nominal length of the PMA. Contraction length  $x(t) = L_0 - L(t)$ . Since an accurate value of the constants in Equation (3-5) are difficult to obtain [77], various modifications or empirical enhancement parameters have been made to this theoretical model [77–80]. In Equation (3-5),  $P(t)$  and  $x(t)$  are variables and the rest of the elements are constants. Therefore, the static force  $F_{static}$  can be presented as a 2<sup>nd</sup> order polynomial of the PMA's contraction length  $x(t)$  and the pressure  $P(t)$  as:

$$F_{static}(x, P) = K(x, P)x(t) + F_{ce}(P) = K_1P(t)x^2(t) + K_2P(t)x(t) + C_1P(t) \quad (3-6)$$

$K_1$ ,  $K_2$  and  $C_1$  are stiffness and contractile coefficients that are related to the PMA's property. Experiments are conducted later on to determine their values.  $K(x, P)$  is the stiffness element and  $F_{ce}(P)$  is the contractile element, expressed as:

$$K(x, P) = K_1P(t)x(t) + K_2P(t) \quad (3-7)$$

$$F_{ce}(P) = C_1P(t) \quad (3-8)$$

In order to improve the performance of this simplified model (Equation (3-6)), many research works ([77, 58]) have added a nonlinear correction force element,  $F_{adjust}$ , to account for the error caused by the thickness of the shell and the bladder, which is assumed to be independent of pressure [58]. This element can be in different forms, for example, in [80] it is a 4<sup>th</sup> order polynomial function. But in my research, I assume it as a 2<sup>nd</sup> order polynomial function of variable

$x(t)$  as in Equation (3-9), because with fewer coefficients it has a simpler form and is found still sufficient to provide accurate force estimation in later experiments.

$$F_{adjust}(x) = S_1x^2(t) + S_2x(t) + S_3 \quad (3-9)$$

Then the static force is written as:

$$\begin{aligned} F_{static}(x, P) &= K(x, P)x(t) + F_{ce}(P) + F_{adjust}(x) \\ &= (K_1x^2(t) + K_2x(t) + C_1)P(t) + S_1x^2(t) + S_2x(t) + S_3 \end{aligned} \quad (3-10)$$

As in Equation (3-9),  $S_1$ ,  $S_2$ ,  $S_3$ ,  $K_1$ ,  $K_2$  and  $C_1$  are regarded as unknown coefficients which need to be determined through experiments, so that the static force model  $F_{static}$  can be determined.

Since the coefficients of the static model ( $S_1$ ,  $S_2$ ,  $S_3$ ,  $K_1$ ,  $K_2$  and  $C_1$ ) can be obtained by experimental approaches, the modelling process, experiments and developed static models are stated in Section 3.2.1; in which the experimental method is similar to the one used in [80]. In this research, however, since multiple groups of experiments are performed to obtain the dynamic model, another way to acquire the static model is used in this research. This way uses the steady state displacement and pressure responses obtained from the experiments with instant compressed air flow input. The results will be presented in Section 3.2.1 below.

## 2. Dynamic Model

This research regards the static force model as a special case of the dynamic model, in the case that the friction force in the dynamic model is assumed to be zero. Previous studies [78] suggested that friction force in the PMA consists of a Coulomb friction element and a viscous damping element. Thus we propose our dynamic force model as:

$$F(x, P) = F_{static}(x) - F_{Damp} \pm F_{coulomb} \quad (3-11)$$

in which, Coulomb friction  $F_{coulomb}$  is velocity-irrelevant and viscous damping  $F_{Damp}$  is dependent on velocity [59]. The sign of  $\pm$  in front of  $F_{coulomb}$  denotes that the direction of coulomb friction depends on PMA's moving direction [59]. The modelling of  $F_{coulomb}$  and  $F_{Damp}$  are discussed respectively below.

(1)  $F_{coulomb}$ 

Coulomb friction is attributed to the dry friction between the rubber tube and the nylon braided sleeve, as well as the nylon threads' friction between each other [93]. It is believed that this friction causes hysteresis in the PMA response, which is known as the gap of displacement response between the excitation process and the relaxation process, in the experiment of applying the same constant load on the PMA [59].

The hysteresis response is related to multiple parameters (e.g. pressure, load, working duration, braided sleeve, diameter, material) and is difficult to be characterised with an accurate mathematical model [94]. In some quasi-static force models of PMAs that include Coulomb friction [58, 80, 24]), the expressions of Coulomb friction are all simplified to some extent. [59] suggested that a simple constant force of  $\pm 2.5N$  (positive for extending, negative for contracting) be added to the static force model to count for the effect of Coulomb friction when simplicity is acceptable. [58] also demonstrated the dominance of Coulomb friction in the total friction of the PMA. In other words, the viscous friction was regarded as much smaller than the Coulomb friction and thus neglected. Kang et al. [83] also regarded Coulomb friction as a constant. In [23], the case where the soft PMA is tested and oscillated displacement response was obtained, Coulomb friction is modelled as the product of a constant coefficient and the PMA's stiffness. The simulation result based on this model did not completely coincide with the experimental results. In summary, we found all these simplified models insufficient to characterise the responses of soft PMAs used in this research.

In some recent research papers discussing the model based controlling approaches for PMAs [90, 92], the excitation and relaxation processes are modelled as two separate high order polynomial functions of pressure and contraction length, or characterised by the Maxwell-Slip model. In other words, the Coulomb friction related hysteresis is explained by two functions of pressure and contraction. Researchers in [85] and [94] found that external loads on the PMAs can affect Coulomb friction. In [85], Balasubramanian et al. considered the effect of external load when explaining varied frequency and damping ratio of the displacement response in their experiment with constant weight and instant compressed air flow input. However, in both studies, the relationship between external loads and Coulomb friction are only quantitatively plotted, in other

words no model is presented. In this study, the relationship of Coulomb friction and external loads, and pressure and contraction length are analysed and a model with coefficients is presented to explain the experimental responses.

According to the definition of Coulomb friction [96]:

$$F_{Coulomb} = F_{Surface-Normal}(P(t), L(t)) \cdot \mu = P(t) \cdot \pi D(t) L(t) \cdot \mu \quad (3-12)$$

where the Coulomb friction force is defined as the product of normal force  $F_{surface-Normal}$  and the friction coefficient  $\mu$ . The surface normal force is calculated as the product of pressure and the contact area of the tube with the outer polymer mesh of the PMA. The contact area is approximated as the surface area of the tube (expressed as  $\pi D(t)L(t)$ ) of the PMA. According to the geometric relations derived in [59], when the geometry of a PMA is determined, then the thread length  $b$ , thread turns  $n$  of the mesh cover for the PMA are determined, and diameter  $D(t)$  is related to the length  $L(t)$  as:

$$D(t) = \frac{b \cdot \sin \theta(t)}{n\pi} = \frac{\sqrt{b^2 - L^2(t)}}{n\pi} \quad (3-13)$$

Substituting Equation (3-13) into Equation (3-12), we get

$$F_{Coulomb} = P(t) \mu \frac{\sqrt{b^2 - L^2(t)}}{n} L = \frac{P(t) \mu}{n} \sqrt{b^2 - (L_0 - x(t))^2} (L_0 - x(t)) \quad (3-14)$$

From Equation (3-14) we can approximate the Coulomb friction force as a second order polynomial function of the actuator length  $x(t)$ :

$$F_{Coulomb}(x, P) = P(t) (N_2 x^2(t) + N_1 x(t) + N_0) \quad (3-15)$$

Here,  $N_0$ ,  $N_1$  and  $N_2$  are the coefficients to be determined. It is also clearly stated in some literatures that, the hysteresis effect caused by the Coulomb friction in the PMA is related to the loads (in this case the hanging weight) applied on the PMA [85]. Considering the effect of external loads on the PMA, we apply a correction term  $\varphi(F_{ext})$  to Equation (3-15). The  $\varphi(F_{ext})$  is empirically found to be  $\varphi(F_{ext}) = -m$  in the constant weight hanging situation.

$$F_{Coulomb}(x, P) = (P(t) + \varphi(F_{ex}t)) \cdot (N_2x^2(t) + N_1x(t) + N_0) \quad (3-16)$$

## (2) $F_{damp}$

The viscous damping was stated to be not as significant as the Coulomb friction [59]. In most cases it is simplified as the product of a constant damping coefficient and the contraction velocity. However, according to the statement made by Colbrunn et al. in [23], that “the damping may not be a constant”, a more sophisticated model for the viscous damping element is developed.

The viscous damping element characterises the viscosity of the compressed air, and the friction between the air and the tube’s inner surface. The friction between the rubber material and the polymer mesh is believed to be dry friction and is characterised by Coulomb friction.

The first part of viscous friction results from the viscosity of the compressed air itself, which is the friction between gas particles in the air. According to [97] it is expressed as follows:

$$F_{viscosity} = Area \times \mu_{Air} \frac{\partial v}{\partial y} \quad (3-17)$$

Here  $\mu_{Air}$  denotes the viscosity of air gas, and  $\frac{\partial v}{\partial y}$  denotes the shear velocity. assuming it is inside a simple round tube; the shear velocity is linearly related to the distance of the air particle to the inner wall of the tube [97], thus the shear velocity is linearly related to the average velocity  $v$ .

$\mu_{Air}$  is a constant and calculated [97] as:

$$\mu_{Air} = 1.456 \times 10^{-6} \frac{T^{1.5}}{T + 110.4} \quad (3-18)$$

In this case  $\mu_{Air} = 18.4347 \times 10^{-6} \text{ kg/sm}$  ( $T$  is assumed as the normal atmospheric temperature 273K).

To conclude, the viscous friction between the air particles is linearly related to the average flow velocity  $v(t)$ , and is modelled as:

$$F_{viscosity} = D_2 P(t) v(t) \quad (3-19)$$

The second part of viscous damping is from the skin friction between the compressed air and the inner wall of the PMA's rubber tube. This friction force can be called drag force and is expressed as [98]:

$$F_{Drag} = C_d \frac{\rho v^2}{2} \times Area \quad (3-20)$$

From (3-20), the drag force is believed to be dependent on the square of air velocity, thus we assume the viscous damper element to be:

$$F_{Damp} = F_{Drag} + F_{viscosity} = D_1 P \dot{x}^2 + D_2 P \dot{x} = D(\dot{x}, P) \dot{x} \quad (3-21)$$

$D_1$  and  $D_2$  are the coefficients to be determined by dynamic experimental results. In Equation (3-21), we made the assumption that contraction velocity of the PMA  $\dot{x}(t)$  equals the air transmission velocity  $v(t)$ , similar to what other researchers did in their studies [24, 58, 80].

In summary, the dynamic contraction force is expressed as:

$$F(x, P) = (K_1 x^2(t) + K_2 x(t) + C_1) P(t) + S_1 x^2(t) + S_2 x(t) + S_3 - P(t)(D_1 \dot{x}^2(t) + D_2 \dot{x}) + (P(t) + \varphi(F_{at})) \cdot (-\text{sign}(\dot{x})) (N_2 x^2(t) + N_1 x(t) + N_0) \quad (3-22)$$

In the rest of this chapter the coefficients in the above model will be determined using the experimental data.

## 3.2 The Development of the Dynamic Model's Coefficients

Multiple experiments are conducted to obtain the coefficients ( $K_1, K_2, C_1, S_1, S_2, S_3, N_1, N_2, D_1, D_2$ ) of the dynamic model in Equation (3-22). The Shadow Robot Company© manufactured PMA  $\Phi 6-300mm$  is used to perform the experiments. In this section, only parts of the experimental results are presented to demonstrate our methodology, the rest of the experimental results are presented in Appendix B .

A series of constant hanging weight and instant compressed air flow input experiments were carried out [58, 76–78]. In each test, a constant load is hung on the free end of the PMA and an instant

compressed air flow is applied to the PMA. This is different from the method of using motors to apply the load (force) change on the PMA and maintaining constant pressure. In this way the impact of the insufficiently modelled elements is more evident and the transient response is measured. The experimental setup is shown in the following figure.

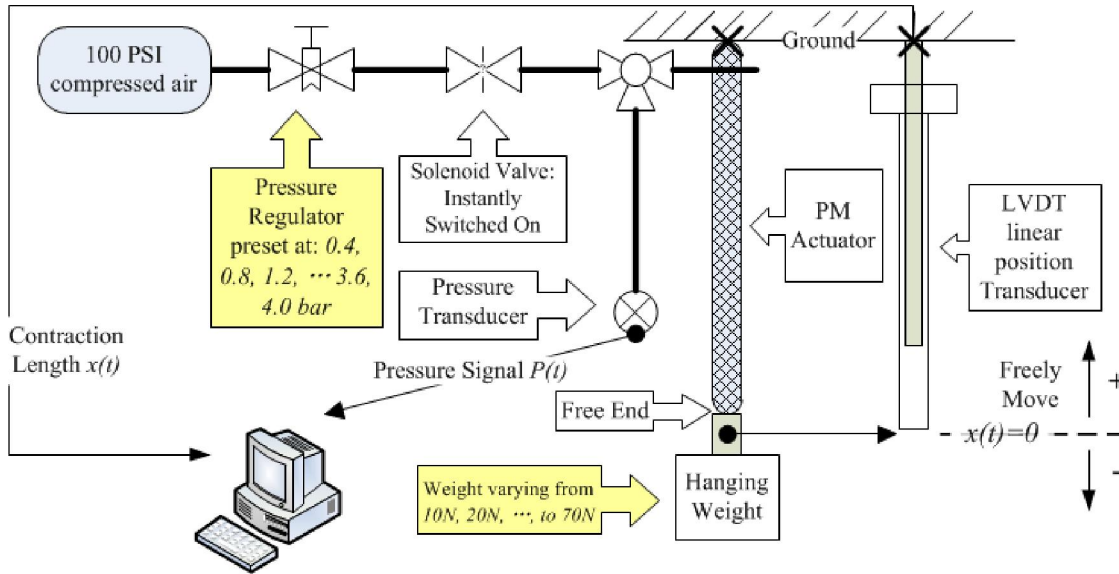


Figure 3-1: Schematic experimental setup

Multiple tests are conducted on this test rig, in which a series of different pre-set pressures on the pressure regulator and different external hanging loads are applied. In each test the solenoid valve is instantly switched on to inflate the empty PMA to the pre-set pressure. The initial eight seconds response of the PMA's free end position and the pressure inside the airway are recorded in each test. Various pressure and weight values are used. The pre-set pressure applied on the pressure regulator are changed from around the atmospheric pressure to 0.4, 0.8, 1.2, 1.6, 2.0, 2.4, 2.8, 3.2 3.6 and 4.0 bar respectively; and loads ranged from 12.74N to 72.74N with an increment of 10N, with 2.74N of the weight holder included. The purpose of using equal intervals from 0.4 bar to 4.0 bar is to measure the response in both lower pressure and high pressure. Therefore, 70 tests in total have been conducted. A sample of the displacement and pressure response in time domain in the case of pre-set pressure at around 4 bar and hanging load of 22.74 N is plotted in Figure 3-2.

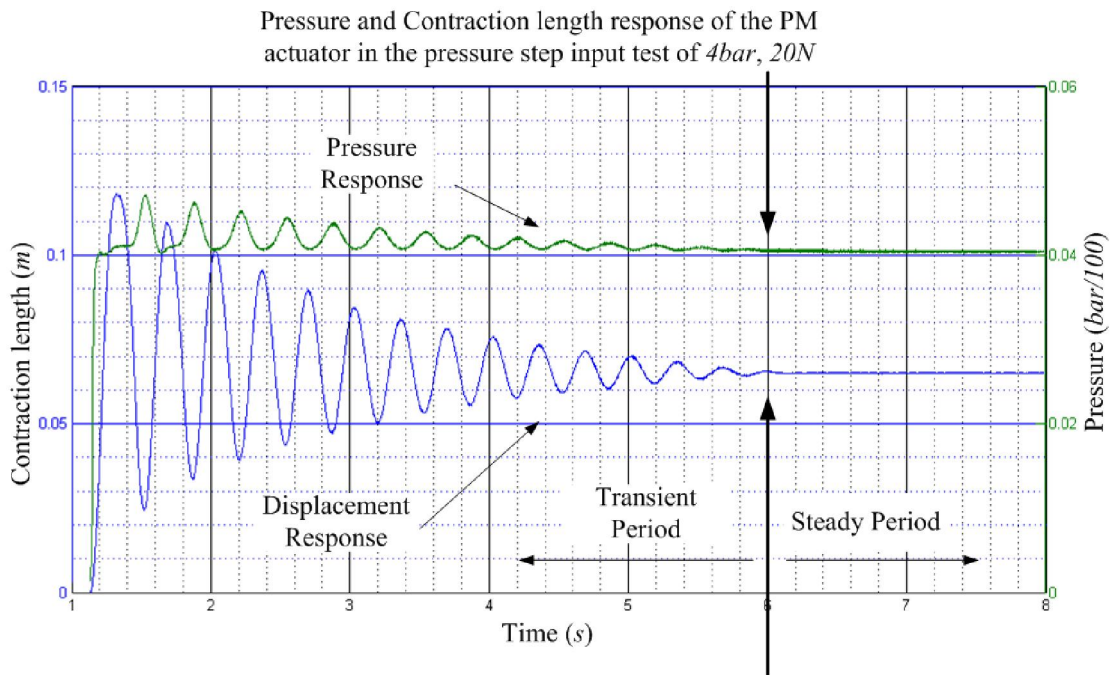


Figure 3-2: Sample response of the test with pre-set pressure of 4 bar, hanging weight 22.74 N)

It is observed that in this sample the settling time is rather long (close to 6 seconds). It is mainly attributed to the lack of damping in the system. However in terms of studying the model of PMA, such response is acceptable. Several approaches can be adopted to reduce the settling time in practical application of the PMA. One straightforward method is to add an orifice between the solenoid valve and the PMA's inlet. Similar to the effect of adding a resistance in an electrical system or a damper in a mechanical system, it can effectively reduce the flow rate and suppress the oscillation in response. On the basis of this idea, feedback control of the flow rate can be further implemented to improve the response.

### 3.2.1 The Static Model

Many other researchers [58, 96, 76, 77, 24] have introduced experimental approaches to obtain the static force model of PMAs. We adopted the approach similar to the one used in [80] to test the PMA and obtain the static models. The details of this part of the work are presented in Appendix A .

However, we also found a way to obtain the coefficients ( $K_1, K_2, C_1, S_1, S_2, S_3$ ) of the static model (Equation (3-6)) by just using the data of experiments with constant load and instant compressed air flow input introduced at the beginning of Section 3.2. By applying the static model to the steady

state response of multiples tests, such as the time period of 6 seconds to 8 seconds in Figure 3-3, where no damping or coulomb friction force exists, the coefficients ( $K_1, K_2, C_1, S_1, S_2, S_3$ ) can then be determined. Due to the equilibrium state of the PMA in each test's steady state, the static force model, Equation (3-6) applies and the static equilibrium is represented by the following equation of motion as:

$$F_{static}(x, P) - mg = K(x, P)x(t) + F_{ce}(P) + F_{adjust}(x) - mg = 0 \tag{3-23}$$

One thing to note is that, this equation of motion is only valid when the hung weight is within the PMA's force capability limitation under the given pressure.

Substituting Equations (3-7), (3-8) and (3-9) in to Equation (3-23), we get

$$\left(K_1x_{stable}^2 + K_2x_{stable} + C_1\right)P_{stable} + S_1x_{stable}^2 + S_2x_{stable} + S_3 - mg = 0 \tag{3-24}$$

The average pressure  $P_{stable}$  and average contraction length  $x_{stable}$  of each test's steady state period are presented in Table 3-1 and Table 3-2, respectively.

Table 3-1: Average value of pressure for the steady-state period of each instant compressed air flow input test

$P_{stable}(\text{Bar})$	12.74N	22.74N	32.74N	42.74N	52.74N	62.74N	72.74N
0.4Bar	0.410	0.410	0.435	0.430	0.430	0.418	0.428
0.8Bar	0.823	0.825	0.810	0.835	0.828	0.828	0.840
1.2Bar	1.223	1.215	1.235	1.240	1.230	1.225	1.233
1.6Bar	1.630	1.632	1.608	1.620	/	1.595	1.593
2.0Bar	/	2.040	2.020	2.010	2.032	2.032	2.037
2.4Bar	2.417	2.425	2.422	2.380	2.435	2.425	2.425
2.8Bar	2.817	2.825	2.849	2.817	2.815	2.703	2.705
3.2Bar	3.192	/	3.232	/	3.210	3.227	3.210
3.6Bar	3.624	3.634	3.637	3.639	3.587	3.624	3.622
4.0Bar	4.054	4.051	4.069	3.994	4.009	3.974	4.024

Table 3-2: Average of contraction length for the steady-state period of each instant compressed air flow input test

$x_{stable}(mm)$	12.74 N	22.74 N	32.74 N	42.74 N	52.74 N	62.74 N	72.74 N
0.4 Bar	1.083	1.067	0.476	0.275	-0.026	-0.063	-0.109
0.8 Bar	4.649	2.323	1.605	1.175	0.629	0.528	0.340
1.2 Bar	12.498	4.901	3.028	2.096	1.605	0.994	0.559
1.6 Bar	30.010	12.317	5.710	3.897	/	1.731	1.313
2 Bar	/	24.450	11.281	5.863	4.033	2.956	2.317
2.4 Bar	53.885	36.628	20.236	11.513	6.414	4.916	2.342
2.8 Bar	61.337	46.000	31.253	18.479	10.542	6.703	4.685
3.2 Bar	66.835	/	39.772	/	16.933	11.102	6.902
3.6 Bar	72.128	59.673	47.823	35.445	24.676	16.467	10.115
4 Bar	75.098	65.224	53.921	42.427	32.161	22.762	15.860

Multiple groups of  $x_{stable}$  and  $P_{stable}$  data in Table 3-1 and Table 3-2 are substituted into equation (3-23) to determine the coefficients. In order to prevent using data that is invalid, we tend to choose higher pressure and lower pressure cases of data. Two groups of initial data were selected to obtain two groups of results. By using the data from the groups of (2.0bar, 20N), (2.8bar, 10N), (3.6bar, 20N), (3.6bar, 30N), (4.0bar, 40N) and (4.0bar, 50N) (where contraction length is in units of meter, and pressure is in the units of bar), the following coefficients are obtained:

$$K_1 = -476.95, K_2 = -188.39, C_1 = 23.90, S_1 = 2562.4, S_2 = -245.48, S_3 = -11.56$$

Thus the PMA static force model is:

$$F_{static}(x, P) = (-476.95x^2(t) - 188.39x(t) + 23.9)P(t) + 2562.4x^2(t) - 245.48x(t) - 11.56 \quad (3-25)$$

Another group of results were calculated from tests (2.0bar, 20N), (2.8bar, 40N), (3.6bar, 20N), (3.6bar, 50N), (4.0bar, 20N) and (4.0bar, 30N):

$$K_1 = 451.7, K_2 = 272.9, C_1 = 25.9, S_1 = 1503.8, S_2 = -157.1, S_3 = -14.2$$

Similar results are obtained by using groups of  $x_{stable}$  and  $P_{stable}$  data from other valid experiments.

To verify the obtained static force model, we substitute the contraction length and pressure values in Table 3-1 and Table 3-2 and the above two groups of coefficients results of  $(K_1, K_2, C_1, S_1, S_2, S_3)$  into Equation (3-10) to calculate the static actuation force on the free end of the PMA. The results are shown in Table 3-3b (based on the first group of data) and that in Table 3-3a (based on the second group of data). The calculated static actuation forces during the steady state period should be close to the hung weight on the free end of the PMA.

The estimation results in Table 3-3a are based on assuming the estimated weights in the cases of  $(2.0bar, 20N)$ ,  $(2.8bar, 40N)$ ,  $(3.6bar, 20N)$ ,  $(3.6bar, 50N)$ ,  $(4.0bar, 20N)$  and  $(4.0bar, 30N)$  equal the actual weights. These groups of force estimation results are in bold and underlined. The rest of the estimations in this table are based on the trained static force model from these six groups. The same method and presentation apply in Table 3-3b as well.

Table 3-3a: Estimated actuation force of the PMA in the stable period calculated from group of  $(2.0bar, 20N)$ ,  $(2.8bar, 40N)$ ,  $(3.6bar, 20N)$ ,  $(3.6bar, 50N)$ ,  $(4.0bar, 20N)$  and  $(4.0bar, 30N)$

Estimation (N)&Error	12.74 N	22.74 N	32.74 N	42.74 N	52.74 N	62.74 N	72.74 N
0.4 Bar	-3.80	-3.80	-3.00	-3.07	-2.99	-3.30	-3.03
0.8 Bar	5.45	6.37	6.26	7.05	7.07	7.11	7.50
1.2 Bar	11.74(-7.9%)	15.01	16.40	16.97	16.96	17.13	17.53
1.6 Bar	12.07(-5.3%)	21.10(7.2%)	24.21	25.56	26.72	26.19	26.37
2 Bar	12.96(1.8%)	<b>22.74(0%)</b>	30.54	33.91	35.72	36.47	37.04
2.4 Bar	12.06(-5.3%)	22.22(-2.3%)	33.17(1.3%)	38.62	43.82	44.76	46.82
2.8 Bar	12.56(-1.4%)	22.29(-2.0%)	33.25(1.6%)	<b>42.74(0%)</b>	49.39	50.06	51.87
3.2 Bar	13.07(2.6%)	/	33.02(0.9%)	/	52.43(-0.6%)	58.37	62.09
3.6 Bar	13.51(6.0%)	<b>22.74(0%)</b>	32.38(-1.1%)	43.41(1.6%)	<b>52.74(0.0%)</b>	61.81	68.51
4 Bar	14.91(17%)	<b>22.74(0%)</b>	<b>32.74(0%)</b>	42.48(-0.6%)	53.01(0.5%)	62.36(-0.6%)	71.13

Table 3-3b: Estimated actuation force of the PMA in the stable period calculated from group of (2.0bar, 20N), (2.8bar, 10N), (3.6bar, 20N), (3.6bar, 30N), (4.0bar, 40N) and (4.0bar, 50N)

Estimation (N)&Error	12.74 N	22.74 N	32.74 N	42.74 N	52.74 N	62.74 N	72.74 N
0.4 Bar	-2.09()	-2.09	-1.31	-1.36	-1.26	-1.55	-1.30
0.8 Bar	6.29	7.25	7.18	7.93	7.97	8.01	8.38
1.2 Bar	12.02(-5.6%)	15.21	16.53	17.08	17.08	17.25	17.63
1.6 Bar	12.42(-2.5%)	20.91(-8.0%)	23.79	25.04	26.11	25.62	25.79
2 Bar	13.46(5.6%)	<b>22.74(0.0%)</b>	29.86	32.87	34.50	35.17	35.68
2.4 Bar	12.54(-1.6%)	22.55(-0.8%)	32.70(-0.1%)	37.52	42.17	42.97	44.75
2.8 Bar	<b>12.74(0.0%)</b>	22.75(0.0%)	33.26(-1.6%)	41.84(-2.1%)	47.66	48.03	49.58
3.2 Bar	12.77(0.3%)	/	33.31(1.8%)	/	51.04(-3.2%)	56.21	59.33
3.6 Bar	12.44(-2.4%)	<b>22.74(0.0%)</b>	<b>32.74(0.0%)</b>	43.45(1.7%)	51.95(-1.5%)	60.00	65.70
4 Bar	13.08(2.7%)	22.15(-2.6%)	32.92(0.5%)	<b>42.74(0.0%)</b>	<b>52.74(0.0%)</b>	61.14(-2.6%)	68.86

The estimated force or weight results are generally in accordance with the actual hanging weight, indicating a valid static force model. It is noted that the model is only valid when the PMA is within its force capability limitation. The shaded background area, i.e. the upper half above the thick line in Table 3-3a and Table 3-3b, indicate the PMA's force capability limitations at each pressure level. For instance, in Table 3-3a, at the pre-set pressure level at around 2.8 Bar, when the actual hung weight is applied as 12.74 N, 22.74 N, 32.74 N and 42.74 N, the estimated static forces are all close to the actual weight (12.56 (-1.4%), 22.29 (-2.0%), 33.25 (1.6%) and 42.74 (0%)). However, as the hanging weight increases to 52.74 N, 62.74 N and 72.74 N, the estimated actuation force of the PMA remains at a certain value lower than the actual weights (around 49 N to 52 N), thus failing to provide sufficient active force to lift the weights. In these cases, the PMA couldn't perform further contraction, and its length barely changes even when weights of 52.74 N, 62.74 N and 72.74 N are applied. The estimation error of each estimated force within the force range is displayed in the brackets.

In Table 3-3a and Table 3-3b, most of the other weight estimation results are satisfactory, with

estimation error (shown in the bracket next to each result) within 7%. Four cases of large misalignment is found in (1.6 bar, 22.74 N, -8.0%) in Table 3-3b and (1.2 bar, 22.74 N, -7.9%), (1.6 bar, 22.74 N, 7.2%), (4.0 bar, 12.74 N, 17%) in Table 3-3a. This might be due to the fact that when estimating smaller weights such as 10 N, 20N, even small amount of error in the estimated force could lead to an evident relative error (for instance, an error of 1 N in the case of 12.74 N would lead to an error close to 10%).

Comparing the estimation results in Table 3-3a and Table 3-3b, the estimations of smaller loads in the second group are not as satisfactory as the first group, in one case the estimation error even reaches 17% (Table 3-3a, pressure 4.0 bar, load 12.74 N). Thus the static force model calculated from the first group, shown in Equation (3-25), is used in the following study.

The approach of obtaining coefficients in the static model is improved by utilising all the redundant data in the rest of the valid tests. An optimisation is performed, the six coefficients ( $K_1$ ,  $K_2$ ,  $C_1$ ,  $S_1$ ,  $S_2$ ,  $S_3$ ) are regarded as variables of the objective function, which calculates the sum of the squared error between the estimated load and the actual weight load in every valid test. The following optimal coefficients are obtained by minimising the cost function.

$$K_1 = -834.28, K_2 = -175.81, C_1 = 24.15, S_1 = 5296.84, S_2 = 439.28, S_3 = -8.939$$

The corresponding estimation results using this set of coefficient values are shown in Table 3-3c. The estimation results turn out better than the previously two estimation results that are based only on six groups of test data. The maximum deviation decreases to 4.4% (in the case of 1.6 bar, 12.74N) and the mean of the deviation decreases to 1.62%. Unfortunately, by the time the dynamic model was developed, the optimal coefficients were not acquired.

Table 3-3c: Estimated actuation force of the PMA in the stable period calculated from optimised coefficients

Estimation (N)&Error	12.74 N	22.74 N	32.74 N	42.74 N	52.74 N	62.74 N	72.74 N
0.4 Bar	-3.80	-3.80	-3.00	-3.07	-2.99	-3.30	-3.03
0.8 Bar	5.45	6.37	6.26	7.05	7.07	7.11	7.50
1.2 Bar	13.08(2.7%)	15.01	16.40	16.97	16.96	17.13	17.53
1.6 Bar	12.19(-4.4%)	21.14(-2.7%)	24.20	25.56	26.72	26.19	26.37
2 Bar	13.06 (2.5%)	22.96(1.0%)	30.54	33.91	35.72	36.47	37.04
2.4 Bar	12.39(-2.7%)	22.31(-1.9%)	33.39(2.0%)	38.62	43.82	44.76	46.82
2.8 Bar	12.85 (0.9%)	22.45(-1.3%)	33.34(1.8%)	42.83(0.2%)	49.39	50.06	51.87
3.2 Bar	13.05(2.4%)	/	33.16(1.3%)	/	52.33(-0.8%)	58.37	62.09
3.6 Bar	12.77 (0.2%)	22.55(-0.8%)	32.48(-0.8%)	43.54(1.9%)	52.69(-0.1%)	61.81	68.51
4 Bar	13.25 (4.0%)	21.95(-3.5%)	32.6(-0.4%)	42.63(-0.3%)	53.11(0.7%)	62.17(-0.9%)	71.13

### 3.2.2 The Dynamic Model

After the coefficients in the static force model ( $K_1$ ,  $K_2$ ,  $C_1$ ,  $S_1$ ,  $S_2$  and  $S_3$ ) are determined and verified, the other coefficients ( $D_1$ ,  $D_2$ ,  $N_1$ ,  $N_2$ ) in the dynamic force model (Equation (3-22)) are to be determined from the experimental data as well.

We used the least squares fitting approach to find the best group of coefficients ( $D_1$ ,  $D_2$ ,  $N_1$ ,  $N_2$ ). The objective function  $\Psi(D_1, D_2, N_1, N_2)$  is Equation (3-28), in which simulation response of contraction length  $x_{simu}(t)$  comes from the following equation of motion

$$\begin{aligned}
 m\ddot{x}(t) &= F(x, P) - mg \\
 &= F_{static} - F_{Damp} \pm F_{coulomb} - mg
 \end{aligned}
 \tag{3-26}$$

In the above equation,  $\ddot{x}(t)$  denotes acceleration.  $F_{static}$  is already developed in Equation (3-25).

Similar to other dynamic models [58, 80], Coulomb friction is dependent on the velocity of the PMA,  $\dot{x}(t)$ . Introducing the pattern discovered in this experiment  $\varphi(F_{ext}) = -m$ , the equation of motion (3-26) is rewritten as:

$$m\ddot{x}(t) = F_{static} - P(t)(D_1\dot{x}^2(t) + D_2\dot{x}) + (P(t) + \varphi(F_{ext})) \cdot (-\text{sign}(\dot{x})) \cdot (N_2x^2(t) + N_1x(t) + N_0) \quad (3-27)$$

The variables ( $D_1, D_2, N_1, N_2$ ) are estimated and adjusted until the minimum sum of the squared residual of the simulation and real contraction lengths (from the experimental results) is found, as denoted in Equation (3-27)

$$\Psi(D_1, D_2, N_1, N_2) = \min \left\| \sum_t (x_{simu}(t) - x(t))^2 \right\| \quad (3-28)$$

In Matlab™, the function lsqcurvfit and trust-region-reflective algorithm are used to perform this approach.

By using the experimental data from the valid experiments (see Table 3-3a and Table 3-3b for the cases that have sufficient force capability), we can obtain the optimal coefficients. In general, similar values of the coefficients are obtained from all the valid test data (please refer to Appendix B for all the solutions and their resultant simulation responses in comparison with the experimental data). Here, we presented the results obtained by using the data from the test with pre-set regulator pressure of 3.6 bar and hanging weight of 20 N (the transient response region shown in Figure 3-3). The obtained Coulomb friction and damping force are:

$$F_{Coulomb}(x, P) = \left( \frac{P(t)}{10^5} - m \right) \cdot (-\text{sign}(\dot{x})) \cdot (228.9342x^2(t) + -90.429x(t) + 6.87) \quad (3-29)$$

$$F_{Damp}(\dot{x}, P) = P(t) \left( -\dot{x}^2(t) + 0.802\dot{x}(t) \right) \quad (3-30)$$

Substituting into the empirical dynamic force model for the PMA we are testing gives:

$$m\ddot{x}(t) = F_{static} + P(t) \left( \dot{x}^2(t) - 0.802\dot{x}(t) \right) + \left( \frac{P(t)}{10^5} - m \right) \cdot (-\text{sign}(\dot{x})) \cdot (228.9342x^2(t) + -90.429x(t) + 6.87) \quad (3-31)$$

For the results of the coefficients and responses obtained from other experiments with different pressure inputs and different weights, please refer to Appendix B .

Table 3-4 shows the coefficients obtained in each test; since similar results are obtained, in this thesis, we used the Coulomb friction and damping coefficient models in Equations (3-29) and (3-30) to obtain the simulation results in Table 3-4. The response plots of the rest of the valid experiments (see Table 3-3b for valid experiments) are presented in Appendix B .

Table 3-4: Optimal coefficients of ( $N_2, N_1, N_0, D_1, D_2$ ) in dynamic force model for PMA in Equation (3-22)

$N_2, N_1, N_0,$ $D_1, D_2$	12.74 N	22.74 N	32.74 N	42.74 N	52.74 N
1.6 Bar	224.93, -91.31, 6.86 -1.01,0.80	/	/	/	/
2 Bar	/	227.91, -90.42, 6.87, -1.01,0.80	/	/	/
2.4 Bar	228.50, -90.73, 6.87, -1.01,0.80	228.50, -90.51, 6.87, -1.01,0.80	/	/	/
2.8 Bar	228.93, -90.43, 6.87, -1.01,0.80	228.94, -90.43, 6.87, -1.01,0.80	228.95, -90.43, 6.87, -1.01,0.80	/	/
3.2 Bar	228.93, -90.43, 6.87, -1.01,0.80	/	228.93, -90.43, 6.87, -1.01,0.80	/	/
3.6 Bar	228.93, -90.42, 6.87, -1.01,0.80	228.93, -90.43, 6.87, -1.01,0.80	228.93, -90.43, 6.87, -1.01,0.80	228.94, -90.43, 6.87, -1.01,0.80	227.45, -90.43, 6.88, -1.02, 0.80
4 Bar	228.92, -90.42, 6.87, -1.01,0.80	228.92, -90.43, 6.87, -1.01,0.80	228.93, -90.43, 6.87, -1.01,0.80	228.94, -90.42, 6.88, -1.01,0.80_	228.93, -90.45, 6.90, -1.01, 0.80

The comparison of the simulation response is shown in Figure 3-3. Valid enhancement of our

model in response prediction is observed in this case.

Besides the simulation results from the developed model in this research, we also applied a constant Coulomb friction force model of  $2.5\text{ N}$  suggested by [23] to replace the Coulomb friction force component in Equation (3-16) to obtain the simulation response. The resultant response in comparison with the experimental data is shown in Figure 3-3.

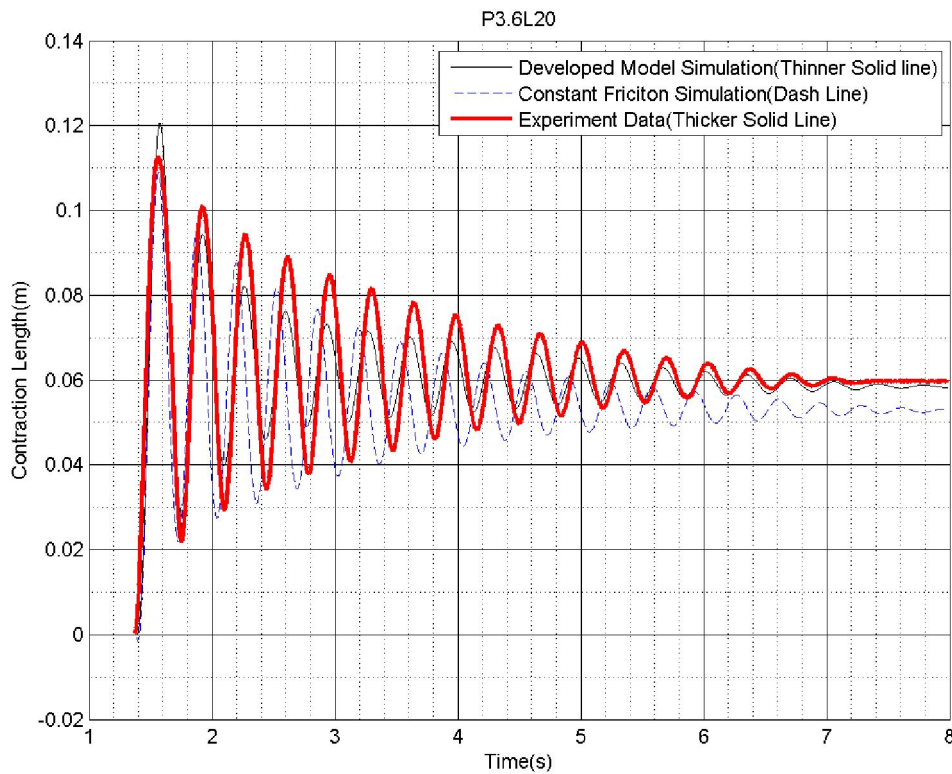


Figure 3-3: Comparison of results: experimental response (contraction length) with a pre-set pressure of  $3.6\text{ bar}$  and load of  $20\text{ N}$ ; the simulation results from the case with constant Coulomb friction force of  $2.5\text{ N}$  suggested by [23], and the simulation data obtained by the model (Equation (3-31))

Figure 3-4 shows the results obtained from a different experiment with a pre-set pressure of  $3.6\text{ bar}$  and load of  $10\text{ N}$ , the simulation results obtained from the developed model, and the simulation results using the constant Coulomb friction force of  $2.5\text{ N}$  suggested by [23]. It can be seen from Figure 3-4 that the results based on our model is much closer to the experimental data, compared to the simulation results based on the constant Coulomb friction force. This enhancement is attributed to the external load element  $\varphi(F_{ext})$  in Coulomb friction.

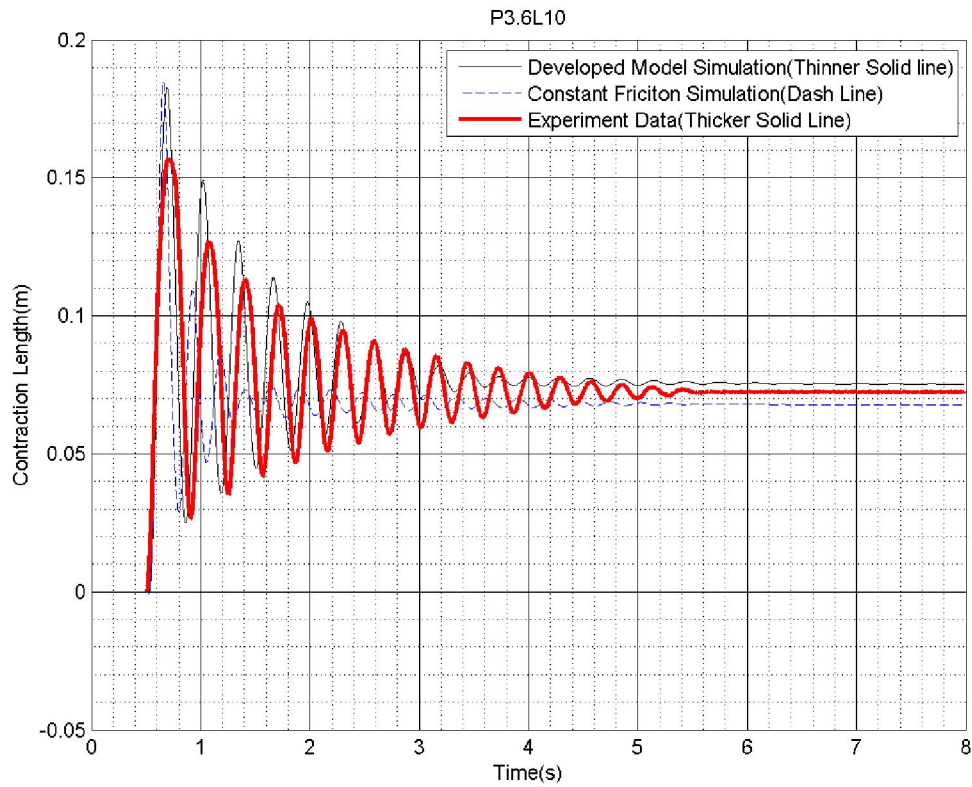


Figure 3-4: Comparison of results: experimental response (contraction length) with a pre-set pressure of  $3.6\text{bar}$  and load of  $10\text{N}$ ; the simulation results from the case with constant Coulomb friction force of  $2.5\text{ N}$  suggested by [23], and the simulation data obtained by the model (Equation (3-31))

Comparison of our developed dynamic model with other dynamic models is somewhat difficult. Different factors relating to the PMA's structure, size and material can lead to various performances, as well as the way the PMA works. However, by comparing how different Coulomb friction models affect the PMA's displacement response in the experiment of this thesis, it is clear that our proposed Coulomb friction model has better performance, especially with the varied external loads. To the best of my knowledge, no other models take the external loads as variables into account.

## Chapter 4 *3UPU wrist* Parallel Mechanism Design

This chapter discusses the issues related to the development of a *3UPU wrist* parallel shoulder mechanism for the shoulder assistive robot. Section 4.1 elaborates on the structure of this mechanism and outlines the conditions required for the *3UPU wrist* mechanism to perform a 3D rotation movement around a fixed rotation centre. Section 4.1 also discusses the kinematics of the *3UPU wrist* mechanism, and reviews the existing analytical solutions of both inverse kinematics and forward kinematics for this mechanism. Further, an alternative forward kinematics approach is proposed. This approach calculates the platform orientation based on six or three angles measured from the universal joints that connect the limbs to the base. Other related works on the *3UPU wrist* mechanism, which are not the core research of this thesis, are presented in Appendix C and Appendix D. Appendix C elaborates a way of obtaining an optimal geometric design that maximises the mechanism's workspace. Appendix D provides a way of calculating the reaction forces transmitted to the shoulder joint when the *3UPU wrist* mechanism is implemented to assist the shoulder joint.

### 4.1 Mechanism Structure

The *3UPU wrist* mechanism, namely a rotational three limb universal-prismatic-universal joint mechanism was first introduced by Karouia and Herve [53]. Like other “*3UPU*” mechanisms, it consists of an immobile base, a moving platform and three linear moving components referred to as “limbs”. The number “3” indicates three limbs in this mechanism that are connected to the base and the platform on their two ends. The term “*UPU*” denotes the type of articulation of each limb to the base, within itself and to the platform respectively. Specifically, each limb is connected to the base as well as to the platform by a universal (*U*) joint; the limb itself consists of a prismatic (*P*) joint (Figure 4-1(a)). It has been demonstrated in [100] that a “*3UPU*” mechanism has three degrees of freedom, while different geometric layouts of the universal joints can achieve different combinations of translation or rotation. For a “*3UPU*” mechanism to become a *3UPU wrist* mechanism that performs a 3D rotation around a fixed rotation centre, Gregorio [101] has listed two conditions, as follows:

1. Consider the universal joints on the platform and the base as six pairs of orthogonal revolute

joints, and each pair of the six revolute pairs must have one revolute axis intersecting with the axes from the other revolute pairs at a common fixed point in space. This condition is illustrated in Figure 4-1(a), where the six revolute axes of revolute joint pairs centred at  $A_1, A_2, A_3, B_1, B_2$  and  $B_3$  ( $\overline{Y_{Ai}}$  and  $\overline{Y_{Bi}}$ ,  $i = 1, 2, 3$ ) all intersect at point  $O$  in space.

2. While one revolute axis of each universal joint ( $\overline{Y_{Ai}}$ ,  $i = 1, 2, 3$ ) intersects with others at a common point, the other revolute axis must be in parallel with the one on the other end of the connected limb. As illustrated in Figure 4-1(a), axis  $\overline{X_{Ai}}$  is in parallel with  $\overline{X_{Bi}}$ .

Only under these conditions, will the platform perform a rotation only movement around the axes intersecting point  $O$  in three directions, with the three limbs ( $A_i B_i$ ,  $i = 1, 2, 3$ ) contracting or stretching.

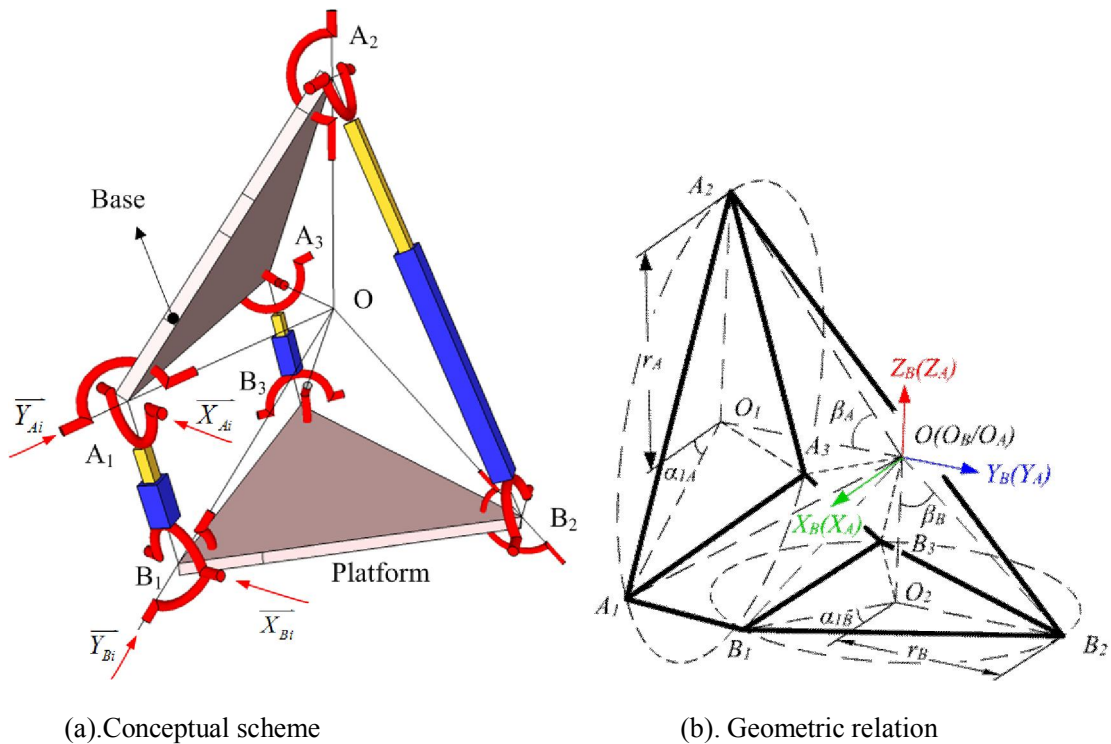


Figure 4-1: Geometry of the 3UPU wrist mechanism

The defined points, distances, angles and coordinates of the 3UPU wrist mechanism are illustrated in Figure 4-1(b). The universal joints on the base plane are defined by their centre point as  $A_1, A_2, A_3$  and on the platform plane as  $B_1, B_2, B_3$  respectively. Therefore the base plane is represented by

triangle  $A_1A_2A_3$ . and the platform is represented by  $B_1B_2B_3$ . The centres of them are Point  $O_1$  and Point  $O_2$ , respectively. Point  $O$  is the platform rotation centre, which is also the intersection point of all six revolute joint axes. Line  $OO_1$  is perpendicular to plane  $A_1A_2A_3$  and  $OO_2$  is perpendicular to plane  $B_1B_2B_3$ . For simplicity in design, we assume that the distances from points  $A_1, A_2$  and  $A_3$  to point  $O_1$  are the same. So are the distances from points  $B_1, B_2$  and  $B_3$  to  $O_2$ . In this way, point  $A_1, A_2$  and  $A_3$  and points  $B_1, B_2$  and  $B_3$  are actually on the rings of two circles, the circular centre of which are point  $O_1$  and point  $O_2$ , respectively. We define the radius of circle  $A_1A_2A_3$  as  $r_A$  and the radius of circle  $B_1B_2B_3$  as  $r_B$ , then  $|O_1A_i| = r_A, |O_2B_i| = r_B, (i = 1, 2, 3)$ . The distance from the base plane to point  $O$  is defined as  $|O_1O| = h_A$ , and from the platform plane to  $O$  is  $|O_2O| = h_B$ . Angle  $\alpha_{iA}$  denotes the projection of angle formed by  $\overline{O_1A_i}$  and axis  $X_A$  on plane  $A_1A_2A_3$ . The angle between vectors  $\overline{O_1O}$  and  $\overline{OA_i}$  ( $\angle O_1OA_i$ ) is defined as  $\beta_A$ . A fixed coordinate frame  $\{O_A: X_A Y_A Z_A\}$  is attached to the base, with rotation centre  $O$  ( $O_A$ ) as its origin. A mobile coordinate frame  $\{O_B: X_B Y_B Z_B\}$  attached to the platform is defined as originated at point  $O$  ( $O_B$ ) as well. The origin points of both coordinate frames ( $O_A$  and  $O_B$ ) coincide with point  $O$ . In this thesis, the terms  $O_A$  and  $O_B$  will only be used to substitute point  $O$  in circumstances where the used coordinate frame needs to be emphasised. By default, in most cases we presume the discussion is made in the base coordinate frame  $\{O_A\}$ .

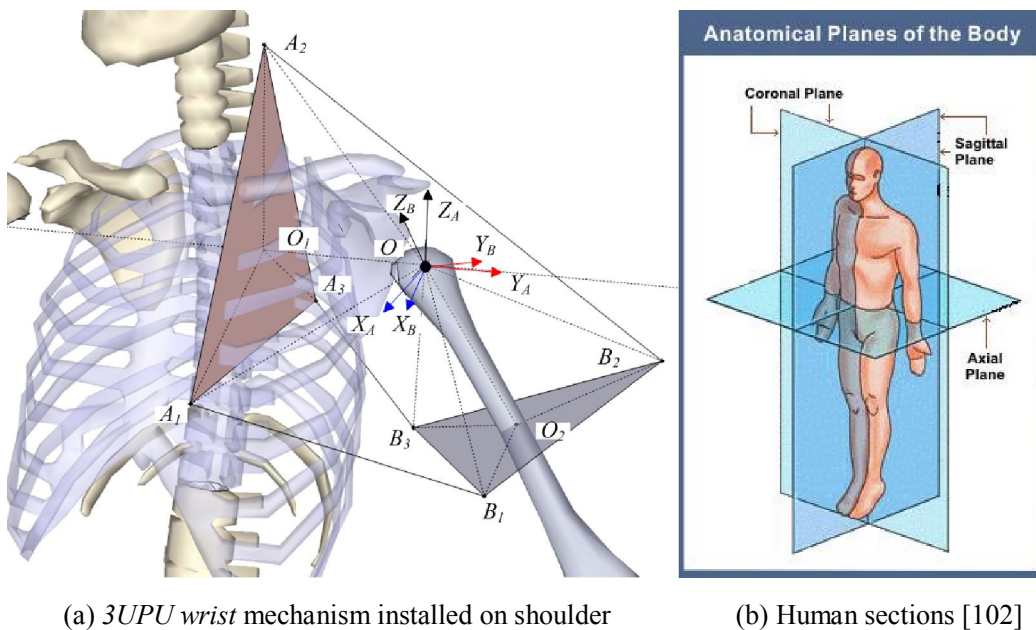


Figure 4-2. A 3UPU wrist mechanism applied on a left shoulder joint after rotation

Integrated with the human shoulder, the base coordinate frame  $\{O_A: X_A Y_A Z_A\}$  is set to be attached to a human torso. As illustrated in Figure 4-2(a), the coordinate frame origin coincides with a human's left shoulder rotation centre, and the frame coincides with the biomechanics coordinate frame introduced in Figure 2-1. Specifically, based on the middle planes in Figure 4-2(b) that divide the human torso in several sections, axis  $Z_A$  in frame  $\{O_A: X_A Y_A Z_A\}$  is defined as vertically pointing upwards, perpendicular to an axial plane, axis  $Y_A$  is perpendicular to a sagittal plane, pointing outwards to one's left; and axis  $X_A$  is perpendicular to a coronal plane, pointing to the front. The immobile base plane of the 3UPU wrist mechanism, represented by  $A_1 A_2 A_3$ , is attached to the human's left shoulder, in parallel with a sagittal plane, and  $\overline{O_1 O}$  coincides with axis  $Y_A$ .

Mobile coordinate frame  $\{O_B: X_B Y_B Z_B\}$  is attached to the mechanism's platform  $B_1 B_2 B_3$ , which is connected to the upper arm. The origin point  $O_B$  and the shoulder rotation centre  $O$  coincide. By simplifying the upper arm as a cylinder, axis  $Z_B$  and the axis of the upper limb cylinder are then superposed. The centre of the platform  $O_2$  is placed on the cylinder axis  $Y_B$  perpendicular to the upper arm's sagittal plane, pointing to the lateral left side of the arm, so that when plane  $A_1 A_2 A_3$  is perpendicular to plane  $B_1 B_2 B_3$ , which is the neutral position (Figure 4-1(b)) of the platform,  $Y_B$  superposes  $Y_A$ . The neutral position is illustrated in Figure 4-1b.  $X_B$  is determined by applying the right-hand rule, pointing anteriorly. Angle  $\alpha_{iB}$  denotes the angle between axis  $X_B$ 's projection in plane  $B_1 B_2 B_3$  and vector  $\overline{B_i O_2}$ , and angle  $\beta_B$  denotes the angle of  $\angle O_2 O_B B_i$ .

At the neutral position shown in Figure 4-1(b), where the rotation angles of the platform are defined as zeros, axis  $X_B$  and  $X_A$ ,  $Y_B$  and  $Y_A$ , as well as  $Z_B$  and  $Z_A$  coincide with each other. A rotated platform on the shoulder joint is shown in Figure 4-2(a).

In order to meet condition (2) of the 3UPU wrist mechanism, that the intermediate revolute axes on the two ends of each limb are in parallel, we assume  $\alpha_{iA} = \alpha_{iB}$  ( $i = 1, 2, 3$ ).

## 4.2 Kinematics of the 3UPU Wrist Mechanism

The kinematics of the 3UPU wrist mechanism has been studied by several researchers [43, 52, 98]. The straightforward inverse kinematics solutions and analytical forward kinematics solutions presented in this chapter are primarily based on their work, and are used as tools for developing an

alternative forward kinematics approach so that the orientation of the *3UPU wrist* platform could be analytically solved from their revolute joint angles rather than from the lengths of the limbs as in [101]. The alternative forward kinematics approach enables the *3UPU wrist* mechanism to adapt to the conditions such as those where normal motor and gear actuation (rather than the linear actuator) are used.

#### 4.2.1 Inverse Kinematics

The process of inverse kinematics of the *3UPU wrist* mechanism is to calculate the orientation and length of the three limbs ( $\bar{l}_1, \bar{l}_2, \bar{l}_3$ ) based on the orientation information of the platform, in the form x-y-z Euler angles ( $\theta_x, \theta_y, \theta_z$ ). Normally the inverse kinematic solutions in parallel mechanisms are straightforward and uniquely mapped to the orientation of the platform [100].

The  $i$ th limb vector is defined as the vector originating from point  $A_i$  to  $B_i$ , shown as:

$$\bar{l}_i = \overline{A_i B_i} = \overline{B_i}^{\{O_A\}} - \overline{A_i}^{\{O_A\}} = R \overline{B_i}^{\{O_B\}} - \overline{A_i}^{\{O_A\}} \quad (i = 1, 2, 3) \quad (4-1)$$

Where  $\overline{A_i}^{\{O_A\}}$  and  $\overline{B_i}^{\{O_B\}}$  are geometric constants, in this case known as:

$$\begin{cases} \overline{A_i}^{\{O_A\}} = \bar{A}_i = (r_A \cdot \cos a_{iA}, -h_A, r_A \cdot \sin a_{iA})^T \\ \overline{B_i}^{\{O_B\}} = (r_B \cdot \cos a_{iB}, r_B \cdot \sin a_{iB}, -h_B)^T \end{cases} \quad (i = 1, 2, 3) \quad (4-2)$$

For the definition of  $r_B, r_A, h_B, h_A, \alpha_{iA}$  and  $\alpha_{iB}$ , please refer to Figure 4-1(b).

$R$  is the rotation matrix from coordinate frame  $\{O_B: X_B Y_B Z_B\}$  to  $\{O_A: X_A Y_A Z_A\}$ , calculated as the inverse of the rotation matrix from frame  $\{O_A\}$  to  $\{O_B\}$ :

$$R = (R_z(\theta_z) R_y(\theta_y) R_x(\theta_x))^{-1} = (R_z(\theta_z) R_y(\theta_y) R_x(\theta_x))^T \quad (4-3)$$

In it the unit rotation matrices for transforming coordinate frame axes are known as:

$$R_x(\theta_x) = \begin{pmatrix} 1 & 0 & 0 \\ 0 & \cos \theta_x & \sin \theta_x \\ 0 & -\sin \theta_x & \cos \theta_x \end{pmatrix} \quad (4-4)$$

$$R_y(\theta_y) = \begin{pmatrix} \cos \theta_y & 0 & -\sin \theta_y \\ 0 & 1 & 0 \\ \sin \theta_y & 0 & \cos \theta_y \end{pmatrix} \quad (4-5)$$

$$R_z(\theta_z) = \begin{pmatrix} \cos \theta_z & \sin \theta_z & 0 \\ -\sin \theta_z & \cos \theta_z & 0 \\ 0 & 0 & 1 \end{pmatrix} \quad (4-6)$$

Substituting Equations (4-4), (4-5) and (4-6) into Equation (4-3), the rotation matrix  $R$  is expressed by  $\theta_x$ ,  $\theta_y$  and  $\theta_z$  as:

$$R = \begin{pmatrix} \cos \theta_y \cos \theta_z & -\cos \theta_y \sin \theta_z & \sin \theta_y \\ \cos \theta_x \sin \theta_z + \sin \theta_x \sin \theta_y \cos \theta_z & \cos \theta_x \cos \theta_z - \sin \theta_x \sin \theta_y \sin \theta_z & -\cos \theta_y \sin \theta_x \\ \sin \theta_x \sin \theta_z - \cos \theta_x \sin \theta_y \cos \theta_z & \sin \theta_x \cos \theta_z + \cos \theta_x \sin \theta_y \sin \theta_z & \cos \theta_x \cos \theta_y \end{pmatrix} \quad (4-7)$$

Substituting Equations (4-2) and (4-7) into Equation (4-1), allows limb vectors  $\vec{l}_i$  ( $i = 1,2,3$ ) to be uniquely determined.

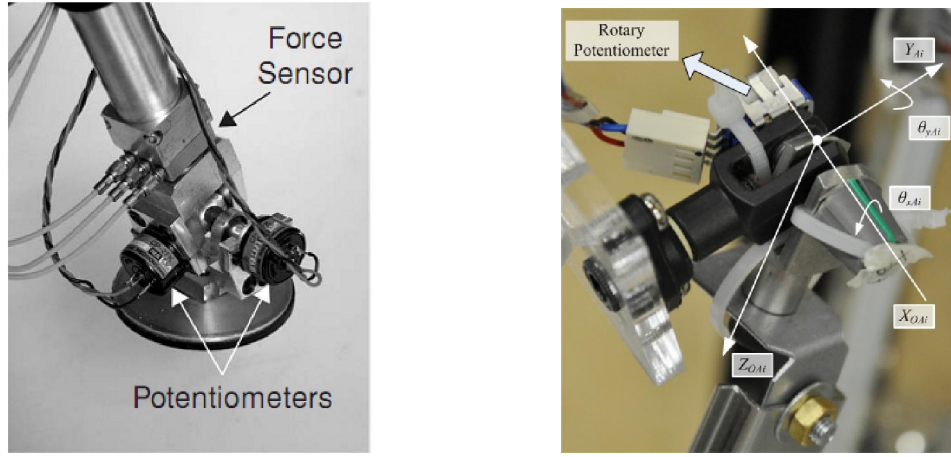
## 4.2.2 Forward Kinematics

Forward kinematics solves the problem of calculating the platform's orientation and position based on the joint motions. In parallel robots, usually the geometric lengths of limbs are used. Real time forward kinematics solutions for the shoulder exoskeleton are quite useful in trajectory tracking control. Solving forward kinematics for the *3UPU wrist* mechanism in real-time is accomplished by firstly obtaining the lengths of linear actuators in the limbs in real time and substituting them into kinematics equations. Although analytical forms of forward kinematics solutions for a parallel mechanism are normally difficult to obtain [103], for the *3UPU wrist* mechanism, [101] and [44] presented the so-called "semi-closed form solutions" which are eight groups of analytical solutions in the form of Euler angles as well as quaternions.

In some practical applications, measuring the length of the limb may not be easy because of limitations such as limited space for installing displacement sensors or insufficient sensor range in large scale robots. In such cases, conventional forward kinematics cannot be applied. In this section

we present an alternative forward kinematics approach for the *3UPU wrist* mechanism. It calculates the platform's orientation from angles of the universal joints that are adjacent to the base plane. Provided with existing technologies like the one introduced in [104] (Figure 4-3(a)) to in order to acquire both the revolute angles in a universal joint, this alternative approach is practical in implementation. Moreover, since the platform orientation can be calculated from the universal joints' angles, traditional motor-gear actuation can be used to control the *3UPU wrist* mechanism to track desired trajectories, with some sacrifices in system stiffness [105].

In accordance with the two types of devices that can obtain the universal joint's rotation angles in real-time (Figure 4-3), the alternative forward kinematics is carried out in two scenarios. In the Scenario One, we assume the device in Figure 4-3(a) is used and both angles of a universal joint are measured; and based on the six measured angles of all the three universal joints ( $A_1, A_2, A_3$ ) adjacent to the base, analytical solutions of the platform orientation ( $\theta_z, \theta_y, \theta_x$ ) are acquired. In Scenario Two, the number of input angles reduced to three--only one angle of each universal joint connected to the base ( $A_1, A_2, A_3$ ) is obtained. Based on them, the platform orientation ( $\theta_z, \theta_y, \theta_x$ ) is solved. In this scenario, we obtain 9 nonlinear equations containing nine highly coupled unknown variables ( $\theta_z, \theta_y, \theta_x, l_1, l_2, l_3, \theta_{yA1}, \theta_{yA2}, \theta_{yA3}$ ). Besides the three variables ( $\theta_z, \theta_y, \theta_x$ ) for platform orientation, the length of the limbs ( $l_1, l_2, l_3$ ) and the angle of the other axis in the universal joints ( $\theta_{yA1}, \theta_{yA2}, \theta_{yA3}$ ) are also involved in the nonlinear equations. The decoupling process is performed on these equations and eight groups of analytical orientation solutions ( $\theta_z, \theta_y, \theta_x$ ) are obtained. Scenario Two is implemented in the prototype experiments in Chapter 5. In the first scenario of the alternative forward kinematics approach, an angle-measuring-capable universal joint in the robot of [104] shown in Figure 4-3(a) is assumed to be used. In the second scenario, we designed and implemented a revolute joint pair that can measure one of the rotation angles (Figure 4-3(b)) to provide input data for calculating the platform's orientation.



(a) Angle-measuring-capable universal joint [104]      (b) Customised angle measurement device

Figure 4-3: Universal joints that are capable of acquiring rotation angles

### Scenario One

In the first scenario of this alternative forward kinematics approach, we presume that the angles of all the three universal joints connected to the base ( $\theta_{xAi}, \theta_{yAi}, i=1,2,3$ ) can be measured, such as the one shown in Figure 4-3(a) and are therefore known. Based on these angles the platform orientation ( $\theta_x, \theta_y, \theta_z$ ) can be calculated. The geometric presentation of these angles is shown in Figure 4-4(a).

According to Equation (4-7), in order to calculate the platform orientation expressed by angles ( $\theta_x, \theta_y, \theta_z$ ), a necessary step is to derive the rotation matrix  $R(\theta_z, \theta_y, \theta_x)$ . Thus the forward kinematics problem is converted to acquiring the nine variables ( $R_{mn}, m, n = 1, 2, 3$ ) in the rotation matrix  $R(\theta_z, \theta_y, \theta_x)$  as in Equation (4-8) based on the measured universal angles ( $\theta_{xAi}, \theta_{yAi}, i=1,2,3$ ).

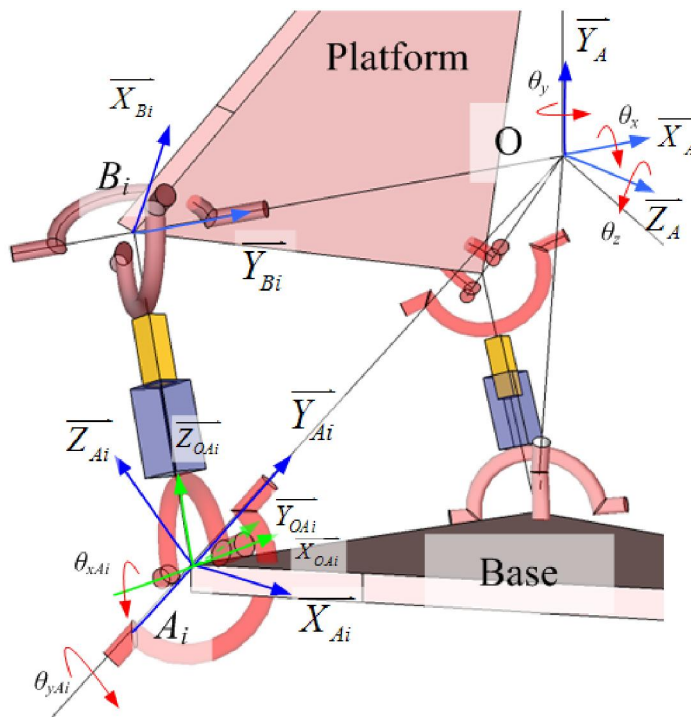
$$R = \begin{pmatrix} R_{11} & R_{12} & R_{13} \\ R_{21} & R_{22} & R_{23} \\ R_{31} & R_{32} & R_{33} \end{pmatrix} \quad (4-8)$$

Noting that in inverse kinematics, we already have the equations relating rotation matrix  $R(\theta_x, \theta_y, \theta_z)$  to the limb vector  $\bar{l}_i^{\{O_A\}}$ .

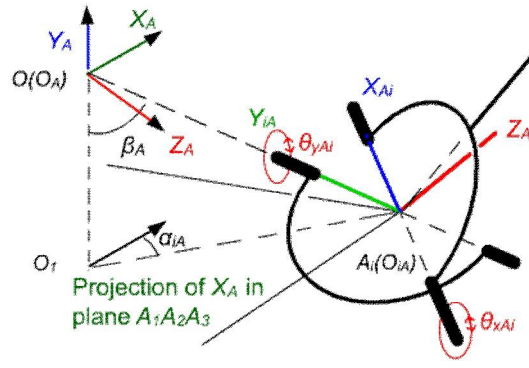
$$\bar{l}_i^{\{O_A\}} = \bar{l}_i = R\bar{B}_i^{\{O_B\}} - \bar{A}_i \quad (i = 1, 2, 3) \quad (4-9)$$

And in the following part of this section, we are going to use universal joint rotation angles ( $\theta_{x_{Ai}}$  and  $\theta_{y_{Ai}}$ ,  $i=1,2,3$ ) and the length of limb vectors  $l_i$  ( $i=1, 2, 3$ ) to characterise limb vector  $\vec{l}_i^{(O_{Ai})}$ , so that the relations of ( $\theta_{x_{Ai}}$  and  $\theta_{y_{Ai}}$ ,  $i=1, 2, 3$ ) and  $R(\theta_x, \theta_y, \theta_z)$  can be obtained.

In Figure 4-4(a) two local coordinate frames are defined. An immobile frame  $\{A_i: X_{Ai} Y_{Ai} Z_{Ai}, i=1, 2, 3\}$  is attached to the immobile part of the  $i$ th universal joint that is adjacent to the base. Its origin point and the universal joint's centre  $A_i$  coincide. Axis  $Y_{Ai}$  is pointing from  $A_i$  to  $O$ . Axis  $X_{Ai}$  is defined as the vector perpendicular to axis  $Y_{Ai}$  that is within plane  $A_1 A_2 A_3$ , and makes the right-hand rule determined axis  $Z_{Ai}$  face the side of the platform. Coordinate frame  $\{O_{Ai}: X_{O_{Ai}} Y_{O_{Ai}} Z_{O_{Ai}}\}$  is a mobile one. It is attached to the moving part of the  $i$ th universal joint that is adjacent to the base. The origin of frame  $\{O_{Ai}\}$  is also at point  $A_i$ . Axis  $Z_{O_{Ai}}$  coincides with the axis of the  $i$ th prismatic joint, pointing to the platform. Axis  $X_{O_{Ai}}$  is superimposed on the revolute axis of the universal joint that is connected to the limb, and it is on the same side of axis  $X_{Ai}$ .  $Y_{O_{Ai}}$  is determined by the right-hand rule.



(a). Immobile local coordinate frame  $\{A_i: X_{Ai} Y_{Ai} Z_{Ai}\}$  and mobile local coordinate frame  $\{O_{Ai}: X_{O_{Ai}} Y_{O_{Ai}} Z_{O_{Ai}}\}$  at universal joint  $A_i$



(b). Neutral position

Figure 4-4: Local coordinate frame and neutral position of the  $i$ th universal joint on the base

Transformation between the mobile coordinate frame  $\{O_{Ai}\}$  and the immobile coordinate frame  $\{A_i\}$  is described by rotation angles  $\theta_{xAi}$  and  $\theta_{yAi}$ . Rotation angles  $\theta_{xAi}$  and  $\theta_{yAi}$  are defined zero where coordinate frames  $\{O_{Ai}\}$  and  $\{A_i\}$  coincide, illustrated as the defined neutral position in Figure 4-4(b). Vectors in coordinate frame  $\{O_{Ai}\}$  are transformed to the immobile frame  $\{A_i\}$  by left multiplying the following rotation matrix:

$$R_{O_{Ai}} = \left( R_x(\theta_{xAi}) \cdot R_y(\theta_{yAi}) \right)^T = \begin{pmatrix} \cos \theta_{yAi} & 0 & -\sin \theta_{yAi} \\ \sin \theta_{xAi} \sin \theta_{yAi} & \cos \theta_{xAi} & \sin \theta_{xAi} \cos \theta_{yAi} \\ \cos \theta_{xAi} \sin \theta_{yAi} & -\sin \theta_{xAi} & \cos \theta_{xAi} \cos \theta_{yAi} \end{pmatrix} \quad (i = 1, 2, 3) \quad (4-10)$$

For practicability, we assume the angle range for  $(\theta_{xAi}, \theta_{yAi}, i=1, 2, 3)$  is  $(-\pi/2, \pi/2)$ .

Since axis  $Z_{O_{Ai}}$  in frame  $\{O_{Ai}\}$  always coincides with the limb vector, then in the mobile frame  $\{O_{Ai}\}$ , the limb vector is expressed as:

$$\bar{l}_i^{\{O_{Ai}\}} = (0, 0, l_i)^T \quad (i = 1, 2, 3) \quad (4-11)$$

Where  $l_i$  is the  $i$ th limb's length.

Then using the developed rotation matrix (Equation (4-10)), the limb vector's expression in frame  $\{A_i\}$  is:

$$\bar{l}_i^{\{A_i\}} = R_{O_{A_i}} \cdot \bar{l}_i^{\{O_{A_i}\}} = R_{O_{A_i}} \cdot (0, 0, l_i)^T \quad (i = 1, 2, 3) \quad (4-12)$$

Substituting Equations (4-10) and (4-11) into Equation (4-12), we get:

$$\bar{l}_i^{\{A_i\}} = l_i \cdot (-\sin \theta_{x_{A_i}}, \cos \theta_{x_{A_i}} \sin \theta_{y_{A_i}}, \cos \theta_{x_{A_i}} \cos \theta_{y_{A_i}})^T \quad (i = 1, 2, 3) \quad (4-13)$$

To achieve the goal of acquiring the limb vector's expression in the global coordinate frame  $\{O_A\}$

$\bar{l}_i^{\{O_A\}}$ , we need to find the coordinate rotation matrix  $R_{A_i}$  between the local immobile coordinate frame  $\{A_i\}$  and the global coordinate frame  $\{O_A\}$ , so that:

$$\bar{l}_i^{\{O_A\}} = R_{A_i} \cdot \bar{l}_i^{\{A_i\}} \quad (i = 1, 2, 3) \quad (4-14)$$

The rotation matrix from the coordinate frame  $\{A_i\}$  to the coordinate frame  $\{O_A\}$  is calculated in Equation (4-15) (the translation between coordinate frames  $\{A_i\}$  and  $\{O_A\}$  is neglected because it is offset when calculating vectors).

$$R_{A_i} = \left( R_x(-\beta_A) \cdot R_y(\pi/2 - \alpha_{iA}) \right)^T = \begin{pmatrix} \sin \alpha_{iA} & -\cos \alpha_{iA} \sin \beta_A & \cos \alpha_{iA} \cos \beta_A \\ 0 & \cos \beta_A & \sin \beta_A \\ -\cos \alpha_{iA} & -\sin \alpha_{iA} \sin \beta_A & \sin \alpha_{iA} \cos \beta_A \end{pmatrix} \quad (4-15)$$

Since this rotation transformation is between the two immobile coordinate frames, and the geometric constants  $\alpha_{iA}$ ,  $\beta_A$  are already defined in Figure 4-1(b),  $R_{A_i}$  ( $i = 1, 2, 3$ ) is therefore a constant matrix.

Substitute equations (4-15) and (4-13) into (4-14), the universal joint angles  $(\theta_{x_{A_i}}, \theta_{y_{A_i}})$  are then related to the rotation matrix  $R(\theta_x, \theta_y, \theta_z)$  as:

$$\bar{l}_i^{\{O_A\}} = R_{A_i} \cdot R_{O_{A_i}}(\theta_{y_{A_i}}, \theta_{x_{A_i}}) \cdot (0, 0, l_i)^T = R \bar{B}_i^{\{O_B\}} - \bar{A}_i \quad (i = 1, 2, 3) \quad (4-16)$$

Where  $l_i$ , and  $R(\theta_x, \theta_y, \theta_z)$  are unknown variables.

Rewriting Equation (4-16), we get:

$$l_i \cdot (t_{13-i}, t_{23-i}, t_{33-i})^T = \bar{A}_i - R\bar{B}_i^{(O_B)} \quad (i = 1, 2, 3) \quad (4-17)$$

in which  $(t_{13-i}, t_{23-i}, t_{33-i})^T$  are the known elements from the dot product of two rotation matrices.

$$R_{Ai} \cdot R_{OAi} = \begin{pmatrix} t_{11-i} & t_{12-i} & t_{13-i} \\ t_{21-i} & t_{22-i} & t_{23-i} \\ t_{31-i} & t_{32-i} & t_{33-i} \end{pmatrix} \quad (i = 1, 2, 3) \quad (4-18)$$

Applying identical transformations on equation (4-17) and squaring both sides of the equation, we obtain a  $2^{nd}$  order equation of  $l_i$ .

$$(t_{13-i}^2 + t_{23-i}^2 + t_{33-i}^2)l_i^2 - 2(A_{ix}t_{13-i} + A_{iy}t_{23-i} + A_{iz}t_{33-i})l_i + |\bar{A}_i|^2 - |\bar{B}_i|^2 = 0 \quad (i = 1, 2, 3) \quad (4-19)$$

the solutions of which are:

$$l_i = \frac{(A_{ix}t_{13-i} + A_{iy}t_{23-i} + A_{iz}t_{33-i})}{(t_{13-i}^2 + t_{23-i}^2 + t_{33-i}^2)} \pm \frac{\sqrt{(A_{ix}t_{13-i} + A_{iy}t_{23-i} + A_{iz}t_{33-i})^2 - (t_{13-i}^2 + t_{23-i}^2 + t_{33-i}^2) \times (|\bar{A}_i|^2 - |\bar{B}_i|^2)}}{(t_{13-i}^2 + t_{23-i}^2 + t_{33-i}^2)} \quad (i = 1, 2, 3) \quad (4-20)$$

Two possible solutions for the  $i$ th limb's length are acquired Equation (4-20). And in total, eight groups of possible solutions of  $(l_1, l_2, l_3)$  are obtained.

Substituting solutions of  $l_i$  and Equation (4-18) into equation (4-17), then for each  $i$  ( $i = 1, 2, 3$ ), Equation (4-17) provides three equations related to the nine unknown matrix elements  $R_{mn}$ , ( $m, n = 1, 2, 3$ ), as in Equation (4-21)

$$\begin{cases} R_{11}B_{ix} + R_{12}B_{iy} + R_{13}B_{iz} = A_{ix}' - l_1t_{13-1} \\ R_{21}B_{ix} + R_{22}B_{iy} + R_{23}B_{iz} = A_{iy}' - l_1t_{23-1} \\ R_{31}B_{ix} + R_{32}B_{iy} + R_{33}B_{iz} = A_{iz}' - l_1t_{33-1} \end{cases} \quad (i = 1, 2, 3) \quad (4-21)$$

Equation group (4-21) provide us nine equations, then the nine unknown variables ( $R_{mn}$ ,  $m, n = 1, 2,$

3) in the rotation matrix  $R(\theta_x, \theta_y, \theta_z)$  can be obtained. After the rotation matrix is calculated, substituting the solutions into Equation (4-7), the platform orientation  $(\theta_x, \theta_y, \theta_z)$  is then determined in Equation (4-22)

$$\begin{cases} \theta_y = \arcsin(R_{13}) & -\frac{\pi}{2} < \theta_y < \frac{\pi}{2} \\ \theta_x = \arctan(-R_{23} / R_{33}) & -\frac{\pi}{2} < \theta_x < \frac{\pi}{2} \\ \theta_z = \arctan(-R_{12} / R_{11}) & -\frac{\pi}{2} < \theta_z < \frac{\pi}{2} \end{cases} \quad (4-22)$$

With two solutions for each  $l_i$  ( $i=1, 2, 3$ ), there are in total of eight combinations of possible solutions for  $(l_1, l_2, l_3)$ , and accordingly eight possible solutions of rotation matrix elements  $(R_{mn}, m, n = 1, 2, 3)$ ; and thus eight possible solutions for the platform orientation  $(\theta_x, \theta_y, \theta_z)$ . Restrictions such as limb length range (minimum length to maximum length) and the relationships of the rotation matrix's elements in forms of mathematical equations help to rule out impractical solutions.

Scenario One of the forward kinematics approach can also be geometrically demonstrated. As illustrated in Figure 4-5, at each universal joint adjacent to the base, the rotation angles  $(\theta_{xA_i}, \theta_{yA_i})$  have uniquely determined the limb vector's direction; in the graph it is represented by the unit vector  $\vec{s}_i$ . Then the centre of the  $i$ th universal joint adjacent to platform (represented as  $B_i$ ) should be along the direction of the limb. To find the position of  $B_i$ , in plane  $OA_iB_i$ , a circle is plotted with a radius of  $OB_i$ , the intersections of the circle and the limb vector  $\vec{s}_i$  are then the positions of  $B_i$ . In this way, two  $B_i$  positions can be obtained on each limb, hence in total there are eight combinations for  $l_i$ , which matches the results of Equation (4-20). Each group of solutions' validity is verified in the visual way of plotting circles centred at  $B_i$ , with radius in constant lengths of  $B_1B_2$ ,  $B_2B_3$  and  $B_1B_3$ .

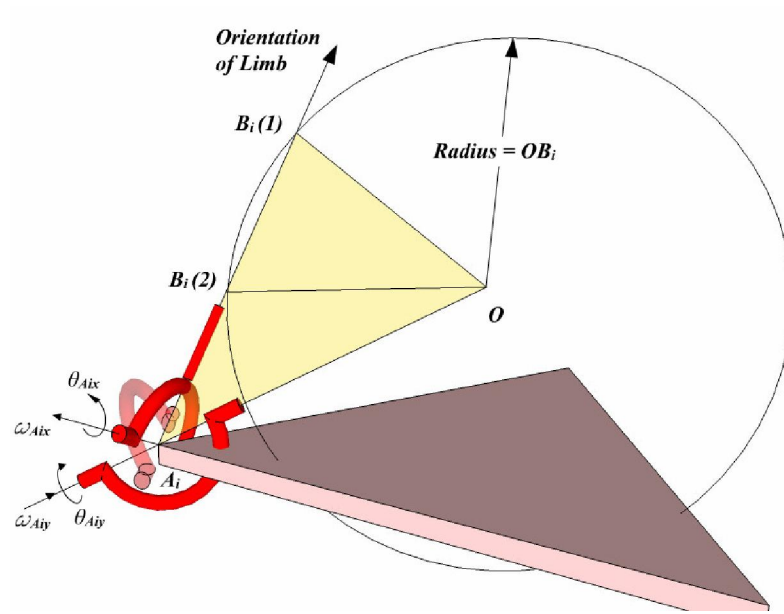


Figure 4-5: Visual illustration of the passive forward kinematics approach

A simple example is presented to demonstrate the approach of Scenario One. The geometric constants for this example are displayed as follows.

$$\begin{cases} \bar{A}_1 = (0, -29.825, 51.658) \\ \bar{A}_2 = (-44.7371, -25.829, 86.43) \\ \bar{A}_3 = (44.7371, -29.825, -25.83) \end{cases} \quad \begin{cases} \bar{B}_1^{\{O_B\}} = (0, 94.9, -86.43) \\ \bar{B}_2^{\{O_B\}} = (44.7371, -25.829, -86.43) \\ \bar{B}_3^{\{O_B\}} = (44.7371, -25.8290, -86.43) \end{cases}$$

In this example we assume the platform is at the position of  $(\theta_x = 0^\circ, \theta_y = 45^\circ, \theta_z = 45^\circ)$ . From (4-16) and (4-10) we can obtain the universal joint angles as  $(\theta_{yA1} = -64.716^\circ, \theta_{xA1} = -41.179^\circ, \theta_{yA2} = -88.425^\circ, \theta_{xA2} = 76.885^\circ, \theta_{yA3} = 75.7441^\circ, \theta_{xA3} = -23.8481^\circ)$  respectively.

Then the product of rotation matrix  $R_{A_i} \cdot R_{OA_i}(\theta_{yi}, \theta_{xi})$  is calculated from Equations (4-15) and (4-16) as:

$$\begin{cases} R_{A1} \cdot R_{O A1} = \begin{pmatrix} 0.4271 & 0.5953 & -0.6805 \\ 0.7831 & 0.1328 & 0.6076 \\ 0.4521 & -0.7924 & -0.4095 \end{pmatrix} \\ R_{A2} \cdot R_{O A2} = \begin{pmatrix} -0.4466 & 0.6454 & -0.6197 \\ 0.8657 & 0.1366 & -0.4816 \\ -0.2261 & -0.7516 & -0.6197 \end{pmatrix} \\ R_{A3} \cdot R_{O A3} = \begin{pmatrix} -0.5428 & 0.5331 & -0.6489 \\ -0.8394 & 0.3711 & 0.3972 \\ 0.0290 & 0.7603 & 0.6489 \end{pmatrix} \end{cases}$$

Substituting the above results into Equation (4-20),  $l_i$  ( $i = 1, 2, 3$ ) is calculated as:

$$\begin{cases} l_1(1) = -80.9774 & l_2(1) = -157.8718 & l_3(1) = -60.5132 \\ l_1(2) = 159.5270 & l_2(2) = 41.6830 & l_3(2) = 108.7461 \end{cases}$$

where each length  $l_i$  has two possible solutions.

Substituting the positive solutions of  $l_i$  ( $l_1 = 159.5270$ ,  $l_2 = 41.6830$ ,  $l_3 = 108.741$ ) into Equation (4-16), The rotation matrix  $R(\theta_x, \theta_y, \theta_z)$  is obtained and accordingly rotation angles of platform ( $\theta_x, \theta_y, \theta_z$ ) are solved from Equation (4-22) as ( $\theta_x = -3.4815^\circ$ ,  $\theta_y = 47.4355^\circ$ ,  $\theta_z = 44.3940^\circ$ ). Comparing to the input rotation angles ( $\theta_x = 0^\circ$ ,  $\theta_y = 45^\circ$ ,  $\theta_z = 45^\circ$ ), the result of Scenario One forward kinematics is acceptable, with around  $3^\circ$  to  $4^\circ$  round-off error.

## Scenario Two

In Scenario Two we use devices like the one in Figure 4-3b to measure one ( $\theta_{x Ai}$ ,  $i = 1, 2, 3$ ) of the two rotation angles ( $\theta_{x Ai}$  or  $\theta_{y Ai}$ ,  $i = 1, 2, 3$ ) of the three universal joints connected to the base. Then the platform's orientation ( $\theta_x, \theta_y, \theta_z$ ) is calculated based on them ( $\theta_{x Ai}$ ,  $i = 1, 2, 3$ ). Theoretically, it's also possible to calculate ( $\theta_x, \theta_y, \theta_z$ ) from the other group of angles ( $\theta_{y Ai}$ ,  $i = 1, 2, 3$ ), but in this thesis we only discuss solving ( $\theta_x, \theta_y, \theta_z$ ) from ( $\theta_{x Ai}$ ,  $i = 1, 2, 3$ ).

To analyse the solvability of this problem, the essential Equation (4-16) that relates the universal joints' local rotation angles ( $\theta_{y Ai}$  and  $\theta_{x Ai}$ ,  $i = 1, 2, 3$ ) with the platform's rotation angles ( $\theta_x, \theta_y, \theta_z$ ) provides nine scalar equations (equations in axis  $X$ ,  $Y$  and  $Z$  when  $i = 1, 2, 3$ ), while in Scenario Two there are exactly nine unknown variables to solve:  $l_i$  ( $i = 1, 2, 3$ ),  $\theta_{y Ai}$  ( $i = 1, 2, 3$ ) and  $\theta_x, \theta_y, \theta_z$ .

Hence, this question is solvable and in the following study, the way  $(\theta_x, \theta_y, \theta_z)$  are also solved from Equation (4-16) is presented. Since Equation (4-16) is nonlinear and variables  $(l_i, \theta_{yAi}, (i = 1, 2, 3))$  and  $\theta_x, \theta_y, \theta_z$  are highly coupled, the process of solving them involves decoupling process.

For convenience, Equation (4-16) is rewritten here again as

$$\bar{l}_i^{\{O_A\}} = R_{Ai} \cdot R_{OAi}(\theta_{yAi}, \theta_{xAi}) \cdot (0, 0, l_i)^T = R\bar{B}_i^{\{O_B\}} - \bar{A}_i \quad (i = 1, 2, 3) \quad (4-23)$$

The way of decoupling is to firstly obtain the relationship of  $l_i$  ( $i = 1, 2, 3$ ) and  $\theta_{yAi}$  ( $i = 1, 2, 3$ ) and remove variables  $(\theta_x, \theta_y, \theta_z)$  from Equation (4-23).

Based on Equation (4-10), the product of the rotation matrices  $R_{Ai}$  and  $R_{OAi}$  is expressed as:

$$R_{Ai} \cdot R_{OAi} = R_{Ai} \cdot (R_x(\theta_{xAi}) \cdot R_y(\theta_{yAi}))^T = R_{Ai} \cdot R_y(\theta_{yAi})^T \cdot R_x(\theta_{xAi})^T \quad (i = 1, 2, 3) \quad (4-24)$$

Substituting Equation (4-24) into Equation (4-16), we get:

$$l_i \begin{pmatrix} R_{Ai-11} \cos \theta_{xAi} \sin \theta_{yAi} - R_{Ai-12} \sin \theta_{xAi} + R_{Ai-13} \cos \theta_{xAi} \cos \theta_{yAi} \\ R_{Ai-21} \cos \theta_{xAi} \sin \theta_{yAi} - R_{Ai-22} \sin \theta_{xAi} + R_{Ai-23} \cos \theta_{xAi} \cos \theta_{yAi} \\ R_{Ai-31} \cos \theta_{xAi} \sin \theta_{yAi} - R_{Ai-32} \sin \theta_{xAi} + R_{Ai-33} \cos \theta_{xAi} \cos \theta_{yAi} \end{pmatrix} = R\bar{B}_i^{\{O_B\}} - \begin{pmatrix} A_{ix} \\ A_{iy} \\ A_{iz} \end{pmatrix} \quad (i = 1, 2, 3) \quad (4-25)$$

Rewriting this equation, we get:

$$l_i \begin{pmatrix} R_{Ai-11} \cos \theta_{xAi} \sin \theta_{yAi} - R_{Ai-12} \sin \theta_{xAi} + R_{Ai-13} \cos \theta_{xAi} \cos \theta_{yAi} \\ R_{Ai-21} \cos \theta_{xAi} \sin \theta_{yAi} - R_{Ai-22} \sin \theta_{xAi} + R_{Ai-23} \cos \theta_{xAi} \cos \theta_{yAi} \\ R_{Ai-31} \cos \theta_{xAi} \sin \theta_{yAi} - R_{Ai-32} \sin \theta_{xAi} + R_{Ai-33} \cos \theta_{xAi} \cos \theta_{yAi} \end{pmatrix} + \begin{pmatrix} A_{ix} \\ A_{iy} \\ A_{iz} \end{pmatrix} = \bar{K}_i = \begin{pmatrix} K_{ix} \\ K_{iy} \\ K_{iz} \end{pmatrix} = R\bar{B}_i^{\{O_B\}} \quad (i = 1, 2, 3) \quad (4-26)$$

Squaring both sides of Equation (4-26) we obtain the following  $2^{nd}$  order polynomial equation of  $l_i$  ( $i=1, 2, 3$ ):

$$l_i^2 + A_i^2 + 2l_i \sin \theta_{yAi} \cos \theta_{xAi} \bar{A}_i \cdot R_{Ai-1} + 2l_i \cos \theta_{yAi} \cos \theta_{xAi} \bar{A}_i \cdot R_{Ai-3} - 2l_i \sin \theta_{xAi} \bar{A}_i \cdot R_{Ai-2} = B_i^2 \quad (i = 1, 2, 3) \quad (4-27)$$

in which the following short forms are used:

$$\begin{cases} R_{Ai-1} = (R_{Ai-11} & R_{Ai-21} & R_{Ai-31})^T \\ R_{Ai-2} = (R_{Ai-12} & R_{Ai-22} & R_{Ai-32})^T \\ R_{Ai-3} = (R_{Ai-13} & R_{Ai-23} & R_{Ai-33})^T \\ \bar{A}_i = (A_{ix} & A_{iy} & A_{iz})^T \end{cases} \quad (i = 1, 2, 3) \quad (4-28)$$

In Equation (4-27), the value of parameters ( $\bar{A}_i, R_{Ai-1}, R_{Ai-2}, R_{Ai-3}, A_i, B_i, \theta_{xAi}, i = 1, 2, 3$ ) are known, so that the relation of  $l_i$  ( $i = 1, 2, 3$ ) and  $\theta_{yAi}$  ( $i = 1, 2, 3$ ) are obtained. However, to solve these six variables ( $l_i, \theta_{yAi}, i = 1, 2, 3$ ), the three equations from (4-27) are not sufficient.

Note that the distance between any two universal centre points on the platform ( $B_i, i = 1, 2, 3$ ) should be constant. Mathematically, from Equation (4-26) we can obtain:

$$\begin{cases} RB_1^{\{O_B\}} - RB_2^{\{O_B\}} = \bar{K}_1(l_1, \theta_{yA1}) - \bar{K}_2(l_2, \theta_{yA2}) \\ RB_2^{\{O_B\}} - RB_3^{\{O_B\}} = \bar{K}_2(l_2, \theta_{yA2}) - \bar{K}_3(l_3, \theta_{yA3}) \\ RB_3^{\{O_B\}} - RB_1^{\{O_B\}} = \bar{K}_3(l_3, \theta_{yA3}) - \bar{K}_1(l_1, \theta_{yA1}) \end{cases} \quad (4-29)$$

in which the definition of  $\bar{K}_i$  ( $i = 1, 2, 3$ ) is presented in Equation (4-26), and  $\bar{K}_i(l_i, \theta_{yAi})$  ( $i = 1, 2, 3$ ) denotes  $\bar{K}_i$  a vector containing ( $l_i, \theta_{yAi}, i = 1, 2, 3$ ) as variables.

Squaring both sides of the three equations in Equation (4-29), then  $R(\theta_x, \theta_y, \theta_z)$  is removed. Then substituting the constant values of  $B_i^{\{O_B\}}$  ( $i = 1, 2, 3$ ) from Equation (4-2) into the above equation, we obtain another three equations relating  $l_i$  ( $i = 1, 2, 3$ ) and  $\theta_{yAi}$  ( $i = 1, 2, 3$ ) as follows:

$$\begin{cases} B_1^2 + B_2^2 - 2\bar{K}_1(l_1, \theta_{yA1}) \cdot \bar{K}_2(l_2, \theta_{yA2}) = |B_1^{\{O_B\}} - B_2^{\{O_B\}}|^2 = r_B^2 \left( (\cos a_{1B} - \cos a_{2B})^2 + (\sin a_{1B} - \sin a_{2B})^2 \right) \\ B_2^2 + B_3^2 - 2\bar{K}_2(l_2, \theta_{yA2}) \cdot \bar{K}_3(l_3, \theta_{yA3}) = |B_2^{\{O_B\}} - B_3^{\{O_B\}}|^2 = r_B^2 \left( (\cos a_{2B} - \cos a_{3B})^2 + (\sin a_{2B} - \sin a_{3B})^2 \right) \\ B_3^2 + B_1^2 - 2\bar{K}_3(l_3, \theta_{yA3}) \cdot \bar{K}_1(l_1, \theta_{yA1}) = |B_3^{\{O_B\}} - B_1^{\{O_B\}}|^2 = r_B^2 \left( (\cos a_{3B} - \cos a_{1B})^2 + (\sin a_{3B} - \sin a_{1B})^2 \right) \end{cases} \quad (4-30)$$

in which  $r_B$  and  $\alpha_{iB}$  are determined geometric constants illustrated in Figure 4-1(b).

Rewriting Equation (4-27) as a 2<sup>nd</sup> order polynomial equation of  $\cos\theta_{yAi}$  in the following way, we get:

$$\begin{aligned}
& 4 \cos^2 \theta_{yAi} \cdot l_i^2 \left( (\bar{A}_i \cdot R_{Ai-3})^2 \cos^2 \theta_{xAi} + (\bar{A}_i \cdot R_{Ai-3})^2 \sin^2 \theta_{xAi} \right) - \\
& 4 \cos \theta_{yAi} l_i \bar{A}_i \cdot R_{Ai-3} \cos \theta_{xAi} \left( A_i^2 + l_i^2 - B_i^2 - 2l_i \sin \theta_{xAi} \bar{A}_i \cdot R_{Ai-2} \right) + \\
& \left( A_i^2 + l_i^2 - B_i^2 - 2l_i \sin \theta_{xAi} \bar{A}_i \cdot R_{Ai-2} \right)^2 - 4l_i^2 \cos^2 \theta_{xAi} (\bar{A}_i \cdot R_{Ai-1})^2 = 0 \quad (i = 1, 2, 3)
\end{aligned} \tag{4-31}$$

Then  $\cos\theta_{yAi}$  as a function of  $l_i$  is solved as:

$$\begin{aligned}
& \pm \sin \theta_{xAi} AR_{Ai-1} \sqrt{+4(l_i \sin \theta_{xAi} AR_{Ai-1})^2 - 4(l_i \sin \theta_{xAi} AR_{Ai-2})^2 + 4(l_i \cos \theta_{xAi} AR_{Ai-3})^2} \\
& \pm 4l_i (A_i^2 - B_i^2 + l_i^2) \sin \theta_{xAi} AR_{Ai-2} - (A_i^2 - B_i^2 + l_i^2)^2 \\
\cos \theta_{yAi} = & \frac{\mp AR_{Ai-3} (A_i^2 \cos \theta_{xAi} - B_i^2 \cos \theta_{xAi} + l_i^2 \cos \theta_{xAi} - 2l_i^2 \cos \theta_{xAi} \sin \theta_{xAi} AR_{Ai-2})}{2l_i (\sin \theta_{xAi} AR_{Ai-1} + \cos \theta_{xAi} AR_{Ai-3})} \quad (i = 1, 2, 3)
\end{aligned} \tag{4-32}$$

in which the following short-form is used:

$$AR_{Ai-i} = \bar{A}_i \cdot R_{Ai-1} \quad (i = 1, 2, 3)$$

Rewriting Equation (4-30), so that  $l_i$  ( $i = 1, 2, 3$ ) is related to  $\theta_{yAi}$  ( $i = 1, 2, 3$ ) in the following way:

$$\begin{aligned}
& |\bar{l}_i|^2 + |\bar{l}_j|^2 - 2R_{Ai} \cdot R_{OAi}(\theta_{yAi}) \cdot (0, 0, l_i)^T \cdot R_{Aj} \cdot R_{O Aj}(\theta_{yAj}) \cdot (0, 0, l_j)^T + |\bar{A}_j \bar{A}_i|^2 + 2(\bar{A}_i - \bar{A}_j) \cdot (\bar{l}_i - \bar{l}_j) = |\bar{B}_j \bar{B}_i|^2 \quad (i, j = 1, 2, 3)
\end{aligned} \tag{4-33}$$

Substituting the expression of  $\cos\theta_{yAi}$  with  $l_i$  as a variable, from Equation (4-32) into Equation (4-33), then it becomes three equations of  $l_i$  and  $l_j$  ( $i, j = 1, 2, 3$ ). Since equations of (4-33) are nonlinear, the numeric methods can be adopted to solve  $l_i$  ( $i = 1, 2, 3$ ). With two possible solutions for  $\cos\theta_{yAi}$  ( $i = 1, 2, 3$ ) in Equation (4-31), the number of solutions for  $l_i$  ( $i = 1, 2, 3$ ) from (4-33) should be two. Then in total there are eight combinations of possible solutions for  $(l_1, l_2, l_3)$ .

Given one determined group of  $l_i$  ( $i = 1, 2, 3$ ), angle  $\theta_{yAi}$  ( $i = 1, 2, 3$ ) is solved from Equations (4-31) or (4-27) as:

$$\theta_{yAi} = \arcsin\left(\frac{2l_i \bar{A}_i \cdot R_{Ai-1} \cos \theta_{xAi}}{B_i^2 - A_i^2 - l_i^2 + 2l_i \sin \theta_{xAi} \bar{A}_i \cdot R_{Ai-2}}\right) \quad (i = 1, 2, 3) \quad (4-34)$$

The next step is to obtain each element of the rotation matrix  $R(\theta_x, \theta_y, \theta_z)$  in the expression of  $l_i$  ( $i = 1, 2, 3$ ). Suppose based on the above approach the values of  $(l_1, l_2, l_3)$  and  $\theta_{yAi}$  ( $i = 1, 2, 3$ ) are already solved from Equations (4-33) and (4-34). Then vector  $\bar{K}_i = (K_{ix} \ K_{iy} \ K_{iz})^T$  ( $i = 1, 2, 3$ ) in Equation (4-26) are known. Thus the elements of the rotation matrix  $R(\theta_x, \theta_y, \theta_z)$  are solved as:

$$\left\{ \begin{array}{l} r_{11} = \frac{(B_{2y}B_{3z} - B_{2z}B_{3y})K_{1x} + (B_{1z}B_{3y} - B_{1y}B_{3z})K_{2x} + (B_{1y}B_{2z} - B_{1z}B_{2y})K_{3x}}{B_{1x}B_{2y}B_{3z} - B_{1x}B_{2z}B_{3y} - B_{1y}B_{2x}B_{3z} + B_{1y}B_{2z}B_{3x} + B_{1z}B_{2x}B_{3y} - B_{1z}B_{2y}B_{3x}} \\ r_{12} = \frac{(B_{2z}B_{3x} - B_{2x}B_{3z})K_{1x} + (B_{1x}B_{3z} - B_{1z}B_{3x})K_{2x} + (B_{1z}B_{2x} - B_{1x}B_{2z})K_{3x}}{B_{1x}B_{2y}B_{3z} - B_{1x}B_{2z}B_{3y} - B_{1y}B_{2x}B_{3z} + B_{1y}B_{2z}B_{3x} + B_{1z}B_{2x}B_{3y} - B_{1z}B_{2y}B_{3x}} \\ r_{13} = \frac{(B_{2x}B_{3y} - B_{2y}B_{3x})K_{1x} + (B_{1y}B_{3x} - B_{1x}B_{3y})K_{2x} + (B_{1x}B_{2y} - B_{1y}B_{2x})K_{3x}}{B_{1x}B_{2y}B_{3z} - B_{1x}B_{2z}B_{3y} - B_{1y}B_{2x}B_{3z} + B_{1y}B_{2z}B_{3x} + B_{1z}B_{2x}B_{3y} - B_{1z}B_{2y}B_{3x}} \end{array} \right. \quad (4-35)$$

$$\left\{ \begin{array}{l} r_{21} = \frac{(B_{2y}B_{3z} - B_{2z}B_{3y})K_{1y} + (B_{1z}B_{3y} - B_{1y}B_{3z})K_{2y} + (B_{1y}B_{2z} - B_{1z}B_{2y})K_{3y}}{B_{1x}B_{2y}B_{3z} - B_{1x}B_{2z}B_{3y} - B_{1y}B_{2x}B_{3z} + B_{1y}B_{2z}B_{3x} + B_{1z}B_{2x}B_{3y} - B_{1z}B_{2y}B_{3x}} \\ r_{22} = \frac{(B_{2z}B_{3x} - B_{2x}B_{3z})K_{1y} + (B_{1x}B_{3z} - B_{1z}B_{3x})K_{2y} + (B_{1z}B_{2x} - B_{1x}B_{2z})K_{3y}}{B_{1x}B_{2y}B_{3z} - B_{1x}B_{2z}B_{3y} - B_{1y}B_{2x}B_{3z} + B_{1y}B_{2z}B_{3x} + B_{1z}B_{2x}B_{3y} - B_{1z}B_{2y}B_{3x}} \\ r_{23} = \frac{(B_{2x}B_{3y} - B_{2y}B_{3x})K_{1y} + (B_{1y}B_{3x} - B_{1x}B_{3y})K_{2y} + (B_{1x}B_{2y} - B_{1y}B_{2x})K_{3y}}{B_{1x}B_{2y}B_{3z} - B_{1x}B_{2z}B_{3y} - B_{1y}B_{2x}B_{3z} + B_{1y}B_{2z}B_{3x} + B_{1z}B_{2x}B_{3y} - B_{1z}B_{2y}B_{3x}} \end{array} \right. \quad (4-36)$$

$$\left\{ \begin{array}{l} r_{31} = \frac{(B_{2y}B_{3z} - B_{2z}B_{3y})K_{1z} + (B_{1z}B_{3y} - B_{1y}B_{3z})K_{2z} + (B_{1y}B_{2z} - B_{1z}B_{2y})K_{3z}}{B_{1x}B_{2y}B_{3z} - B_{1x}B_{2z}B_{3y} - B_{1y}B_{2x}B_{3z} + B_{1y}B_{2z}B_{3x} + B_{1z}B_{2x}B_{3y} - B_{1z}B_{2y}B_{3x}} \\ r_{32} = \frac{(B_{2z}B_{3x} - B_{2x}B_{3z})K_{1z} + (B_{1x}B_{3z} - B_{1z}B_{3x})K_{2z} + (B_{1z}B_{2x} - B_{1x}B_{2z})K_{3z}}{B_{1x}B_{2y}B_{3z} - B_{1x}B_{2z}B_{3y} - B_{1y}B_{2x}B_{3z} + B_{1y}B_{2z}B_{3x} + B_{1z}B_{2x}B_{3y} - B_{1z}B_{2y}B_{3x}} \\ r_{33} = \frac{(B_{2x}B_{3y} - B_{2y}B_{3x})K_{1z} + (B_{1y}B_{3x} - B_{1x}B_{3y})K_{2z} + (B_{1x}B_{2y} - B_{1y}B_{2x})K_{3z}}{B_{1x}B_{2y}B_{3z} - B_{1x}B_{2z}B_{3y} - B_{1y}B_{2x}B_{3z} + B_{1y}B_{2z}B_{3x} + B_{1z}B_{2x}B_{3y} - B_{1z}B_{2y}B_{3x}} \end{array} \right. \quad (4-37)$$

With all elements in rotation matrix  $R(\theta_x, \theta_y, \theta_z)$  determined, eight groups of the rotation angles  $\theta_x$ ,  $\theta_y$  and  $\theta_z$  are then acquired from (4-7).

Scenario Two of the alternative forward kinematics is implemented in the experiment in Chapter 5, in which the calculation results are compared with orientation angle data from an orientation sensor,

and the validity and performance of this method is evaluated in Chapter 5

This alternative forward kinematics approach can also be demonstrated in geometric way. As illustrated in Figure 4-6, the surface of the sphere whose radius equals  $|B_i|$  and whose centre coincides with the rotation centre  $O$  represents the set of all the possible  $B_i$  points. In this case the distance from  $B_i$  to  $O$  in all three limbs are the same, therefore only one sphere is generated. Then, given the specific rotation angles of each universal joint's  $\theta_{xAi}$ , a circular cone is generated for each universal joint, with each cone's apex angle determined by  $\theta_{xAi}$ , and the cone's axis aligned with the universal joint's axis  $Y_{Ai}$ , indicating free rotation around axis  $Y_{Ai}$ . Thus the conical surface of the circular cone represents a set of all the possible tracks of the limb vector, while rotation angles around the axis  $Y_{Ai}$  ( $\theta_{yAi}$ ) are still undetermined. The intersection closed form curves of the circular cones and the sphere are generated. They characterise the set of position solutions for  $B_i$ , when both conditions (distance of  $|B_i|$  as well as universal rotation angles  $\theta_{xAi}$ ) are considered. The corresponding mathematical expression is in Equation (4-30). Finally by applying the condition of constant distances between  $B_1B_2$ ,  $B_2B_3$  and  $B_3B_1$  (Equation (4-30)), we could employ numeric methods to determine the exact position of  $B_i$  along the intersection curves.

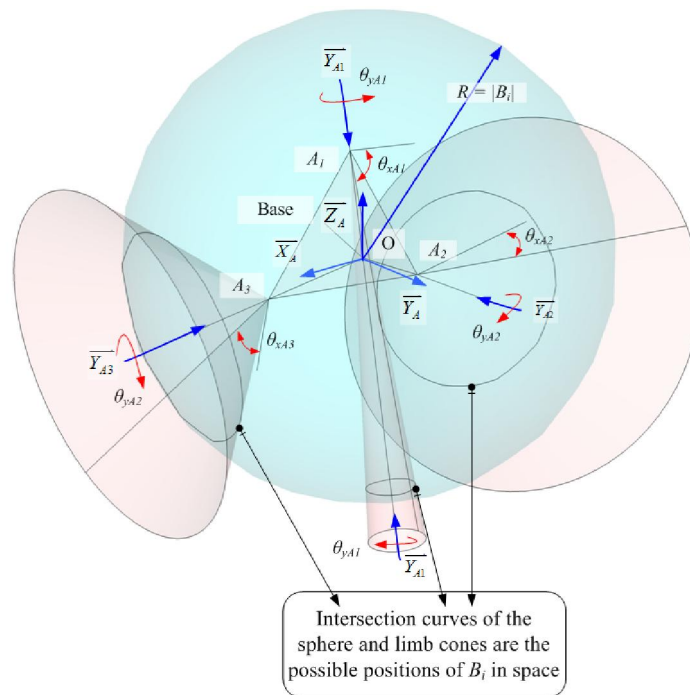


Figure 4-6: Geometric illustration of Scenario Two of the alternative forward kinematics

### 4.3 Other Related Works of *3UPU Wrist* Mechanism

#### **Workspace Optimisation based on Previous Tools**

Inverse kinematics and forward kinematics tools enables us to perform an optimisation towards the goal of optimising various geometric variables in the design to obtain the group of variables that provide the largest workspace. Details of this optimisation are presented in Appendix C . Although we did not implement the optimal results on the practical prototype, the workspace optimisation is still significant in determining optimal design for larger workspace in the future.

#### **Shoulder Joint Reaction Force Analysis**

When implementing a parallel mechanism onto the human shoulder, one critical safety issue is the resultant reaction force transmitted from the mechanism onto the human shoulder joint. In Appendix D we analysed the forces transmitted onto the human shoulder joint when a *3UPU wrist* mechanism is applied as an exoskeleton robot. The way of calculating the shoulder joint reaction force is presented. The experiment to test this analysis was not accomplished, thus this force analysis listed in the Appendix only provide a theoretical approach.

# Chapter 5 Prototype Development and Experimental Verification

## 5.1 The 3UPU Wrist Mechanism Kinematics Experiment

Despite multiple literatures discussing the kinematics and dynamic attributes of the *3UPU wrist* mechanism [42, 51, 54, 97], no practically manufactured *3UPU wrist* mechanisms were introduced in the literature. By developing a test rig that meets the geometric requirements of a *3UPU wrist* parallel mechanism, our objective is to examine the practicability of the *3UPU wrist* mechanism as well as the alternative forward kinematics introduced in Section 4.2.2. Static replication tests at the beginning of the experiment are performed on the test rig to validate the kinematics of the *3UPU wrist* mechanism. Then, as the customised universal joints adjacent to the base are capable of acquiring rotation angles in real time, Scenario Two of the proposed alternative forward kinematics is implemented to calculate the *3UPU wrist* mechanism's orientation. The calculation results are compared to the directly obtained orientation data through an inertial measurement unit (IMU) sensor.

### 5.1.1 The Test Rig

The test rig, illustrated in Figure 5-1 is made mostly from off-the-shelf parts and rapid prototyping components, and the base and platform plane are made of acrylic; the same geometric dimensions apply to both the base and the platform. Three pairs of customised orthogonal revolute joints are installed on the tilted standing brackets of the base plane. Alongside axis  $X_{Ai}$  of each customised orthogonal joint pair, a low friction, detention-free rotary potentiometer is mounted, so that the relative rotation angle around axis  $X_{Ai}$  is recorded. Details of this joint pair are shown in Figure 5-1(c). The measurement range of the rotary potentiometer is roughly  $-150^\circ$  to  $150^\circ$  away from the centre position, thus it is sufficient to detect the rotation angles around axis  $X_{Ai}$ . The local coordinate frame of the IMU sensor indicated in (shown Figure 5-1(b)) coincides with the coordinate frame of the platform  $\{O_B\}$ . It is used to obtain the orientation of the platform plane relative to the earth's magnetic field and eventually acquires the rotation angles of the platform relative to the base. This test rig is actuated by hand in this experiment.

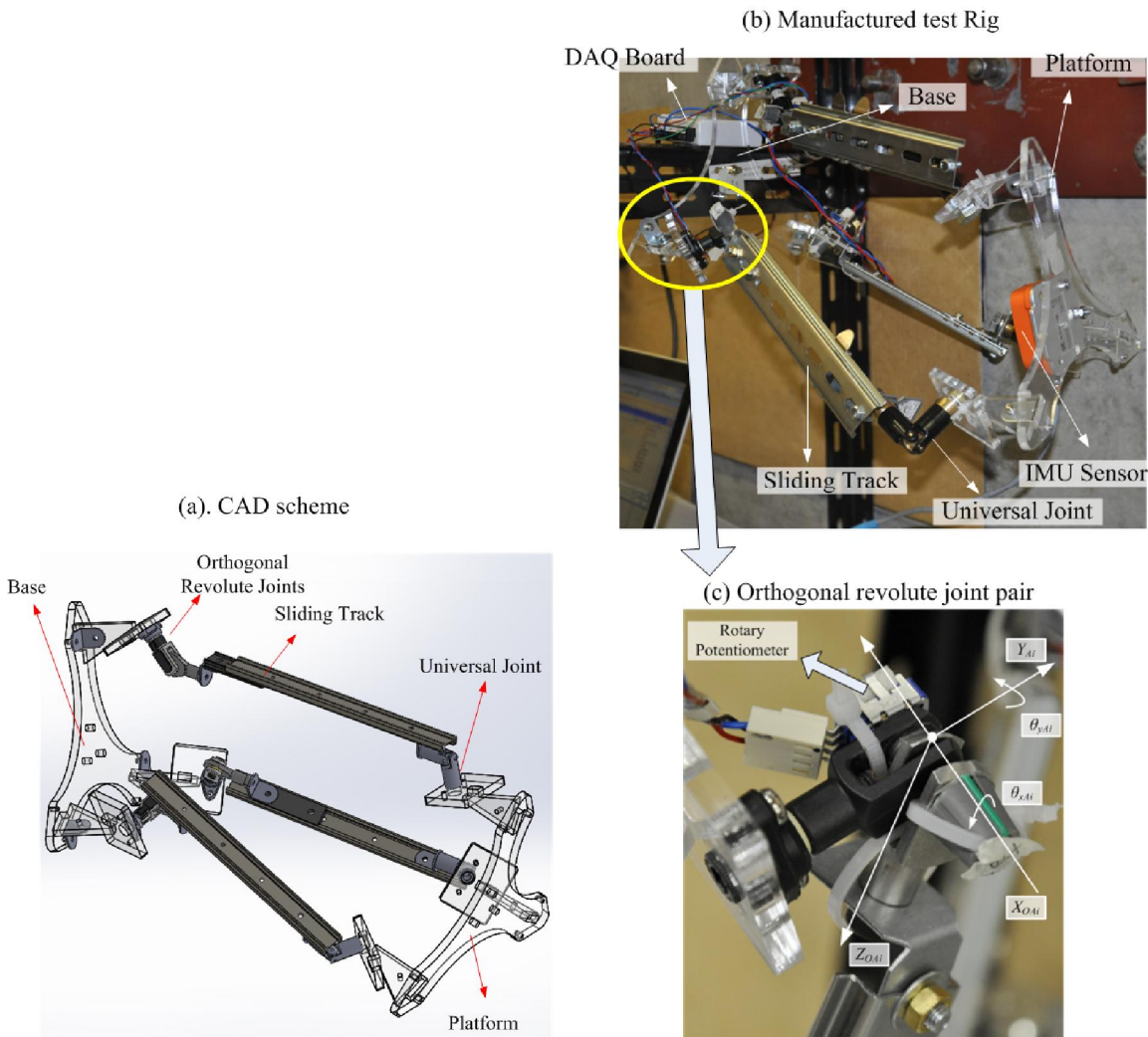


Figure 5-1: Test rig for the *3UPU wrist* mechanism experiment

### 5.1.2 Experiments and Results

#### Static Replication Test and Verification of Inverse Kinematics

The objective of the static replication test is to verify the practicability of the *3UPU wrist* mechanism. The platform of the test rig is placed statically at an arbitrary position, the length of each limb (namely, the distance between two universal joints' centres) can freely change and is manually measured as  $l_{i-measured}$  ( $i = 1, 2, 3$ ), which is compared with the estimated limb length  $l_i$  ( $i = 1, 2, 3$ ) (calculated from the inverse kinematics Equation (4-1) and the rotation angles from the IMU sensor's orientation information). Although inaccuracy in the manual measurement (up to  $5\text{ mm}$  or more) exists because the length we tried to measure is the distance between two virtual

centre points of the corresponding universal joints, the estimated length  $l_i$  should in general be consistent with the measured length,  $l_{i-measured}$ . Any misalignment between  $l_i$  and  $l_{i-measured}$  is attributed to the displacement of rotation centre  $O$ , denoted as vector  $\bar{O}_B$ . According to the pure rotation feature of the *3UPU wrist* mechanism,  $\bar{O}_B$  is ideally zero, and in this experiment  $\bar{O}_B$  is calculated by the following equations:

$$\begin{cases} \bar{O}_B = (O_{ix}, O_{iy}, O_{iz})^T \\ |\bar{O}_B + R(\theta_x, \theta_y, \theta_z)\bar{B}_i - \bar{A}_i|^2 = l_{i-measured}^2 \quad (i = 1, 2, 3) \\ |R(\theta_x, \theta_y, \theta_z)\bar{B}_i - \bar{A}_i|^2 = l_i^2 \end{cases} \quad (5-1)$$

Table 5-1: Test results of static replication test

IMU sensor orientation data (Z-Y-X Euler angles in degrees)			Estimated length $l_i$ (mm)			Manually measured length $l_{i-measured}$ (mm)			Rotation centre displacement $\bar{O}_B$ (mm)	Test cases
$\theta_x$	$\theta_y$	$\theta_z$	L1	L2	L3	L1	L2	L3	(X, Y, Z)	
0.9°	1.0°	-26.2°	278.4	177.4	176.6	275	175	175	(-0.4, -2.3, 2.53)	Case 1
18.5°	-2.3°	9°	277.0	183.9	182.4	275	180	180	(1.8, 1.0, 3.8)	Case 15
32.0°	-11.9°	7.2°	271.9	199.6	184.1	270	202	182	(-6.6, -3.6, -3.5)	Case 9
39.1°	-5.1°	1.6°	268.5	199.5	192.2	270	196	192	(5.8, 5.2, 5.3)	Case 14
39.5°	-3.9°	-3.8°	268.5	198.5	194.1	270	196	193	(0.5, 4.3, 5.2)	Case 13
57.0°	12.4°	-0.8°	256.2	198.0	217.6	270	210	220	(20.9, -13.7, 16.2)	Case 12

The results in Table 5-1 indicate a consistency between the manual measured and estimated lengths in the first five cases (Case 1, Case 15, Case 9, Case 14, Case 13), with the displacement of the rotation centre within  $\pm 7mm$  in all three directions. Several factors are responsible for the rotation centre's displacement. Despite the observational error of the length measurement as well as the data drifting in the IMU sensor, systematic error in the test rig (e.g. the small gap between the orthogonal joint pair and the base) has brought in uncertainties in determining the length of the

limbs as well.

It is noticed that the displacement of the rotational centre has the tendency of increasing as the rotation angle of the platform around axis  $X$  grows. And in the 6<sup>th</sup> case, when  $\theta_x$  reaches  $57.0^\circ$  the displacement of rotation centre rises sharply to around  $20mm$ . This is mainly due to the unsteadiness of the *3UPU wrist* mechanism when approaching singularity. In this case the singular position is the situation where the platform and the base are in parallel, namely when  $\theta_x$  reaches near  $90.0^\circ$  and  $\theta_x$  and  $\theta_y$  are near  $0^\circ$ . According to [106], at the singular position, the limb prismatic joints can extend and contract to an arbitrary length.

In summary, the static replication test reveals the validity of the *3UPU wrist* mechanism's in rotational movement around a fixed space point when the platform is controlled away from its singularity position.

### Verification of the Presented Forward Kinematics

The objective of this test is to evaluate the validity of the proposed alternative forward kinematics approach (Stage Two only). The test is carried out by mainly comparing the calculation results of platform's orientation based on the proposed alternative forward approach (Stage Two) with the measured platform orientation  $(\theta_x, \theta_y, \theta_z)$  from the IMU sensor. The forward kinematics approach uses the three rotation angles  $(\theta_{x_{Ai}}, i = 1, 2, 3)$  in the three orthogonal revolute joint pairs mounted on the base of the *3UPU wrist* mechanism to perform calculation. Angles  $\theta_{x_{Ai}}$  ( $i = 1, 2, 3$ ) are obtained from rotary potentiometers mounted on the orthogonal revolute joint pairs in Figure 5-1(c). It also compares other geometric estimations, obtained in the way of inverse kinematics (calculation based on measured platform orientation  $(\theta_x, \theta_y, \theta_z)$ ) and forward kinematics (calculation based on based on revolute joint's rotation angles  $(\theta_{x_{Ai}}, i = 1, 2, 3)$ ). Calculation results of each limb's length  $(l_i, i = 1, 2, 3)$  and the distance between the platform universal joints and the origin point of the coordinate frame  $(l_i, i = 1, 2, 3)$  are discussed.

We firstly verify the validity of the alternative forward kinematics by comparing vectors  $\bar{B}_i^{\{O_A\}}$  calculated from both the rotary potentiometer and the IMU sensor. Equations (4-1), (4-16), (4-31) and (4-32) are mainly used to obtain  $\bar{B}_i^{\{O_A\}}$ . To review, Equation (5-2) demonstrates the process of

using the IMU sensor data to obtain  $\bar{B}_i^{\{O_A\}}$  and Equation (5-3) demonstrates the way of using  $\theta_{xAi}$  ( $i = 1, 2, 3$ ).

$$\theta_x, \theta_y, \theta_z \Rightarrow \left\{ \bar{B}_i^{\{O_A\}} = R(\theta_x, \theta_y, \theta_z) \bar{B}_i^{\{O_B\}} \right\} \Rightarrow \bar{B}_i^{\{O_A\}} \quad (5-2)$$

$$\left\{ \begin{array}{l} \theta_{xAi} \Rightarrow \left\{ \begin{array}{l} l_i^4 - 2l_i^3 \sin \theta_{xAi} \bar{A}_i \cdot R_{Ai-2} + l_i^2 (2A_i^2 - 2B_i^2 + \sin^2 \theta_{xAi} (\bar{A}_i \cdot R_{Ai-2})^2) \\ - l_i^2 \cos^2 \theta_{xAi} ((\bar{A}_i \cdot R_{Ai-1})^2 + (\bar{A}_i \cdot R_{Ai-3})^2) - 2l_i \sin \theta_{xAi} \bar{A}_i \cdot R_{Ai-2} (A_i^2 - B_i^2) \\ + (A_i^2 - B_i^2)^2 = 0 \end{array} \right\} \Rightarrow l_i \\ \theta_{xAi}, l_i \Rightarrow \left\{ \begin{array}{l} l_i^2 + A_i^2 - B_i^2 + 2l_i \sin \theta_{yAi} \cos \theta_{xAi} \bar{A}_i \cdot R_{Ai-1} \\ + 2l_i \cos \theta_{yAi} \cos \theta_{xAi} \bar{A}_i \cdot R_{Ai-3} - 2l_i \sin \theta_{xAi} \bar{A}_i \cdot R_{Ai-2} = 0 \end{array} \right\} \Rightarrow \theta_{yAi} \\ \theta_{xAi}, \theta_{yAi}, l_i \Rightarrow \left\{ \bar{B}_i^{\{O_A\}} = \bar{l}_i^{\{O_A\}} + \bar{A}_i^{\{O_A\}} = R_{Ai} \cdot R_{OAi}(\theta_{yAi}, \theta_{xAi}) \cdot (0, 0, l_i)^T + \bar{A}_i^{\{O_A\}} \right\} \Rightarrow \bar{B}_i^{\{O_A\}} \\ (i = 1, 2, 3) \end{array} \right. \quad (5-3)$$

Table 5-2 shows the calculation results in both the approach of inverse kinematics and the proposed alternative forward kinematics (Scenario Two) in a static position case. When the test rig is at this static position, the data from both the IMU sensor ( $\theta_{y-measure}$ ,  $\theta_{x-measure}$ ,  $\theta_{z-measure}$ ) and the rotary potentiometers in the test rig ( $\theta_{xAi-measure}$ ,  $i = 1, 2, 3$ ) are recorded. Given the measured platform orientation ( $\theta_{y-measure}$ ,  $\theta_{x-measure}$ ,  $\theta_{z-measure}$ ), inverse kinematics is applied to obtain results ( $\theta_{xAi}$ ,  $\theta_{yAi}$ ,  $L_i$ ,  $B_i$ ,  $i = 1, 2, 3$ ). With the rotation angles of the revolute joints in the orthogonal revolute joint pairs ( $\theta_{xAi-measure}$ ,  $i = 1, 2, 3$ ), the proposed alternative forward kinematics approach (Scenario Two) is applied to obtain the other rotation angles in the revolute joint pairs ( $\theta_{yAi}$ ,  $i = 1, 2, 3$ ), the platform orientation relative to the base ( $\theta_y$ ,  $\theta_x$ ,  $\theta_z$ ) as well as the length of the limbs ( $L_i$ ,  $i = 1, 2, 3$ ) and platform universal joints' distance from the origin point ( $B_i$ ,  $i = 1, 2, 3$ ). Then the calculation results from both the inverse and forward kinematics are compared to verify the validity of the alternative forward kinematics.

Table 5-2 lists the calculation results of the above-mentioned angles and distances. In Table 5-2 the cells with shaded background indicate that the values are practically measured from sensors, and are used as input data for calculation. The comparison of platform's orientation angles ( $\theta_y$ ,  $\theta_x$ ,  $\theta_z$ )

from the rotary potentiometer data show valid estimation results. The estimation of  $(\theta_y, \theta_x, \theta_z)$  based on the rotary potentiometer data from the forward kinematics method, which is  $(\theta_x = 15.55^\circ, \theta_y = -3.0^\circ, \theta_z = 6.5^\circ)$  is close to the measured rotation data from the IMU sensor, which is  $(\theta_x = 18.75^\circ, \theta_y = -2.33^\circ, \theta_z = 8.99^\circ)$ , the difference between the measured angle and estimated angle are  $3.2^\circ, 0.65^\circ$  and  $2.49^\circ$  for  $\theta_x, \theta_y,$  and  $\theta_z$  respectively. The misalignment in length values of  $l_i$  and  $B_i$  between the results of inverse kinematics and the results of forward kinematics are within  $8mm$ . Though the results of length are consistent, the actual vectors are found to be not in the same direction. Furthermore, large misalignment between the estimation from the inverse kinematics and the forward kinematics in  $\theta_{yAi}$  is observed.

Table 5-2: Calculation results of the alternative forward kinematics verification test

<i>Kinematics Approach</i>	<i>Platform Orientation</i> $(\theta_x, \theta_y, \theta_z)$	$\theta_{xA1}, \theta_{xA2}, \theta_{xA3}$	$\theta_{yA1}, \theta_{yA2},$ $\theta_{yA3}$	$L_1, L_2, L_3$ <i>(mm)</i>	$B_1, B_2, B_3$ <i>(mm)</i>
<u>Inverse Kinematics</u>	<u>Measured by IMU</u> $\theta_{x-measure} = 18.8^\circ,$ $\theta_{y-measure} = -2.3^\circ,$ $\theta_{z-measure} = 9.0^\circ$	$-75.4^\circ,$ $-59.4^\circ,$ $43.4^\circ$	$-7.7^\circ,$ $-54.1^\circ,$ $39.7^\circ$	$277.0,$ $184.0,$ $182.6$	$219.2,$ $219.2,$ $219.2$
<u>Forward Kinematics</u> <i>(Stage Two)</i>	$15.6^\circ,$ $-3.0^\circ,$ $6.5^\circ$	<u>Measured by Rotary pot</u> $\theta_{xA1-measure} = -83.6^\circ,$ $\theta_{xA2-measure} = 31.1^\circ,$ $\theta_{xA3-measure} = 34.4^\circ$	$-4.62^\circ,$ $-59.4^\circ,$ $43.4^\circ$	$271.4833,$ $182.4,$ $180.5,$	$211.7,$ $217.6,$ $219.7$

This misalignment is mainly attributed to insufficiency of the hardware, this includes that the stroke of the rotary potentiometer is assumed to be  $300^\circ$ , while the actual stroke varies from  $295^\circ$  to  $305^\circ$  [107], which can results an error around  $1.7\%$ , as well as the error in the installation and calibration of the rotary potentiometer. Better revolute pairs and test rig should be built.

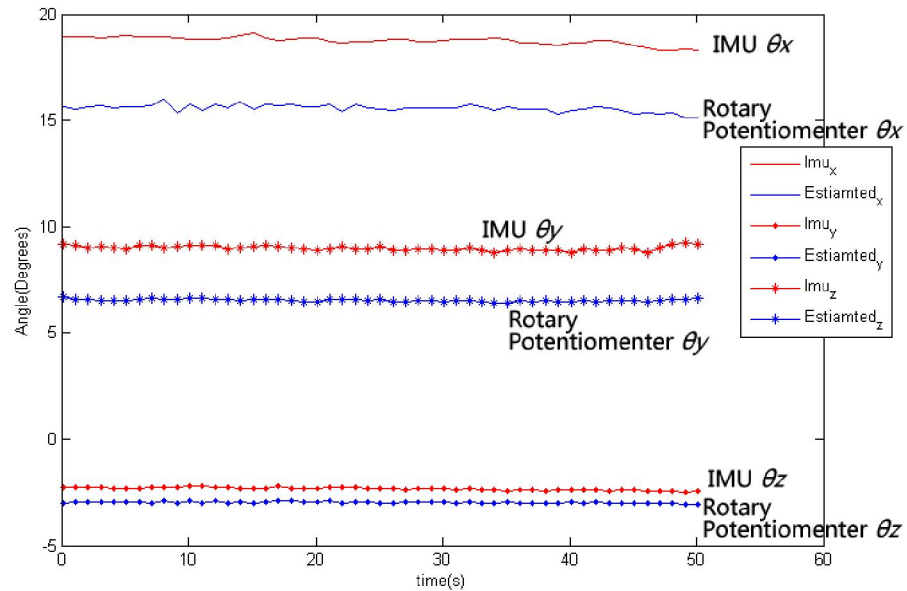


Figure 5-2: Calculated results of platform orientation and the measured orientation (IMU  $\theta_x$ , IMU  $\theta_y$ , IMU  $\theta_z$ ) in the alternative forward kinematics verification test

For the computation of time consumption, each loop of calculation would take up to *0.1 seconds*. Figure 5-2 shows a sample of the real time feedback for calculating platform rotation angles ( $\theta_x$ ,  $\theta_y$ ,  $\theta_z$ ), in comparison with the acquired IMU sensor's data. The estimation error is between  $2^\circ$  to  $4^\circ$ , which is acceptable under such circumstance. Since the computation speed is not satisfactory, we didn't carry on doing further dynamically moving experiments, which will be studied in future work. Despite this, the test results still indicate a valid and potential alternative forward kinematics approach, given proper inputs.

## 5.2 The Shoulder Assistive Exoskeleton Prototype

### 5.2.1 Overall System

A prototype shoulder assistive exoskeleton was built to test the developed PMA model and the kinematics of the “3UPU wrist” mechanism. Figure 5-3 shows the prototype. A wooden dummy is modified on its shoulder joint to replicate the 3D rotation around a fixed centre. The 3UPU wrist mechanism was realised in a straightforward and easy built design. When manufacturing and mounting the exoskeleton, special procedures, according to the geometric requirements [101], were

followed in order to make the exoskeleton produce only rotation motion. A compressed air transmission system was designed on a board unit at the back of the dummy. Compressed air passes through a main pressure regulator, and a manifold with four branches. Each branch contains an individual three way two port solenoid valves, and restriction valves. Five analog pressure signals from the pressure transducers in the main tube and branches are transmitted to the National Instrument data acquisition (DAQ) board, which communicates with the laptop through a USB connection. The IMU orientation sensor mounted on the dummy arm provides real time orientation information. The control program generates a series of digital pulse signals as a pulse-width modulation (PWM) signal to the DAQ board and through a voltage amplifier to control the solenoid valves' on and off state. The amplifier essentially consists of a solid state relay and  $24V$  DC power. The relay's working frequency is over  $1000\text{ Hz}$ , which is sufficient to cope with the operating frequency of PWM signals, which is  $20\text{ Hz}$ . An IMU sensor (© Xsens Technologies B.V., Model: Mti-G) is used to capture the upper arm's orientation. It is capable of obtaining the rotational acceleration, velocity and orientation referenced to the earth's magnetic field. With calculation time accounted for, the sampling frequency for orientation data output is  $256\text{ Hz}$  and the drift is acceptable ( $1^\circ - 2^\circ$  for half a minute), making it sufficient for our research. Four differential pressure sensors (Freescale™ MPX5700DP) are adopted to record the pressure of the regulated air source and pressure in each PMA respectively.

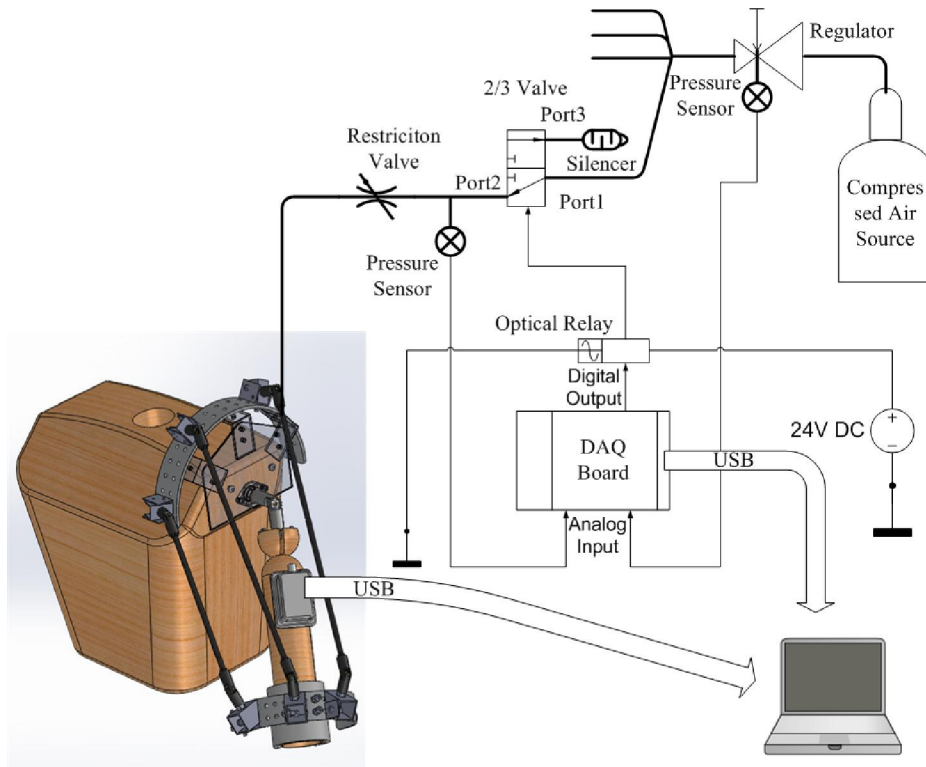


Figure 5-3: Overall scheme of the Prototype

### 5.2.2 Dummy

A wooden dummy torso, shoulder and arm are used to emulate the 3D rotation of a human shoulder joint. To reach the essential goal of replicating the 3D rotational movement around a fixed rotation centre, we customised a special 3D rotation unit as the shoulder joint. As illustrated in Figure 5-4, it essentially consists of a bearing flange and a universal joint. The outer ring of the bearing flange is mounted onto the dummy torso. A bolt goes through the inner ring, attached to it by a nut. The end of the bolt is securely connected to one end of a universal joint. The other end of the universal joint is securely connected to the upper arm of the dummy. In this way, the inner ring is connected to a universal joint, and the whole unit is capable of rotating in three orientations. Around the  $Y$  axis of this unit (coordinate frame in Figure 5-4), the rotation range is unlimited. The rotation angles around the  $X$  and  $Z$  axes are restricted by the universal joints. Generally, the manufacturer claims  $20^\circ$  working range in both directions [108], although the actual angle range varies according to the other angle's value.

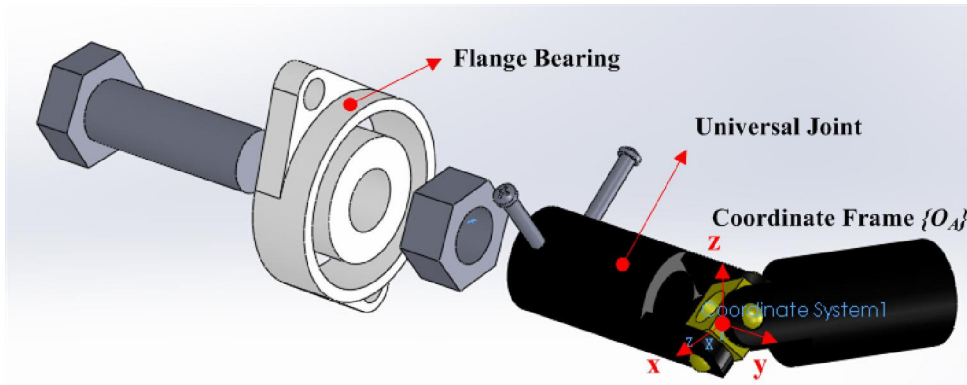


Figure 5-4: Structure of the 3D rotational unit emulating shoulder joint

### 5.2.3 Exoskeleton

#### Geometry

The optimal geometry obtained in Appendix C was not practically realised due to manufacturing restrictions. Specifically, since the universal joints are designed to be mounted in pairs of holes spaced in equal increments of  $10^\circ$ , variables  $\alpha_{1A} = 36.7^\circ$ ,  $\alpha_{2A} = 56.8^\circ$  and  $\alpha_{3A} = 115.2^\circ$  are rounded to match the nearest pair of holes. However, for  $\alpha_{1A}$ , which should be rounded into  $40^\circ$  due to mechanical interference, we have to mount it further away from the second universal unit, at the position determined by  $\alpha_{2A}$  ( $59.6^\circ$ ). The other major difference between the optimised geometry and the prototype geometry is the size of the platform plane and the base plane. Since the variable boundaries for  $(r_A, r_B, h_A, h_B)$  in the workspace optimization was based on human's anthropometric surveys, applying them to the wooden dummy prototype is rather difficult. Therefore we disregarded the optimisation results for variables and adapted them to meet the geometric conditions for the exoskeleton to work as a  $3UPU$  wrist mechanism. The way of determining  $(r_A, r_B)$  is presented later in the section. Although the optimal geometry is not carried out, the exoskeleton is still made adjustable on some variables (variables  $\alpha_{1A}$ ,  $\alpha_{2A}$  and  $\alpha_{3A}$ ). As the structure illustration of the platform and the base in Figure 5-5(a) shows, there are equally distributed pairs of holes designed on the platform plate and the base plate, which makes  $(\alpha_{1A}, \alpha_{2A}, \alpha_{3A})$  adjustable in increments of  $10^\circ$ . Table 5-3 lists the geometric variables of the CAD design and prototype.

Table 5-3: Geometry of prototype exoskeleton

Geometric Variables	$r_A$	$r_B$	$h_A$	$h_B$	$\alpha_{1A}$	$\alpha_{2A}$	$\alpha_{3A}$
Prototype Geometry	136.30 mm	118.8 mm	78 mm	200 mm	31.3°	59.6°	119.8°
Optimised Geometry	81.8 mm	95.3 mm	99.9 mm	181.8 mm	36.7°	56.8°	115.2°

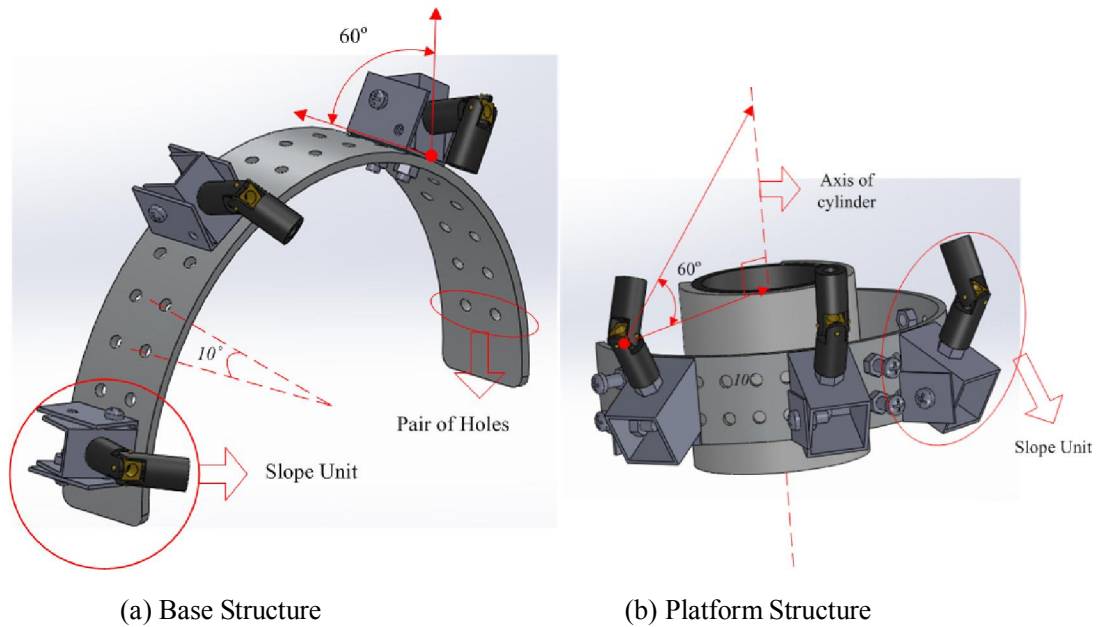


Figure 5-5: Structure of the exoskeleton

Figure 5-6 is a photo of the prototype. The pneumatic and electric control units are not shown in this picture. On the bottom right of this photo, the fourth universal joints and the PMA are shown, but it is not used in current experiments. It can be used for further studies.

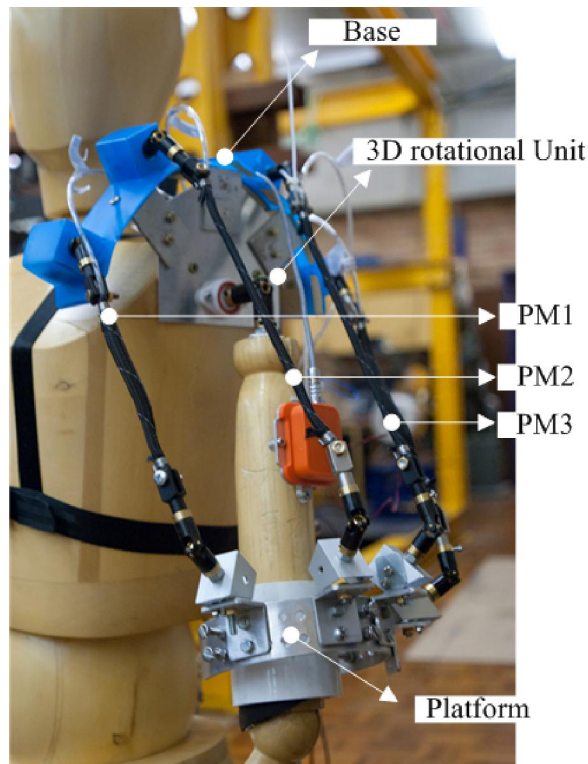


Figure 5-6: Photo of the prototype

### Assembling

As was stated by Gregorio in [101], two geometric conditions need to be met in order that the *3UPU* wrist mechanism performs 3D orientation around one rotation centre. In the practical prototype, the geometric conditions should be guaranteed in the both manufacturing and assembling process. In addition, in the assembling process we need to make sure that the *3UPU* wrist mechanism aligns with the shoulder rotation centre.

The first geometric condition is that each of the six revolute pairs must have one joint axis intersecting with the axes from other revolute pairs at a common fixed point in space. To meet such a requirement, we need to adjust the distance of the platform and the base relative to the shoulder rotation centre. In terms of manufacturing, as Figure 5-5(a) and Figure 5-5(b) illustrate, the slopes for mounting all the universal joints on both the base and the platform are customized to be at an angle of  $60^\circ$ . The value of  $60^\circ$  is a compromise between sufficient space on the sides to drill holes and bolt, convenience in calculation as well as mechanical interference of the prototype. According to the geometric relationship illustrated in Figure 5-8(b),  $r_A / h_A = \tan 60^\circ$  and  $h_B / r_B = \tan 60^\circ$ . Given

the distance from the base plane and the platform plane to the rotation centre  $O$  as  $h_A = 78 \text{ mm}$ ,  $h_B = 200 \text{ mm}$ ), we can calculate the size of the base and the platform as  $r_A = 136.30 \text{ mm}$ ,  $r_B = 118.8 \text{ mm}$ .

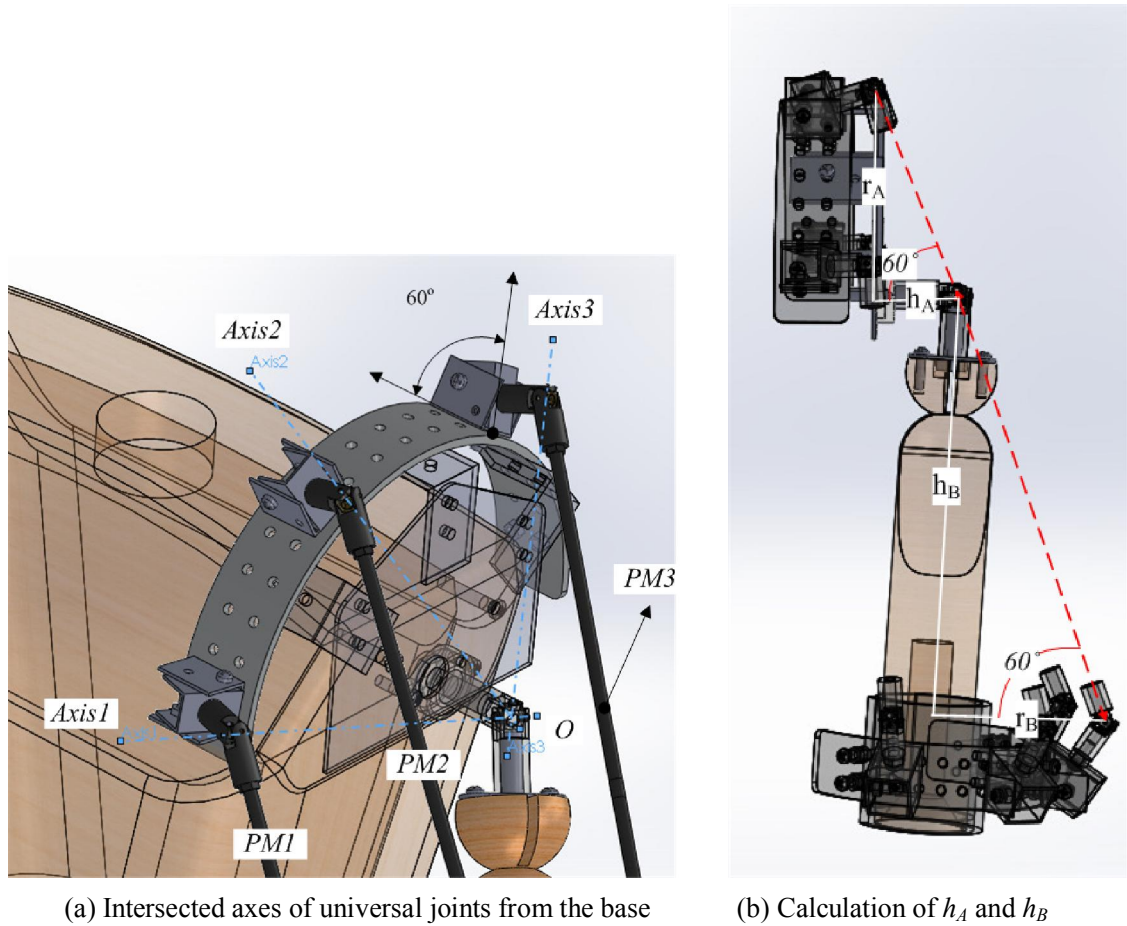


Figure 5-7: Assembly meeting the geometric requirements of the “3UPU wrist” mechanism

The second condition is that, the other revolute axis in the universal joint should be in parallel with the corresponding revolute axis on the other end of the limb or pneumatic muscle. This condition is satisfied by aligning the universal joint of the platform and base in the same angled pair of holes, in other words,  $\alpha_{iA} = \alpha_{iB}$  ( $i=1,2,3$ ).

Table 5-4 shows the mass and inertia information of the moving part in the design as well as the measured weight of the actual prototype’s moving part. The inertia matrix is computed in the coordinate frame relative to the moving platform  $\{O_B\}$ . The centroid position is also presented in the coordinate frame attached to the moving coordinate frame  $\{O_B\}$ .

Table 5-4: Mass and moment of inertia of the platform of the prototype

Mass(g)	Centroid (mm)	Moment of Inertia (gmm <sup>2</sup> )
656.56	(-2.60,22.7, -189.7)	(27867611.9    -21184.2    319504.5
	distance to rotation	-21184.2    27638169.9    -2649709.2
	centre: 191.07mm	319504.5    -2649709.3    1419768.2)

### 5.3 Control

In this section we discuss the position control of the prototype to accomplish ADL tasks and the *PI* controller developed for the PMAs. The position control scheme is illustrated in Figure 5-8.

The PMA contraction rate is computed in advance from the desired trajectory of the shoulder joint angles ( $\theta_{x\_d}, \theta_{y\_d}, \theta_{z\_d}$ ) and then passed to the PI control as reference values. The program acquires the actual orientation from the IMU sensor at the sampling frequency of 100Hz and then calculates the length contraction rate through the orientation calibration ( $\theta_x, \theta_y, \theta_z$ ) and the inverse kinematics ( $L_i$ ). The error in contraction rate for each PMA is conveyed into the PI controller. The output of the PI controller is transmitted to the PWM generator, which generates a pulse signal according to the given duty cycle, to control the on and off of the solenoid valves.

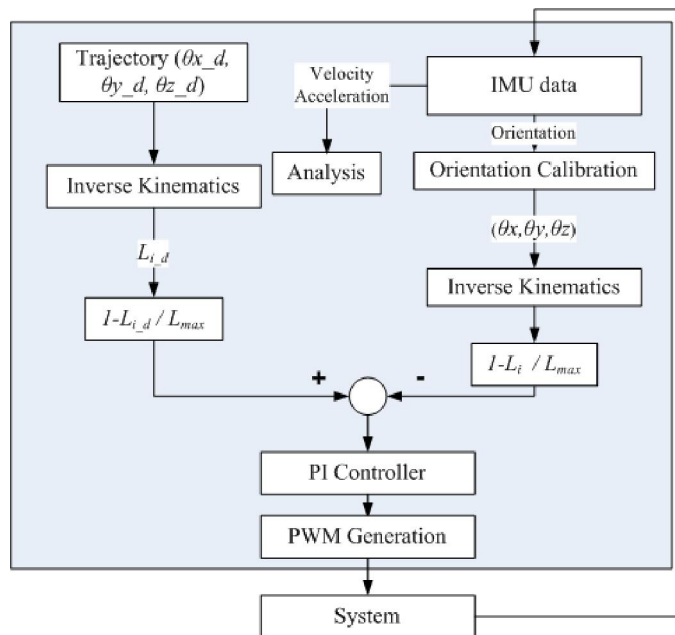


Figure 5-8: Position control scheme of the prototype

A couple of blocks in Figure 5-8 are briefly introduced in the rest of this section.

The orientation calibration block is illustrated in Figure 5-9. The outputted rotation matrix from the IMU sensor  $R_{GS}$  represents its orientation relative to the ground. With calibrated torso rotation matrix  $R_{GT}$ , and coordinate transformation matrix  $R_{SS'}$ , we can obtain the rotation matrix  $R_{TS'}$ , containing shoulder rotation angles  $(\theta_x, \theta_y, \theta_z)$  as described in Figure 5-9(b).

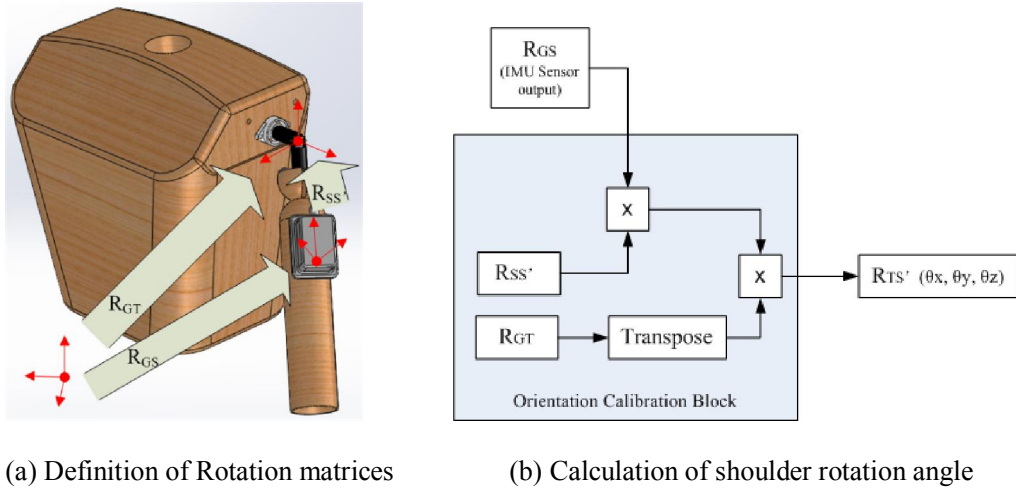


Figure 5-9: Orientation Calibration Block

Proportional-integral (PI) controllers are developed for the PMAs. As stated in [92], the PI control approach for pneumatic actuated systems has advantages in reducing design complexity and provides comparatively good performance in reducing error. Hence it is applied in a single PMA's position control. We tested the PI controller in the experiments illustrated in Figure 5-10.

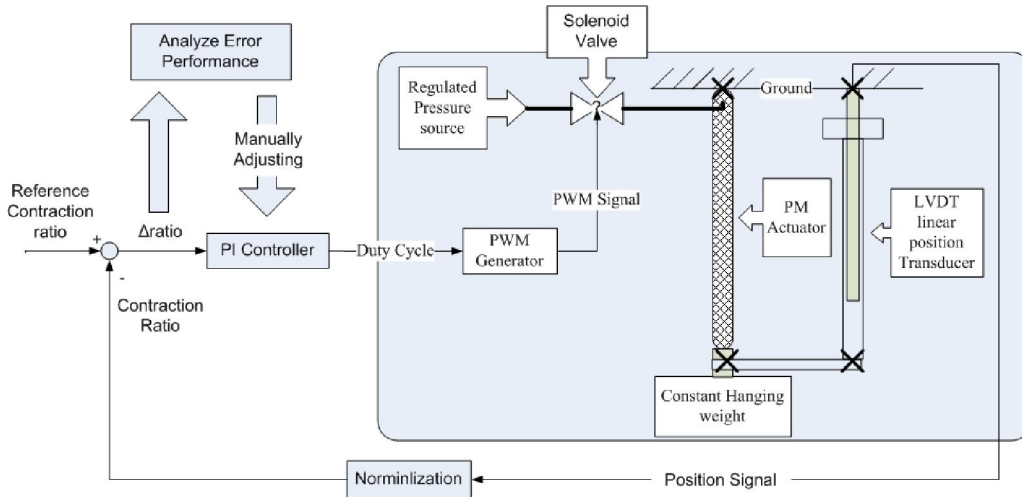


Figure 5-10: Schematic diagram for the PMA PI controller test

Table 5-5 shows the coefficients used for control of the PMAs in the prototype. Slightly different coefficients for two types of PMAs are obtained. The steady state error of the PI controller achieved is within 5%. With valve restrictors before the inlet of the PMAs, there is not overshoot in the response. Occasionally, displacement jittering occurs because of time lapse. This can be solved by implementing hardware generated PMW signals in the valve control.

Table 5-5: PID Coefficients of PMAs

<i>Muscle</i>	$K_c$	$T_i$	$T_d$
<i>PMA1 (Φ6-150)</i>	$2.3 \times 10^{-2}$	$6.62 \times 10^{-1}$	0
<i>PMA2 / PMA3 (Φ6-250)</i>	$3.3 \times 10^{-2}$	$9.5 \times 10^{-1}$	0

## 5.4 Position Tracking Experiment

After the prototype and controlling scheme were developed, several experiments were conducted to test the capabilities of the 3UPU wrist based prototype. The prototype’s capabilities in the 3D rotation capability as well as its kinematic capability in realising ADL tasks are studied.

### 5.4.1 Preliminary Tests on 3D Rotation Capability

Two preliminary experiments were carried out to test the feasibility of the prototype. In the preliminary tests the prototype system is programmed to conduct two basic movements in the

shoulder joint: abduction (around axis  $X$  in the coordinates in Figure 5-5) and flexion (Around axis  $Y$  in Figure 5-5). The reason we neglect internal/ external rotation (Around axis  $Z$  in Figure 5-5) at the rest position is, because the structure of the dummy's shoulder joint has restricted the upper arm to move freely in this direction at the rest position.

### Abduction Experiment

In the first outwards abduction experiment, rotation angles around  $Y$  and  $Z$  are commanded to remain zero ( $\theta_{y\_des}=0$ ,  $\theta_{z\_des}=0$ ), and  $\theta_{x\_des}$  is commanded to move from  $0^\circ$  to  $90^\circ$  in  $5s$  in constant speed. The desired starting posture and desired ending posture of this motion is illustrated in Figure 5-11(a), while the experimental angle data is displayed in Figure 5-11(b).

In the experimental results, we first observed that both the desired starting and ending positions are not achieved. For the unpressured starting position, though desired to start from posture of ( $\theta_{x\_des} = 0^\circ$ ,  $\theta_{y\_des}=0^\circ$ ,  $\theta_{z\_des}=0^\circ$ ), the prototype actually starts from the posture of ( $\theta_{x\_des} = 8.8^\circ$ ,  $\theta_{y\_des} = -13.4^\circ$ ,  $\theta_{z\_des} = -8.8^\circ$ ). The inextensibility of PMAs is mainly responsible for this misalignment. In other words, the  $\Phi 6-150$  ( $150mm$  long) PMA could not be stretched further longer than  $150mm$  to rest the prototype at desired starting position. In this test due to applied weight, the stretching length at starting position is stretched to around  $160mm$ .

To analyse the impact of inextensibility and stroke limitation of the PMA in this task, in Figure 5-12 the calculated PMA length, namely the distance between the  $i$ th base universal joint and the  $i$ th platform universal joints (both desired length  $l_{i\_des}$  and actual length  $l_i$ ) are presented. The calculation is based on inverse kinematics of Equation (4-1). In this figure, PMA2 and PMA3 show valid tracking results in contraction along with desired trajectory before  $3.5s$  of the response time. And for PMA1, during most of the task time, the desired PMA length  $l_{1\_des}$  is larger than the actual length PMA1 can be stretched to. In fact, before the  $4^{th}$  second, the desired PMA length ( $l_{i\_des}$ ,  $i = 1, 2, 3$ ) is always larger than  $150mm$ , which is the normal length of PMA1 actuator  $\Phi 6-150$ . Therefore before the  $4^{th}$  second, PMA1 is incapable of achieving desired length.

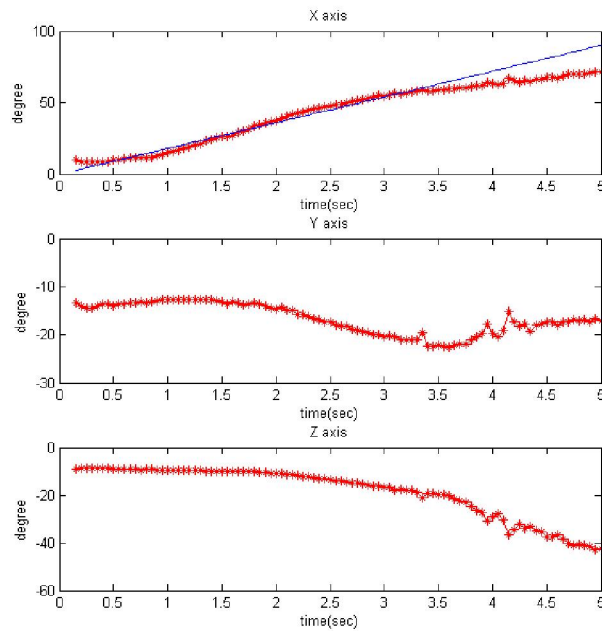
At  $3.5s$ , on the one hand, PMA2 reaches its maximum contraction length position, i.e. minimum actuator active length (around  $170mm$  for the  $\Phi 6-250mm$  PMA) and thus the contraction force in PMA2 becomes zero. On the other hand, PMA3 still tries to decrease the error between the desired

length  $l_{3\_des}$  and the actual length  $l_3$ , so that it performs further contraction until at 5s where PMA3 contracts to the length of 171.9mm, which close to its maximum contraction length position (around 170mm for the  $\Phi 6-250mm$  PMA). During the period of 3.5s and 5s, although PMA2 has reached its minimum length of 170mm, due to the contraction force of PMA3, the distance of  $l_i$  continues to be shortened and PMA2 is bent to a curve so that the distance is shortened to 155.5mm. Overall, the desired length at the end position (130mm for PMA2 and 120mm for PMA3) is beyond the PMA's stroke capability.

The resultant angle tracking experimental results in Figure 5-11 indicate that, the around X axis, the angle tracking has been successful at the beginning, until the increasing speed of the angle falls at the time around 3.5s (angle around 60°), and then it slowly grows until it reaches 75° at the end of the experiment. The angle did not reach the desired destination of 90°. The desired angle of 0° around the Y and Z axis is always beyond the exoskeleton's workspace, mainly due to the inextensibility of the PMAs and the PMA's stroke limitation.



(a) Motion illustration



(b) experimental rotation angle

Figure 5-11: Rotation angle in Abduction Experiment

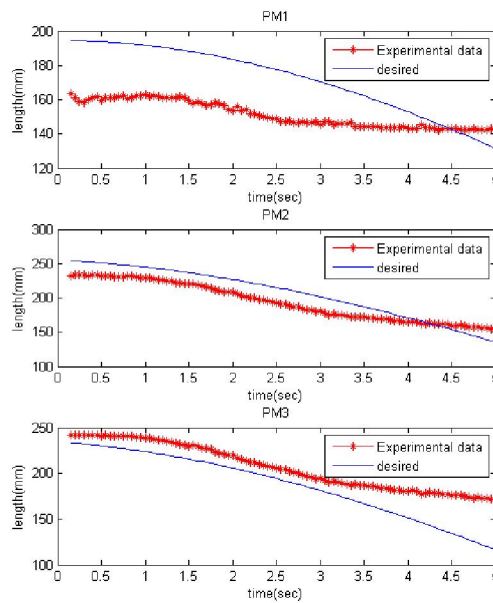


Figure 5-12: PMA length trajectory of abduction experiment

This experiment shows reasonable length tracking capability in PMA2 and PMA3, as well as acceptable abduction capability of the prototype. The prototype is able to achieve an angle of  $75^\circ$  in the abduction test. If the desired position is within the range of the PMAs, the prototype is able to reach it. For larger a range of motion, longer PMAs are needed.

### Flexion Experiment

The second experiment is forward flexion. We command the desired rotation angles around  $X$  and  $Z$  axes is maintained at zero ( $\theta_{x\_des}=0$ ,  $\theta_{z\_des}=0$ ), and  $\theta_{y\_des}$  is commanded to move from  $0^\circ$  to  $-90^\circ$  in 5s in constant velocity. Figure 5-13(a) illustrates the starting and ending position of the motion.

The desired and experimental rotation angles are displayed in Figure 5-13b. Misalignment between the desired trajectory and the actual response still exists in this test.

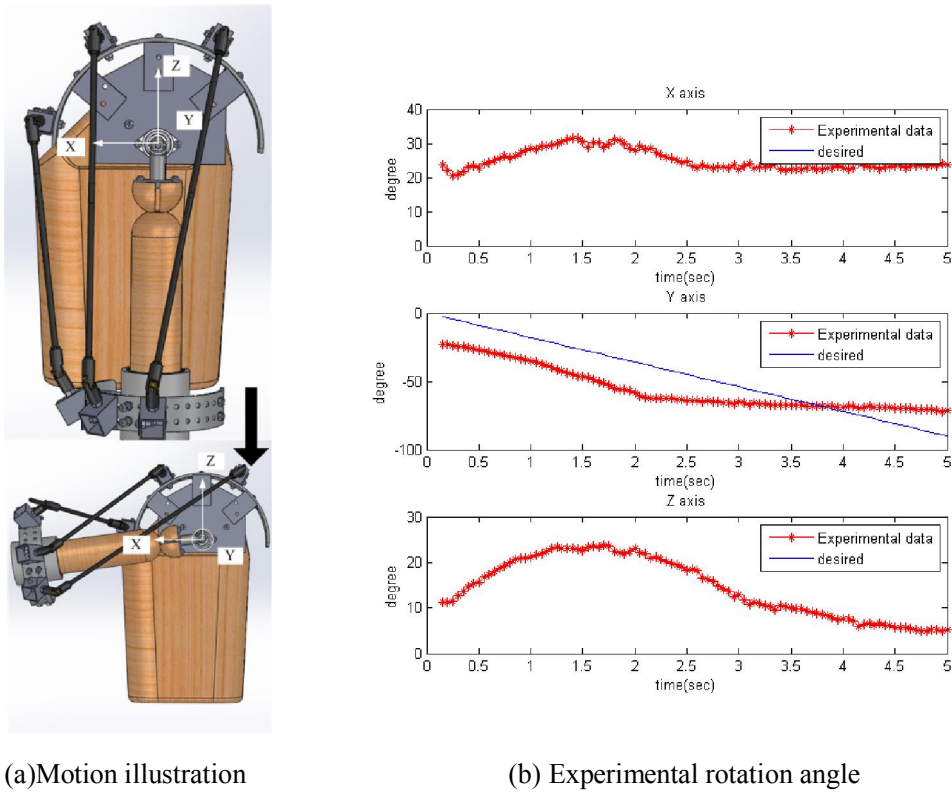


Figure 5-13: Rotation angle in flexion experiment

If we first discuss the PMAs' desired and actual length responses plotted in Figure 5-14, it is found that the desired length trajectory ( $l_{1\_des}$ ) of PMA1 is rather demanding, which requires the actuator to contract from 200mm to 50mm. While in the actual length response ( $l_1$ ) the PMA contracted from its normal length of around 160mm (pre-tensioned) to around 110mm, accomplishing nearly a full 26.7% contraction rate for a  $\Phi 6-250mm$  PMA. The length response of PMA2 ( $l_2$ ) achieved close to the desired length tracking result during the first 3s of the trajectory, after 3s, PMA2 reached its maximum contraction and becomes a stiff spring bent by other actuators (PMA1). The desired length of PMA3 is close to its nominal length, therefore, during most of the test, PMA3 is not properly pressurized and  $l_3$  show a loosely unpredictable response. Overall, we can conclude that demanding the desired trajectory of PMA1 is not accomplished and this has for the most part hindered the prototype from acting more flexion.

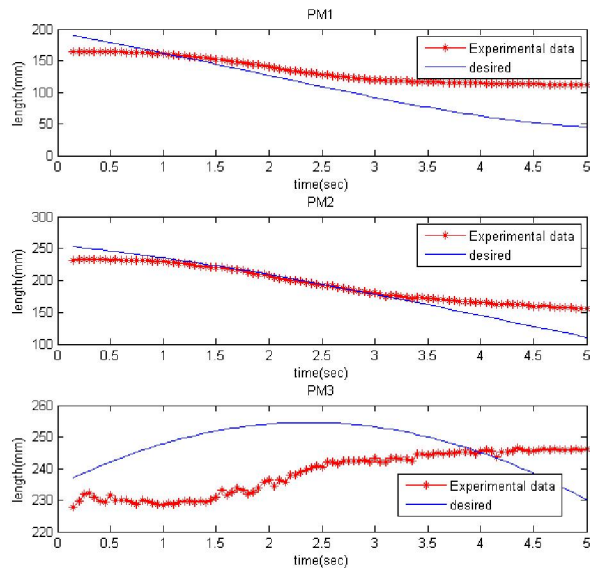


Figure 5-14: PMA length trajectory of flexion experiment

The resultant angle results in Figure 5-13(b) are even more unexpected and difficult to estimate due to the underperformance of PMA1. Generally, the  $X$  and  $Z$  axes are still not maintained at  $0^\circ$ . Around the  $Y$  axis, the prototype rotates from  $-20^\circ$  to  $-70^\circ$  and then remains at  $-70^\circ$  for the last 3 s of the whole experiment.

The preliminary tests showed that the single PMA's control is acceptable, and 3D rotation of the prototype can reach positions that are within the range of the PMAs' contraction. It also demonstrated that the prototype design is acceptable. We also discovered the limitation of the PMA's stroke which limits the prototype's range of motion. In order to have a larger range of motion, different PMAs need to be used and a different way to mount the actuators must be used as well.

#### 5.4.2 ADL task test

In this section, we are going to study and improve the prototype's performance in accomplishing upper limb ADL tasks. We selected tasks from a survey of human upper limb's ADL tasks in [109] because Santos et al. have provided full trajectory data in their paper, rather than simple ranges of angles in their research. By implementing the trajectory data in the prototype system, the process of achieving the ADL task can be examined. There are in total four tasks studied in [109] -- "Hand to

contra lateral shoulder”, “Hand to mouth”, “Combing hair” and “Hand to back pocket”.

In [109] the authors used a different Euler sequence to model the shoulder joint, which is arranged as “Elevation Plane - Elevation – Internal/ External Rotation” (Figure 5-15(a)). Thus transformation is applied on each task’s original trajectory angles to obtain the corresponding angle trajectories in our model, which is in the sequence of “Flexion, Abduction and Axial rotation” (“Y-X-Z”), as illustrated in Figure 5-15(b),

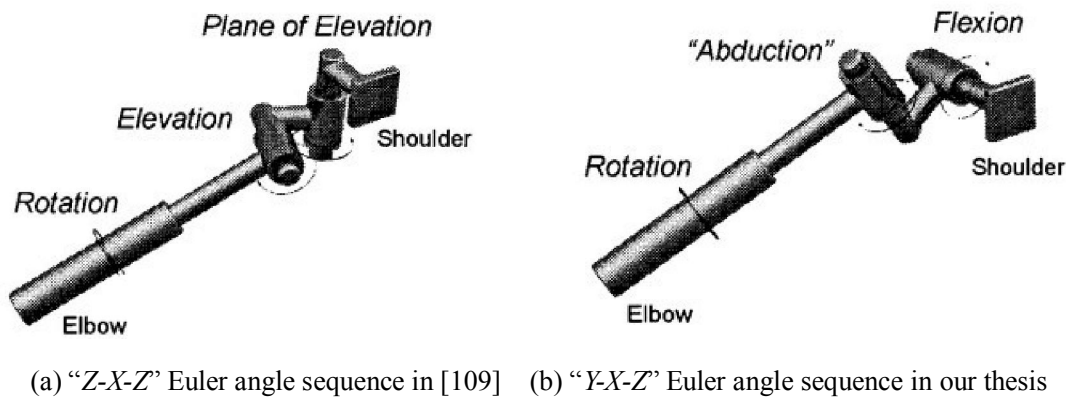


Figure 5-15: Conversion of kinematic model for the prototype [32]

### 1. Workspace mapping and task selection

In order to select a task from the four tasks for implementation in the prototype system, we simulated the reachable workspace of the developed prototype and verified whether a task’s trajectory postures fall in the prototype’s reachable workspace. By doing this, we can find the task with the largest proportion of trajectory postures within the prototype workspace.

The difference between the prototype workspace and the *3UPU* wrist workspace (simulation in Appendix C ) is mainly caused by the restriction of the angles of the “*3UPU* wrist” mechanism in the prototype and the stroke limitation of the PMAs. The customised 3D rotational unit (illustrated in Figure 5-4 ), which is working as a human shoulder joint, also affects the prototype workspace. Table 5-6 lists the conditions we used to determine whether a posture is in the reachable workspace of the prototype.

Table 5-6: Reachable position condition in the prototype workspace

<i>“3UPU Wrist” Mechanism</i>	$-95^\circ < \theta_{yAi} (\theta_{yBi}) < 95^\circ$ $ 190^\circ - \theta_{yAi}  - 90^\circ < \theta_{xAi} (\theta_{xBi}) < 90^\circ -  190^\circ - \theta_{yAi} $
<i>3D rotational unit (Shoulder joint)</i>	$-5^\circ < \theta_x < 185^\circ$ $ \theta_x - 90^\circ  - 95^\circ < \theta_z < - \theta_x - 90^\circ  + 95^\circ$
<i>Pneumatic Muscle Actuator</i>	$75\% L_{i\_max} < L_i < L_{i\_max} (L_{1\_max} = 150\text{mm}, L_{2\_max}, L_{3\_max} = 250)$

In Table 5-6, the second row shows the workspace of the 3D rotational unit in the prototype. The restriction is essentially attributed to the constraint of a universal joint used in this unit. Around  $Y$  axis (refer to Figure 5-4 for axis definition), where the flange bearing is adopted to allow rotation, there is no angle limitation. The restriction pattern for universal joint angles (characterised in Table 5-6) applies to rotation angles around the  $X$  and  $Z$  axes because a similar universal joint is used.

Then, given a certain posture  $(\theta_x, \theta_y, \theta_z)$  and determined geometric variables  $(r_A, r_B, h_A, h_B, r_A, r_A, r_A, \alpha_{1A}, \alpha_{2A}, \alpha_{3A})$  listed in Figure 4-1, we could compute the corresponding  $(L_i, \theta_{yAi}, \theta_{yBi}, \theta_{xAi}, \theta_{xBi})$  and check if the variables  $(\theta_x, \theta_y, \theta_z, L_i, \theta_{yAi}, \theta_{yBi}, \theta_{xAi}, \theta_{xBi})$  fall into the range defined by Table 5-6.

The trajectory of tasks in [109] are expressed as 100 discrete postures in a normalised time scale of 0% to 100%. Each posture is verified by the conditions in Table 5-6. The program outputs a status value: value “1” denotes the posture within the prototype workspace and value 0 denotes the contrary. The status results are presented in Figure 5-16, and Table 5-6 shows the percentage of postures inside the prototype workspace.

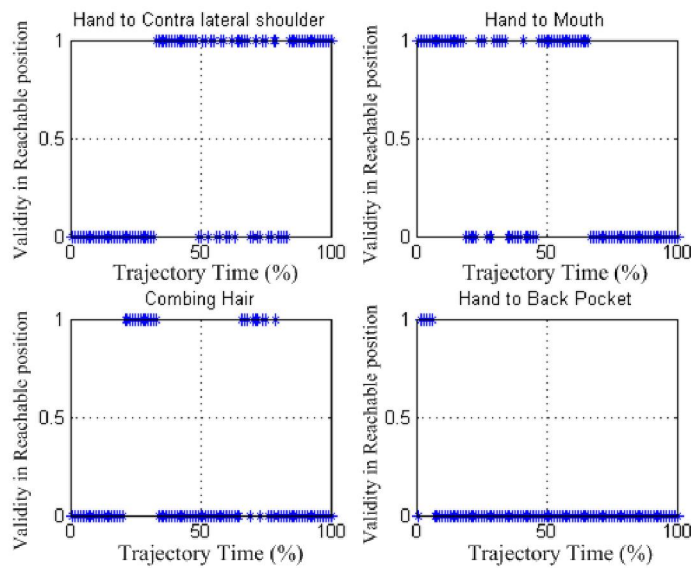


Figure 5-16: The status value of each task in the prototype workspace

Table 5-7: Workspace verification result of four tasks

Task Name	Hand to contra lateral shoulder	Hand to mouth	Combing hair	Hand to back pocket
Proportion of trajectory postures within prototype workspace	51%	47%	22%	5%

Due to the limitation of the prototype workspace, only part of the postures of each task is within the prototype workspace. “Hand to back pocket” is the worst one with only 5% postures attainable, i.e. only few positions at the start of the task motion can be achieved. It can be explained by the fact that, there are no actuators mounted at the back side of the exoskeleton to drive the upper arm movement backwards. “Hand to contra lateral shoulder” and “Hand to mouth” tasks have similar proportion of trajectories within the prototype workspace, which are 51% and 47% respectively. The reachable postures of the “Hand to mouth” task are in the beginning part of the trajectory while the postures of the “Hand to contra lateral shoulder” task at the ending part are more reachable.

In order to perform a test with a successful start, we decided to use the entire trajectory of “Hand to mouth” tasks in the ADL workspace test. Although as Figure 5-16 shows, in the task of “Hand to Mouth”, after the initial 25% time, positions in the desired trajectory are not always in reachable

workspace anymore, it is still meaningful to observe how the PMAs act in approaching the desired trajectory and its capability in lifting (as lifting is involved in lots of tasks in ADL). The angles in the trajectory of “Hand to mouth” are input into the controller program as reference signals in the prototype position controller scheme (Figure 5-5).

## 2. Experiments

Figure 5-17 shows the response of the actuator’s contraction ratio in the tracking test. The contraction ratio is obtained by dividing each PMA’s contraction length by its normal length  $l_{0-PMi}$ , ( $i=1, 2, 3$ ).

$$\left\{ \begin{array}{l} Ratio_{PM1}(t) = \frac{l_{0-PM1} - l_1(t)}{l_{0-PM1}} = \frac{150 - l_1(t)}{150} \\ Ratio_{PM2}(t) = \frac{l_{0-PM2} - l_2(t)}{l_{0-PM2}} = \frac{250 - l_2(t)}{250} \\ Ratio_{PM3}(t) = \frac{l_{0-PM3} - l_3(t)}{l_{0-PM3}} = \frac{250 - l_3(t)}{250} \end{array} \right. \quad (5-4)$$

Both the desired trajectory and the experimental trajectory data are displayed in the three plots. Each PMA’s position tracking performance is discussed and finally the resultant motion in this tracking experiment is presented. For PMA1, generally valid consistent tracking results are obtained throughout the trajectory. The experimental response of PMA1’s contraction ratio rises from about 8% (desired end position is 6%) to desired 33% (desired end position is 35%) in the desired way. Two slight overshoots in the first 20 s of the tracking response is observed. It is probably caused by the non-smooth on and off air flow brought about by the solenoid valves. This problem should be solved by adopting smaller flow rate valves. For PMA2 and PMA3, the first 15s of the contraction ratio response climbs in the desired way and are close to the desired contraction ratio trajectory. After 15 s, the contraction ratio of PMA2 and PMA3 become steady (18% and 8.5%) and fails to rise to the desired end position (33.2% and 17.9%).

The performance of the PMA’s tracking results is in accordance with the task’s trajectory simulation results in Figure 5-17. This simulation result indicates that about the first 25% of trajectory positions are continuously within the prototype’s reachable range. And the rest of the trajectory positions are either beyond the workspace or isolated by unreachable positions.

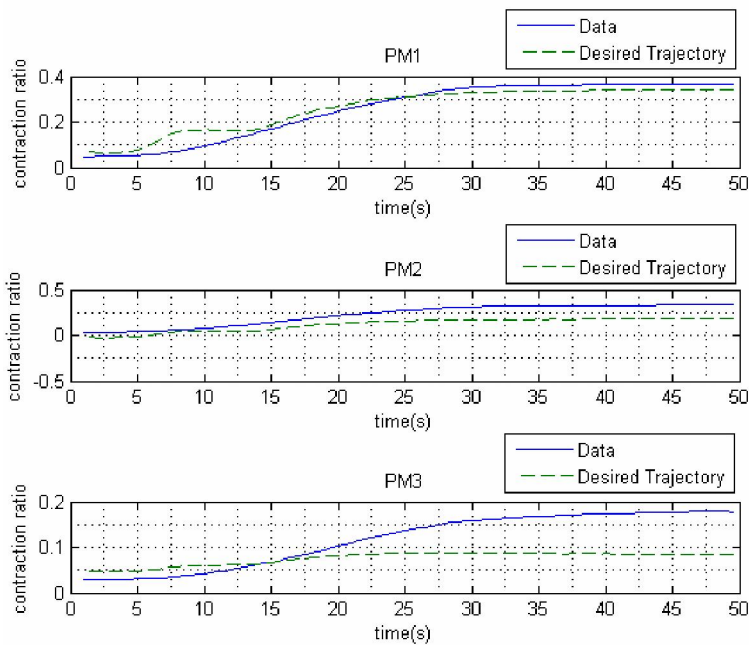


Figure 5-17: Actuator contraction response in the position tracking test.

The rotation angle response is presented in Figure 5-18(a). In the Y axis, overshooting is evident at the start motion. The over contraction of PMA1 has led to a relative large angle change. The overshoot is mainly related to large airflow and comparatively slow operating speed of the solenoid valve at the beginning. Despite the overshoot, the desired angles from 0 to 20 seconds seems to be within the angle range. This result aligns with the workspace mapping results in Figure 5-16 that the beginning part of Task 2 is within prototype workspace trajectory. Finally, a 3D plot showing the end effector’s trajectory is drawn in Figure 5-18(b), so that the desired trajectory and the actual trajectory are compared.

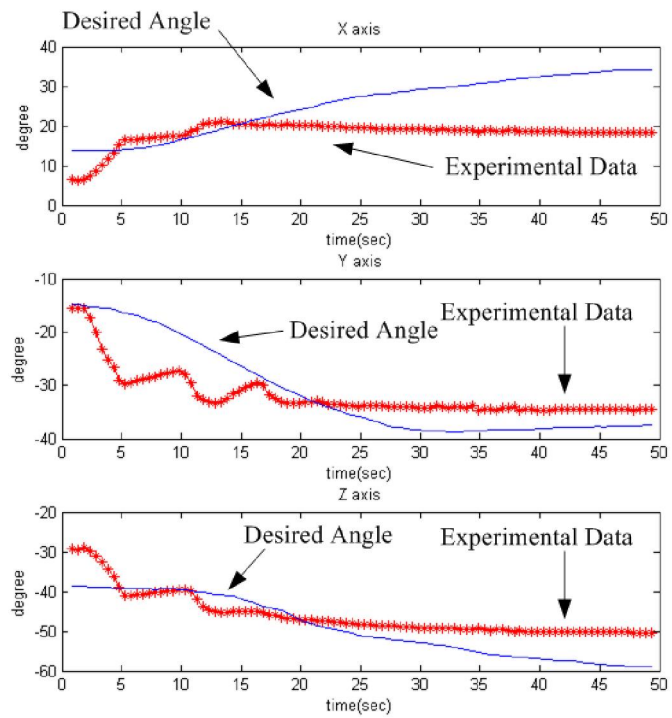


Figure 5-18: Shoulder joint angle tracking response, the red line denotes the practical response and the blue solid line denotes the desired trajectory

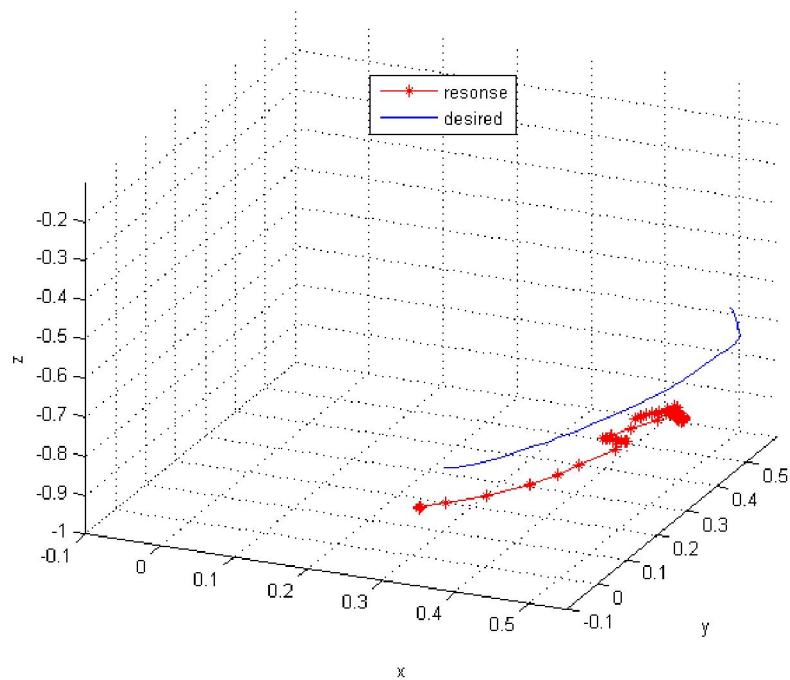


Figure 5-19: 3D plot of task trajectory and desired trajectory

### 5.4.3 Deficiency Analysis and Possible Strategies

As discussed before, the difference between the prototype workspace and the *3UPU* wrist mechanism workspace (the simulation in Appendix C ) is mainly caused by the restriction of the angles of the *3UPU* wrist mechanism in the prototype and the stroke limitation of the PMAs. The customised 3D rotational unit (illustrated in Figure 5-4 ), which is working as a human shoulder joint, also affects the prototype workspace. One way to reduce the effect of the 3D rotational unit on the prototype workspace is to add an additional flange bearing into the 3D rotational unit (between the universal joint and the upper arm), as shown in Figure 5-20. By adding this degree of freedom of rotation around the upper arm,  $\theta_z$  is not restricted anymore, thus the “*3D rotational unit*” constraint condition from Table 5-6: Reachable position condition in the prototype workspace is eliminated.

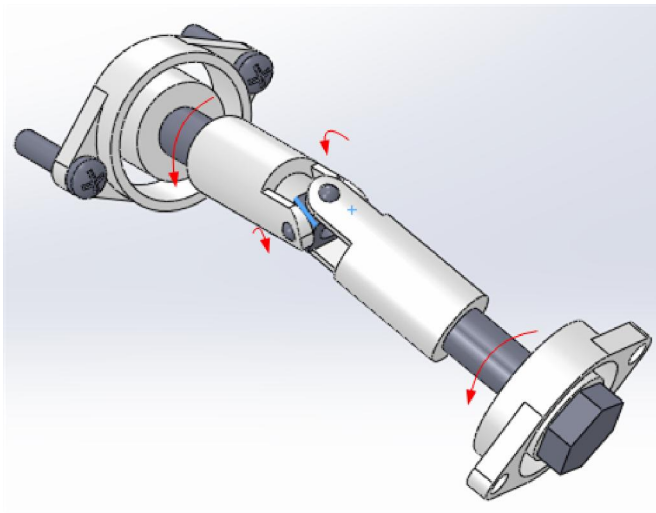


Figure 5-20: 3D rotational unit with additional flange bearing

Besides the 3D rotational unit’s mechanical restriction, actuator stroke is also a critical factor in determining the exoskeleton’s workspace. As was shown in Figure 5-16, the PMA only allows contraction between 70% and 100% of the specific PMAs maximum length, which is much smaller than other actuators (motor and gear, pneumatic cylinder). In the other three tasks (“*Hand to contra lateral shoulder*”, “*Combing hair*”, “*Hand to back pocket*”), this factor also shows large constraint. In motor and cable pulling systems, this issue is prevented because motors have infinite stroke. Of course, other issues related to the use of motors need to be considered in the design of robotic

exoskeletons.

With the modified 3D rotational unit (Figure 5-20), we performed the task of “*Hand to mouth*” again on the prototype. The same test procedures as used in Section 5.4.2 were used.

The single PMA’s contraction ratio response is plotted in Figure 5-21. In this figure, we can observe that each PMA contracts near the desired ratio. In PMA1, the desired contraction is over 30% and the PMA evidently failed to provide such stroke, due to its inherent characteristics. Therefore, refinement on the shoulder joint is effective in improving the prototype’s ADL task tracking capability; although some other factors (like the limited stroke) still hinder the exoskeleton from achieving the full range of desired motion.

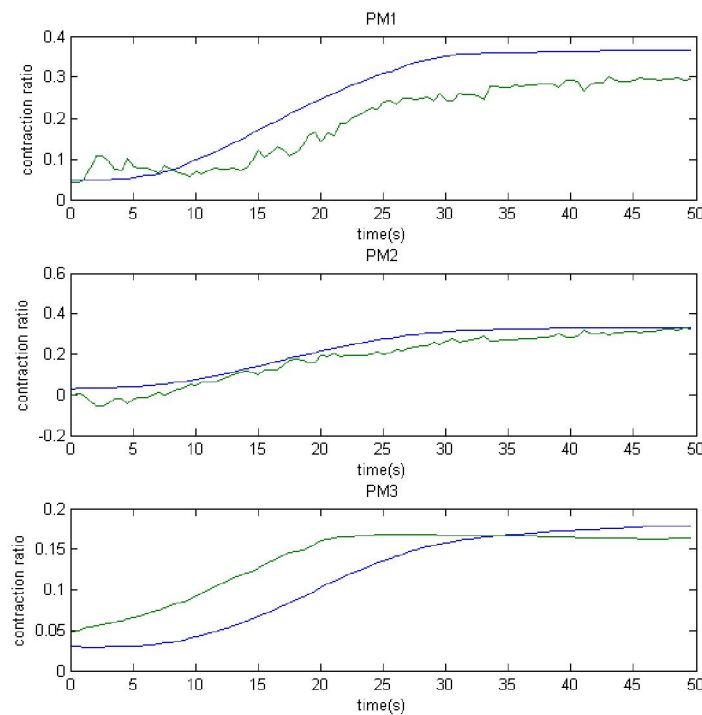


Figure 5-21: Pneumatic muscle contraction response after shoulder joint enhanced for task “Hand to mouth”

## Chapter 6 Conclusions and Future Work

### 6.1 Conclusions

The objective of this thesis is to develop dynamic models of pneumatic muscle actuators and design a new mechanism, towards developing a compact and light weight upper limb exoskeleton for providing sufficient kinematic capability to assist a human's upper limbs in their ADL. An enhanced dynamic model for the PMA is firstly developed in order to achieve accurate estimation. A model of the Coulomb friction element is introduced, and parameters such as pressure, displacement as well as external loads are considered in this model. With the Coulomb friction element, the developed dynamic force model of the PMAs shows valid enhancement through a series of constant load, instant compressed air flow input experiments. The estimated PMA's displacement response based on the developed dynamic force model is compared with the experimental data, as well as the simulation results based on other dynamic models (in which Coulomb friction force is regarded as a constant). This comparison shows that the developed model provides more accurate responses in most of the cases. The enhanced dynamic model can be used in developing model based control algorithms, such as sliding mode control.

A parallel mechanism, the *3UPU wrist* mechanism is analysed and implemented as the base of mechanical design of the shoulder exoskeleton. Besides the review of its kinematics characteristics, an alternative method of forward kinematics is developed, which is to calculate the platform's orientation from the angles of universal joints connected to the base, rather than from the length of the limbs. In accordance with two existing types of universal joints that are both capable of measuring their rotation angles, we developed two scenarios for the alternative forward kinematics. A case study of using the forward kinematics method in Scenario One to determine the rotation angles of the platform is presented. Scenario Two of the forward kinematics is experimentally verified.

A *3UPU wrist* test rig has been developed for verifying the inverse kinematics at several static positions. Then, Scenario Two of the alternative forward kinematics approach is implemented to estimate the platform's orientation. The estimation results are compared with the orientation results measured by the IMU sensor, in the static experiments. Solid results are obtained with estimation error within  $5^\circ$ .

A prototype shoulder exoskeleton based on the *3UPU wrist* mechanism and the PMA was developed. From the experiments of two basic upper limb motions, namely abduction and flexion, we observed satisfactory trajectory tracking capability. However the workspace of the prototype exoskeleton is limited, which is attributed to the PMAs' inextensibility at its normal length as well as its limited stroke in contraction (around 30% at maximum). Experiments with several ADL also showed that the prototype is capable of accomplishing motions within its effective workspace, but not the motions outside its effective workspace, which is caused by the limited contraction of the PMAs and the mechanical design of the prototype. By analysing possible factors that affect the prototype's workspace, several strategies are proposed. One strategy is applied and the performance in the same ADL task was improved.

## 6.2 Future Work

More studies on PMAs and the *3UPU wrist* mechanism are planned in the future works:

1. to develop more robust control algorithms (e.g. sliding model control) based on the developed dynamic PM force model
2. to study the alternative forward kinematics performance in dynamic environments
3. to study the force transmitted to the human shoulder joint when the *3UPU wrist* mechanism based robotic shoulder exoskeleton is implemented on a human shoulder.

As for the issue of limited workspace and kinematic performance, we wish to further improve the prototype by:

1. designing an orthogonal revolute pair to replace the current universal joint in the 3D rotational unit. This technique is relatively mature with its applications in multiple projects [44, 101, 19]
2. connecting an elastic spring serially to the PMA to allow longer pulling length.

## Reference

- [1] E. S. Lawrence, C. Coshall, R. Dundas, J. Stewart, a G. Rudd, R. Howard, and C. D. Wolfe, "Estimates of the prevalence of acute stroke impairments and disability in a multiethnic population," *Stroke: a journal of cerebral circulation*, vol. 32, no. 6, pp. 1279–84, Jun. 2001.
- [2] National Stroke Foundation, "Facts, figures and statistics, 10 things you should know about stroke," 2011. [Online]. Available: <http://www.strokefoundation.com.au/facts-figures-and-stats>. [Accessed: 12-Dec-2011].
- [3] Australian Institute of Health and Welfare, "Australia's health 2006," Canberra, Australia, 2006.
- [4] AIHW, "Heart,stroke and vascular diseases Australian facts," 2004.
- [5] CEDA, "Australia's Ageing Population: Meeting the Challenge," 2004.
- [6] M. Lee, M. Rittenhouse, and H. a. Abdullah, "Design Issues for Therapeutic Robot Systems: Results from a Survey of Physiotherapists," *Journal of Intelligent and Robotic Systems*, vol. 42, no. 3, pp. 239–252, Mar. 2005.
- [7] S. Masiero, A. Celia, G. Rosati, and M. Armani, "Robotic-assisted rehabilitation of the upper limb after acute stroke.," *Archives of physical medicine and rehabilitation*, vol. 88, no. 2, pp. 142–9, Feb. 2007.
- [8] K. Kiguchi, M. H. Rahman, M. Sasaki, and K. Teramoto, "Development of a 3DOF mobile exoskeleton robot for human upper-limb motion assist," *Robotics and Autonomous Systems*, vol. 56, pp. 678–691, 2008.
- [9] S. Hesse, H. Schmidt, C. Werner, and A. Bardeleben, "Upper and lower extremity robotic devices for rehabilitation and for studying motor control.," *Current opinion in neurology*, vol. 16, no. 6, pp. 705–10, Dec. 2003.
- [10] D. J. J. Reinkensmeyer, R. J. Sanchez, E. Wolbrecht, R. Smith, J. Liu, S. Rao, S. Cramer, T. Rahman, and J. E. Bobrow, "A Pneumatic Robot for Re-Training Arm Movement after Stroke: Rationale and Mechanical Design," *9th International Conference on Rehabilitation Robotics, 2005. ICORR 2005.*, pp. 500–504, 2005.
- [11] T. G. Sugar, J. He, E. J. Koeneman, J. B. Koeneman, R. Herman, H. Huang, R. S. Schultz, D. E. Herring, J. Wanberg, S. Balasubramanian, P. Swenson, J. a Ward, and S. Member, "Design and control of RUPERT: a device for robotic upper extremity repetitive therapy.," *IEEE transactions on neural systems and rehabilitation engineering: a publication of the IEEE Engineering in Medicine and Biology Society*, vol. 15, no. 3, pp. 336–46, Sep. 2007.

- [12] J. Klein, "Performance Enhancing Mechanisms for Human Manipulation by Manipulation," UNIVERSITY OF CALIFORNIA, IRVINE, 2009.
- [13] A. Frisoli, F. Rocchi, S. Marcheschi, A. Dettori, F. Salsedo, M. Bergamasco, A. F. F. Rocchi, S. M. A. Dettori, F. S. M. Bergamasco, P. Scuola, and S. S. Anna, "A New Force-Feedback Arm Exoskeleton for Haptic Interaction in Virtual Environments," *First Joint Eurohaptics Conference and Symposium on Haptic Interfaces for Virtual Environment and Teleoperator Systems*, pp. 195–201, 2005.
- [14] J. Rosen, M. Brand, M. B. Fuchs, and M. Arcan, "A myosignal-based powered exoskeleton system," *IEEE Transactions on Systems, Man, and Cybernetics - Part A: Systems and Humans*, vol. 31, no. 3, pp. 210–222, May 2001.
- [15] K. Xing, J. Huang, Q. Xu, and Y. Wang, "Design of A Wearable Rehabilitation Robotic Hand Actuated by Pneumatic Artificial Muscles," *Image Processing*, pp. 740–744, 2009.
- [16] C. Carignan and M. Liszka, "Design of an arm exoskeleton with scapula motion for shoulder rehabilitation," *ICAR '05. Proceedings., 12th International Conference on Advanced Robotics, 2005.*, pp. 524–531, 2005.
- [17] P. Bosscher and E. LaFay, "Haptic Cobot Exoskeleton Concepts and Mechanism Design," in *IDETC/CIE*, 2006, pp. 1–10.
- [18] S. K. Mustafa, G. Yang, S. H. Yeo, and W. Lin, "Optimal design of a bio-inspired anthropocentric shoulder rehabilitator," *Applied Bionics and Biomechanics*, vol. 3, no. 3, pp. 199–208, 2006.
- [19] Y. Mao and S. K. Agrawal, "A Cable Driven Upper Arm Exoskeleton for Upper Extremity Rehabilitation," *Robotics*, pp. 4163–4168, 2011.
- [20] Y. Jeong, Y. K. Kim, K. Kim, J. Park, and P. O. Box, "Design and control of a wearable robot," *Proceedings 10th IEEE International Workshop on Robot and Human Interactive Communication. ROMAN 2001 (Cat. No.01TH8591)*, pp. 636–641.
- [21] S. Salimi, S. Simon Park, and T. Freiheit, "Dynamic response of intraocular pressure and biomechanical effects of the eye considering fluid-structure interaction.,", *Journal of biomechanical engineering*, vol. 133, no. 9, p. 091009, Sep. 2011.
- [22] D. G. Caldwell, G. a. Medrano-Cerda, and M. Goodwin, "Control of pneumatic muscle actuators," *IEEE Control Systems Magazine*, vol. 15, no. 1, pp. 40–48, 1995.
- [23] R. W. R. W. Colbrunn, G. M. G. M. Nelson, and R. D. R. D. Quinn, "Modeling of Braided Pneumatic Actuators for Robotic Control," in *Proceedings 2001 IEEE/RSJ International Conference on Intelligent Robots and Systems. Expanding the Societal Role of Robotics in the the Next Millennium (Cat. No.01CH37180)*, 2001, pp. 1964–1970.

- [24] M. D. Klein Breteler, C. W. Spoor, and F. C. Van der Helm, "Measuring muscle and joint geometry parameters of a shoulder for modeling purposes.," *Journal of biomechanics*, vol. 32, no. 11, pp. 1191–7, Nov. 1999.
- [25] H. E. Veeger, "The position of the rotation center of the glenohumeral joint.," *Journal of biomechanics*, vol. 33, no. 12, pp. 1711–5, Dec. 2000.
- [26] F. C. Van der Helm, H. E. Veeger, G. M. Pronk, L. H. Van der Woude, and R. H. Rozendal, "Geometry parameters for musculoskeletal modelling of the shoulder system.," *Journal of biomechanics*, vol. 25, no. 2, pp. 129–44, Feb. 1992.
- [27] J. Galinat, "Normal Glenohumeral and Abnormal Joint Mechanics of the Plane in the Horizontal," *Surgery*, vol. 70, no. 2, 1988.
- [28] D. T. Harryman, J. A. Sidles, S. L. Harris, and F. A. Matsen, "Laxity of the normal glenohumeral joint: A quantitative in vivo assessment," *Journal of Shoulder and Elbow Surgery* 1, pp. 66–76, 1992.
- [29] C. Doorenbosch, A. Mourits, D. Veeger, J. Harlaar, F. van der Helm, and others, "Determination of functional rotation axes during elevation of the shoulder complex.," *The Journal of orthopaedic and sports physical therapy*, vol. 31, no. 3, p. 133, 2001.
- [30] N. Klopčar, M. Tomsic, and J. Lenarčič, "A kinematic model of the shoulder complex to evaluate the arm-reachable workspace.," *Journal of biomechanics*, vol. 40, no. 1, pp. 86–91, Jan. 2007.
- [31] J. Rosen, J. C. Perry., N. Manning, S. Burns, and B. Hannaford, "The human arm kinematics and dynamics during daily activities - toward a 7 DOF upper limb powered exoskeleton.," *ICAR '05. Proceedings., 12th International Conference on Advanced Robotics, 2005.*, no. July, pp. 532–539, 2005.
- [32] C. Anglin and U. P. Wyss, "Review of arm motion analyses.," *Proceedings of the Institution of Mechanical Engineers. Part H, Journal of engineering in medicine*, vol. 214, no. 5, pp. 541–55, Jan. 2000.
- [33] I. A. Murray and G. R. Johnson, "A study of the external forces and moments at the shoulder and elbow while performing every day tasks.," *Clinical biomechanics (Bristol, Avon)*, vol. 19, no. 6, pp. 586–94, Jul. 2004.
- [34] M. A. Buckley, A. Yardley, G. R. Johnson, and D. A. Carus, "Dynamics of the upper limb during performance of the tasks of everyday living--a review of the current knowledge base.," *Proceedings of the Institution of Mechanical Engineers. Part H, Journal of engineering in medicine*, vol. 210, no. 4, pp. 241–7, Jan. 1996.

- [35] K. N. An, L. J. Askew, and E. Y. Chao, "Biomechanics and functional assessment of upper extremities," *Trends in Ergonomics/Human Factors III*, 1986.
- [36] P. Letier, M. Avraam, S. Veillerette, M. Horodincea, M. De Bartolomei, A. Schiele, and A. Preumont, "SAM: A 7-DOF portable arm exoskeleton with local joint control," *2008 IEEE/RSJ International Conference on Intelligent Robots and Systems*, pp. 3501–3506, Sep. 2008.
- [37] K. S. Saladin, *Anatomy & Physiology: 5th edition*, 5th Editio. McGraw-Hill, 2010.
- [38] C. Chen and D. Jackson, "Parameterization and Evaluation of Robotic Orientation Workspace: A Geometric Treatment," *IEEE Transactions on Robotics*, vol. 27, no. 4, pp. 656–663, Aug. 2011.
- [39] J. C. Perry and J. Rosen, "Design of a 7 Degree-of-Freedom Upper-Limb Powered Exoskeleton," *The First IEEE/RAS-EMBS International Conference on BioRob 2006.*, pp. 805–810, 2006.
- [40] T. Nef and R. Riener, "ARMin - Design of a Novel Arm Rehabilitation Robot," *9th International Conference on Rehabilitation Robotics, 2005. ICORR 2005.*, pp. 57–60, 2005.
- [41] "Harmonic Drive." [Online]. Available: <http://www.harmonicdrive.net/products/actuators/>. [Accessed: 14-Dec-2011].
- [42] M. Tavakoli, L. Marques, and A. T. de Almeida, "A Comparison Study on Pneumatic Muscles and electrical motors," in *2008 IEEE International Conference on Robotics and Biomimetics*, 2009, pp. 1590–1594.
- [43] J. Klein, S. J. J. Spencer, J. Allington, K. Minakata, E. T. Wolbrecht, R. Smith, J. E. Bobrow, D. J. Reinkensmeyer, and S. Member, "Biomimetic orthosis for the neurorehabilitation of the elbow and shoulder (BONES)," *2008 2nd IEEE RAS & EMBS International Conference on Biomedical Robotics and Biomechatronics*, pp. 535–541, Oct. 2008.
- [44] X. Z. Zheng, H. Z. Bin, and Y. G. Luo, "Kinematic analysis of a hybrid serial-parallel manipulator," *The International Journal of Advanced Manufacturing Technology*, vol. 23, no. 11–12, pp. 925–930, Apr. 2004.
- [45] S. K. Agrawal, V. N. Dubey, J. J. Gangloff, E. Brackbill, Y. Mao, and V. Sangwan, "Design and Optimization of a Cable Driven Upper Arm Exoskeleton," *Journal of Medical Devices*, vol. 3, no. 3, p. 031004, 2009.
- [46] S. K. Mustafa, "Kinematic calibration of a 7-DOF self-calibrated modular cable-driven robotic arm," *2008 IEEE International Conference on Robotics and Automation*, pp. 1288–1293, May 2008.

- [47] S. K. Mustafa, S. H. Yeo, C. B. Pham, G. Yang, and W. Lin, "A biologically-inspired anthropocentric shoulder joint rehabilitator: workspace analysis & optimization," *IEEE International Conference Mechatronics and Automation*, 2005, no. July, pp. 1045–1050, 2005.
- [48] A. T. Submitted, "Design and Control of a Haptic Arm Exoskeleton Abstract Design and Control of a Haptic Arm Exoskeleton," *Optimization*, 2004.
- [49] Y. Mao and S. K. Agrawal, "Wearable Cable-driven Upper Arm Exoskeleton - Motion with Transmitted Joint Force and Moment Minimization," *Constraints*, pp. 4334–4339, 2010.
- [50] D. T. Harryman, J. A. Sidles, J. M. Clark, K. J. Mcquade, T. D. Gibb, and F. A. Matsen, "Translation of the humeral head on the glenoid with passive glenohumeral motion Translation of the Humeral Head with Passive Glenohumeral on the Glenoid Motion \*," *Surgery*, 2011.
- [51] C. M. Gosselin, E. St. Pierre, and M. . Gagne, "On the development of the Agile Eye," *Robotics*, 1996.
- [52] R. J. Saltaren, J. M. Sabater, E. Yime, J. M. Azorin, R. Aracil, and N. Garcia, "Performance evaluation of spherical parallel platforms for humanoid robots," *Robotica*, vol. 25, no. 03, p. 257, Aug. 2006.
- [53] M. Karouia and J. M. Hervé, *A three-dof tripod for generating spherical rotation.pdf*. Advances in Robot Kinematics, J. Lenarcic and M. M. Stanisic, eds., Kluwer Academic, London, 2000, pp. pp. 395–4020.
- [54] L. Romdhane, "Design and analysis of a hybrid serial-parallel manipulator," *Mechanism and Machine Theory*, vol. 34, no. 7, pp. 1037–1055, Oct. 1999.
- [55] D. Zlatanov, I. a. Bonev, and C. M. Gosselin, "Constraint singularities of parallel mechanisms," *Proceedings 2002 IEEE International Conference on Robotics and Automation (Cat. No.02CH37292)*, no. May, pp. 496–502, 2002.
- [56] Z. Xiangzhou, L. Yougao, and B. Hongzan, "Inverse Dynamics of 3-UPU Parallel Mechanism with Pure Rotation Based on D'Alembert Principle," *2007 International Conference on Mechatronics and Automation*, pp. 2842–2847, Aug. 2007.
- [57] R. Kratz, S. Klug, M. Stelzer, O. von Stryk, and O. Von Stryk, "Biologically Inspired Reflex Based Stabilization Control of a Humanoid Robot with Artificial SMA Muscles," *2006 IEEE International Conference on Robotics and Biomimetics*, pp. 1089–1094, 2006.
- [58] F. Carpi and D. De Rossi, "Electroactive Polymer-Based Devices for e-Textiles in Biomedicine," *Technology*, vol. 9, no. 3, pp. 295–318, 2005.
- [59] C. Chou and B. Hannaford, "Measurement and modeling of McKibben pneumatic artificial muscles," *Robotics*, vol. 12, no. 1, pp. 90–102, 1996.

- [60] M. B. Binnard, "Design of a Small Pneumatic Walking Robot," M.I.T., 1995.
- [61] Z. Fan, K. Raun, L. Hein, and H. Kiil, "Application of Artificial Muscles as Actuators in Engineering Design," in *DVANCED DESIGN AND MANUFACTURE TO GAIN A COMPETITIVE EDGE*, Springer London, 2008, pp. 875–884.
- [62] T. B. Wolfe, M. G. Faulkner, and J. Wolfaardt, "Development of a shape memory alloy actuator for a robotic eye prosthesis," *Smart Materials and Structures*, vol. 14, no. 4, pp. 759–768, Aug. 2005.
- [63] F. Daerden and D. Lefeber, "Pneumatic Artificial Muscles: actuators for robotics and automation," *European journal of Mechanical and Environmental Engineering*, 2000.
- [64] J. W. Hurst, J. E. Chestnutt, and A. A. Rizzi, "The Actuator With Mechanically Adjustable Series Compliance," *Robotics*, vol. 26, no. 4, pp. 597–606, 2010.
- [65] B. Vanderborght, T. Sugar, and D. Lefeber, "Adaptable compliance or variable stiffness for robotic applications [From the Guest Editors]," *IEEE Robotics & Automation Magazine*, vol. 15, no. 3, pp. 8–9, Sep. 2008.
- [66] M. A. Lemay, N. Hogan, and J. W. A. Van Dorsten, "Issues in Impedance Selection and Input Devices for Multijoint Powered Orthotics," *Rehabilitation Engineering*, vol. 6, no. 1, pp. 102–105, 1998.
- [67] G. a. Pratt and M. M. Williamson, "Series elastic actuators," *Proceedings 1995 IEEE/RSJ International Conference on Intelligent Robots and Systems. Human Robot Interaction and Cooperative Robots*, no. 1524, pp. 399–406, 1995.
- [68] V. Duindam and S. Stramigioli, "Optimization of Mass and Stiffness Distribution for Efficient Bipedal Walking," in *International Symposium on Nonlinear Theory and its Applications*, 2005, pp. 1–4.
- [69] I. Sardellitti, O. Khatib, and D. Shin, "A hybrid actuation approach for human-friendly robot design," *2008 IEEE International Conference on Robotics and Automation*, pp. 1747–1752, May 2008.
- [70] K. Narioka, R. Niiyama, Y. Ishii, and K. Hosoda, "Pneumatic Musculoskeletal Infant Robots," *Science And Technology*.
- [71] R. Kratz, M. Stelzer, M. Friedmann, and O. Von Stryk, "Control Approach for a Novel High Power-To-Weight Ratio Actuator Scalable in Force and Length for Robots," in *International Conference on Advanced Intelligent Mechatronics*, 2007.
- [72] C. Pfeiffer, K. Delaurentis, and C. Mavroidis, "Shape Memory Alloy Actuated Robot Prostheses: Initial Experiments," in *Proc. of IEEE International Conf. on Robotics and Auto*, 1999.

- [73] F. Carpi, G. Frediani, A. Mannini, and D. De Rossi, "Contractile and Buckling Actuators Based on Dielectric Elastomers: Devices and Applications," *Advances in Science and Technology*, vol. 61, pp. 186–191, 2008.
- [74] F. Carpi, A. Mannini, and D. De Rossi, "Elastomeric contractile actuators for hand rehabilitation splints," in *SPIE*, 2008, pp. 692705–692705–10.
- [75] D. De Rossi, F. Carpi, and F. Galantini, "Functional Materials for Wearable Sensing , Actuating and Energy Harvesting," *Science And Technology*, vol. 57, pp. 247–256, 2008.
- [76] R. Gaylord, "Fluid Actuated Motor System and Stroking Device," U.S. Patent 2844126, 1958.
- [77] P. Tondu, B., Lopez, "Modelling and control of McKibben artificial muscle robot actuator," *IEEE Control Systems Magazine*, vol. 20, pp. 15–38, 2000.
- [78] R. W. Colbrunn, G. M. Nelson, and R. D. Quinn, "Modeling of braided pneumatic actuators for robotic control," in *Proceedings 2001 IEEE/RSJ International Conference on Intelligent Robots and Systems. Expanding the Societal Role of Robotics in the the Next Millennium (Cat. No.01CH37180)*, 2001, pp. 1964–1970.
- [79] P. B. Petrovic, "Modeling and control of an artificial muscle part one: Model building," in *Xth Conference on Mechanical Vibration*, 2002, p. 93.
- [80] A. Pujana-arrese, A. Martinez-esnaola, and J. Landaluze, "Modelling in Modelica of a pneumatic muscle: application to model an experimental set-up," in *21st European conference on modelling and simulation, ECMS*, 2007.
- [81] K. C. Wickramatunge and T. Leephakpreeda, "Empirical Modeling of Pneumatic Artificial Muscle," in *International multiconference of Engineers and Computer Scientists IMECS 2009*, 2009, vol. II, no. 0, pp. 3–7.
- [82] T. Itto, "Hybrid Modeling of McKibben Pneumatic Artificial Muscle Systems," in *2011 IEEE International Conference on Industrial Technology (ICIT)*, 2011, pp. 65–70.
- [83] B. Kang, C. S. Kothera, B. K. S. Woods, and N. M. Wereley, "Dynamic Modeling of Mckibben Pneumatic Artificial Muscles for Antagonistic Actuation," in *IEEE International Conference on Robotics and Automation*, 2009, pp. 182–187.
- [84] D. B. Reynolds, D. W. Repperger, C. A. Phillips, and G. Bandry, "Modeling the Dynamic Characteristics of Pneumatic Muscle," *Annals of Biomedical Engineering*, vol. 31, pp. 310–317, 2003.
- [85] S. Balasubramanian, H. Huang, S. Member, J. He, and S. Member, "Quantification of Dynamic Property of Pneumatic Muscle Actuator," in *Proceedings of the 28th IEEE EMBS Annual International Conference*, 2006, pp. 2734–2737.

- [86] R. W. COLBRUNN, G. M. Nelson, and R. D. Quinn, "Design and control of a robotic leg with braided pneumatic actuators," in *Proceedings. 2001 IEEE/RSJ International Conference on Intelligent Robots and Systems*, 2000.
- [87] P. Carbonell, Z. P. Jiang, and D. W. Repperger, "Nonlinear control of a pneumatic muscle actuator: backstepping vs. sliding-mode," *Proceedings of the 2001 IEEE International Conference on Control Applications (ICCA '01)*, vol. 2, pp. 167–172, 2001.
- [88] S. W. Chan, J. H. Lilly, D. W. Repperger, and J. E. Berlin, "Fuzzy PD+I learning control for a pneumatic muscle," *The 12th IEEE International Conference on Fuzzy Systems, 2003. FUZZ '03.*, pp. 278–283.
- [89] M.-K. Chang, "An adaptive self-organizing fuzzy sliding mode controller for a 2-DOF rehabilitation robot actuated by pneumatic muscle actuators," *Control Engineering Practice*, vol. 18, no. 1, pp. 13–22, 2010.
- [90] X. Shen, "Nonlinear model-based control of pneumatic artificial muscle servo systems," *Control Engineering Practice*, vol. 18, no. 3, pp. 311–317, Mar. 2010.
- [91] T. Thanh and K. Ahn, "Nonlinear PID control to improve the control performance of 2 axes pneumatic artificial muscle manipulator using neural network," in *Mechatronics*, 2001, vol. 16, no. 9, pp. 577–587.
- [92] S. Chillari, S. Guccione, and G. Muscat, "An Experimental Comparison Between Several Pneumatic Position Control Methods," *Decision and Control, 2001. Proceedings of the 40th IEEE Conference on*, 2001.
- [93] T.-J. Yeh, M.-J. Wu, T.-J. Lu, F.-K. Wu, and C.-R. Huang, "Control of McKibben pneumatic muscles for a power-assist, lower-limb orthosis," *Mechatronics*, vol. 20, no. 6, pp. 686–697, Sep. 2010.
- [94] L. Fei, W. Yu, T. Heting, R. P. S. Han, and M. Pam, "Empirically-Sourced Mechanical Behaviors of Pneumatic Artificial Muscles for Compensation-Based Controls," *Materials Research*, vol. 186, pp. 31–35, 2011.
- [95] C. Huang, C. Chang, M. Yu, and L. Fu, "Sliding-Mode Tracking Control of the Stewart Platform," *Electrical Engineering*.
- [96] A. Pytel, J. Kiusalaas, and I. Sharma, "Engineering Mechanics: Statics, Volume 1," 3rd ed., 2010, p. 584.
- [97] E. L. Houghton and P. W. Carpenter, *Aerodynamics for Engineering Students*, vol. 85, no. 4. Butterworth-Heinemann, 2003, pp. 500–503.
- [98] B. W. McCormick, "Aerodynamics, aeronautics, and flight mechanics," Wiley, 1995.

- [99] K. C. Wickramatunge and T. Leephakpreeda, "Empirical Modeling of Pneumatic Artificial Muscle," *Computer*, vol. II, no. 0, pp. 3–7, 2009.
- [100] L.-W. Tsai and S. Joshi, "Kinematics and Optimization of a Spatial 3-UPU Parallel Manipulator," *Journal of Mechanical Design*, vol. 122, no. 4, p. 439, 2000.
- [101] R. Di Gregorio, "Kinematics of the 3-UPU wrist," *Mechanism and Machine Theory*, vol. 38, no. 3, pp. 253–263, Mar. 2003.
- [102] S. CALANDE, "2D picture (coronal or sagittal view) from 55 2D picture (axial view)." [Online]. Available: <http://www.itk.org/pipermail/insight-users/2008-September/027427.html>. [Accessed: 30-Sep-2008].
- [103] H. Sadjadian and H. D. Taghirad, "Numerical Methods for Computing the Forward Kinematics of a Redundant Parallel Manipulator," in *Proceedings of the IEEE Conference on Mechatronics and Robotics*, pp. 557–562.
- [104] P. G. De Santos, J. A. Galvez, J. Estremera, and E. Garcia, "SIL04: a true walking robot for the comparative study of walking machine techniques," *Robotics & Automation Magazine, IEEE*, vol. 10, no. 4, pp. 23–32, 2003.
- [105] P. B. Goldsmith, "Kinematics and Stiffness," no. May, pp. 2–7, 2002.
- [106] R. Di Gregorio, "Statics and Singularity Loci of the 3-UPU Wrist," vol. 20, no. 4, pp. 630–635, 2004.
- [107] Alps, "11mm Size Insulated Shaft Snap-in Type RK11K Series."
- [108] P. U. Joints, B. C. Pieces, and H. O. W. T. O. Order, "HUCO-POL Single joints HUCO-POL," *Main*, pp. 28–29.
- [109] C. J. Van Andel, N. Wolterbeek, C. a M. Doorenbosch, D. H. E. J. Veeger, J. Harlaar, and C. J. Van Andel, "Complete 3D kinematics of upper extremity functional tasks.," *Gait & posture*, vol. 27, no. 1, pp. 120–7, Jan. 2008.
- [110] The Shadow Robot Company, "Shadow Air Muscle," 2011.
- [111] F. Daerden, "Conception and realization of pleated pneumatic artificial muscles and their use as compliant actuation elements," *PhD Thesis Vrije Universiteit Brussel, Belgium*, 1999.
- [112] D. A. Winter, "Biomechanics and Motor Control of Human Movement." John Wiley & Sons, Inc., Hoboken, NJ, USA, 23-Sep-2009.

- [113] G. Yang, E. Hui, L. Ho, W. Lin, and I. Chen, "A Differential Geometry Approach for the Workspace Analysis of Spherical Parallel Manipulators," in *Proceedings of the th World Congress in Mechanism and Machine Science*, 2003.

## Appendix A Experiments for Obtaining a Static Model for the PMA

In Appendix A the process of using an experimental approach to determine the coefficients ( $K_1$ ,  $K_2$ ,  $C_1$ ,  $S_1$ ,  $S_2$ ,  $S_3$ ) of the static force model (3-9) of the PMA ( $\Phi 6-300$  mm) is presented.

### A.1 Experimental Setup

The experimental setup is illustrated in Figure A-1. As shown, the air inlet end of the PMA was securely mounted on a plate. In experiments with different contraction lengths  $x(t)$ , the free hanging end was adjusted and fixed at various positions on the slotted track. At each length position, the solenoid valve was fully opened and the regulator was slowly adjusted so that the pressure rose from  $0.4$  bar to around  $4$  bar. According to the Shadow Air Muscle specification [110],  $4$  bar is the highest safe operating pressure. During the adjustment process, the force and pressure were recorded by a load cell and pressure transducer, respectively. Both the excitation and relaxation processes were executed.

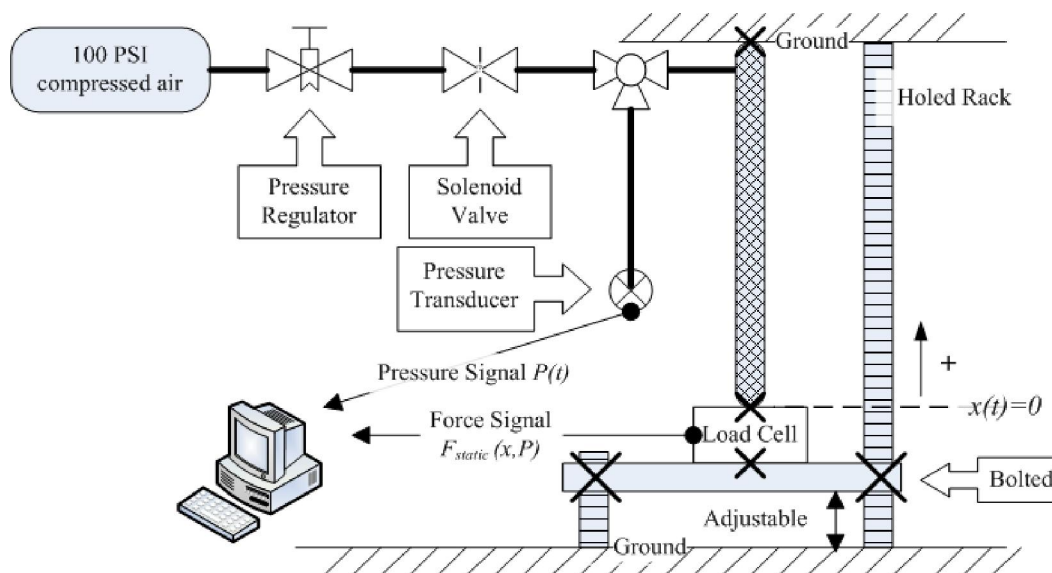


Figure A-1: Experimental setup of the PMA

At each length position (constant PMA length), the experimental results were initially presented in the form of a pressure-time plot and a force-time plot. Figure A-2(a) and Figure A-2(b) show samples of the excitation and relaxation results, respectively. In the excitation test, a contraction

length is fixed at  $82.7\text{ mm}$  (Figure A-2(a)); and in the relaxation test, a contraction length is  $50.4\text{ mm}$  (Figure A-2(b)).

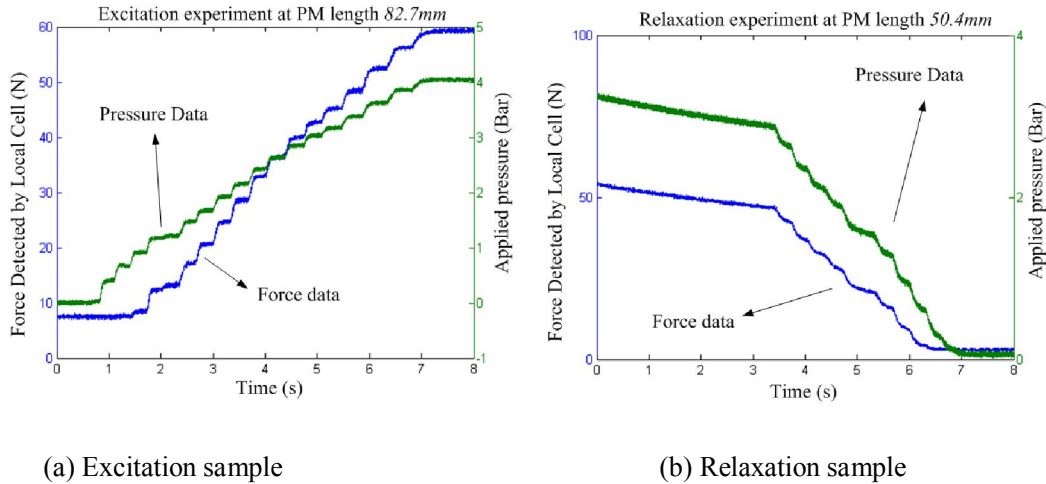


Figure A-2: Sample data of experiments with the  $\Phi 6\text{--}300\text{ mm}$  PMA

## A.2 Experimental Results and Static Model

The force data against pressure data relationships at each fixed length position are presented in Figure A-3. In this figure, each line represents a set of force-pressure relationships for one length of the  $\Phi 6\text{--}300\text{ mm}$  PMA. The blue straight lines show the approximated linear relationship between the pressure and the force with a fixed length. In both the excitation and relaxation results, a linear relationship between is found despite some misalignment in the lower pressure region (from  $0\text{ bar}$  to below  $1\text{ bar}$ ) of each plot. The misalignment of real data is attributed to the insufficiently pressurised tubes inside the PMA when the pressure is low. For this region, the force model of the PMA does not apply.

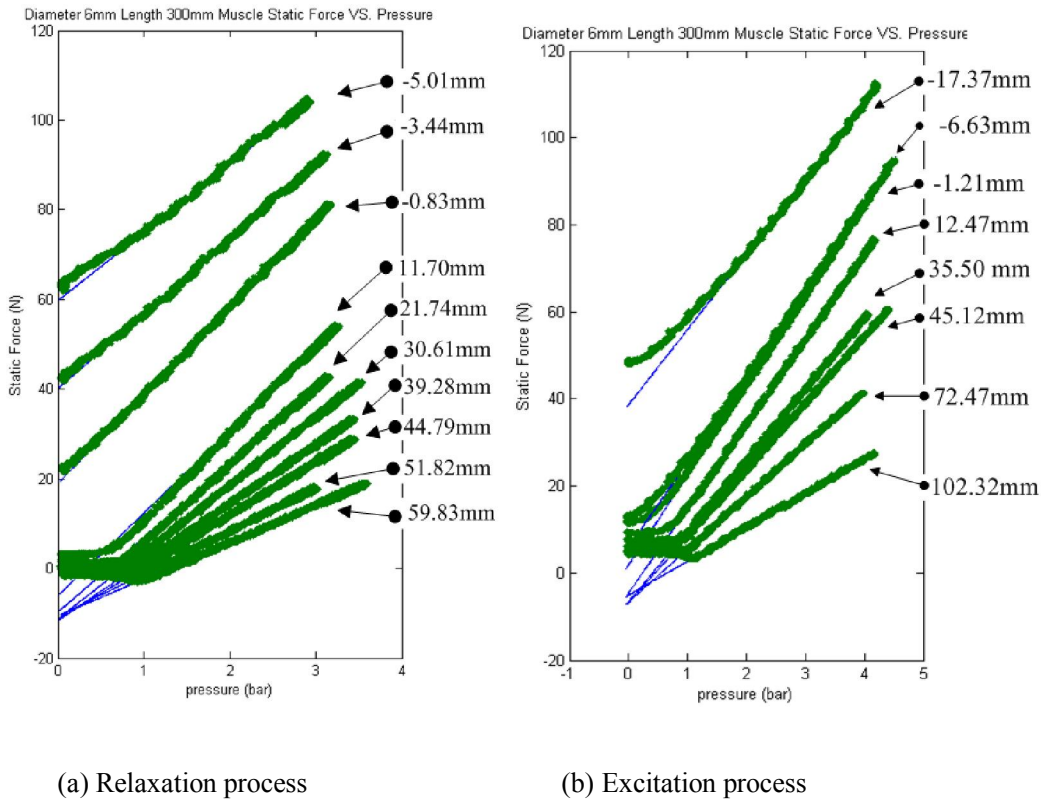


Figure A-3:  $\Phi 6-300$  mm PMA static experiment results: pressure-force relationship with different muscle length

The results in Figure A-3 are in accordance with the static force model from Equation (3-6), because in both the results of the plot and the force model, the linear relation of pressure  $P(t)$  and static force  $F_{static}(x,P)$  is indicated. It is also noticed that as contraction length  $x(t)$  increases, the range of the insufficiently pressurised period increases, and the slope of the linear relation between  $F_{static}(x,P)$  and  $P(t)$  drops. Actually, it was demonstrated by other literature [105, 24] that when the contraction length  $x(t)$  reaches over the PMA's maximum contraction length, the linear relation of  $F_{static}(x,P)$  and  $P(t)$  becomes a horizontal line. In other words, the PMA exerts no forces after  $x(t)$  is greater the maximum contraction length. On the contrary, if the PMA is fixed at an elongated position where the contraction length  $x(t)$  is defined as negative, we observed the linear relationship between the pressure and the force in the full range. The starting points of contraction force in these cases are increased from zero to a value denoting a passive elongation force on the PMA. It is observed that the slope of  $F_{static}(x, P)$  versus  $P(t)$  line becomes higher when the contraction length  $x(t)$  gets nearer to zero. This is in consistence with the statement in [111] and [23] that the PMA's

exertion force reaches the largest when the contraction length is zero.

The linear regression in Figure A-3 is expressed as:

$$F_{static-i}(P) = L_i P(t) + J_i \quad (i = 1, 2, \dots, 10) \quad (A-1)$$

$$F_{static-j}(P) = L_j P(t) + J_j \quad (j = 1, 2, \dots, 8) \quad (A-2)$$

Where  $L_i$ ,  $L_j$  and  $J_i$ ,  $J_j$  are the fitted coefficients;  $P(t)$  and  $F_{static-i/ static-j}(P)$  are the continuous pressure and force; and subscripts  $i$  and  $j$  label each group of positions in the relaxation and excitation processes, respectively. The corresponding displacement as well as the fitted  $L_i$ ,  $L_j$  and  $J_i$ ,  $J_j$  of each  $i(i = 1, 2, \dots, 10)$  and  $j(j = 1, 2, \dots, 8)$  are listed in Table A-1.

Derived from Equation (3-6), for each  $x_i$ , Equation (3-11) can be presented as:

$$F_{static-i}(x_i, P) = (K_1 x_i^2 + K_2 x_i + C_1)P(t) + S_1 x_i^2 + S_2 x_i + S_3 \quad (i = 1, 2, \dots, 10) \quad (A-3)$$

Substituting Equation (A-3) into (A-1) and (A-2), we have a multiple series of:

$$\begin{cases} L_i = (K_1 x_i^2 + K_2 x_i + C_1) \\ J_i = S_1 x_i^2 + S_2 x_i + S_3 \end{cases} \quad (i = 1, 2, \dots, 10) \quad (A-4)$$

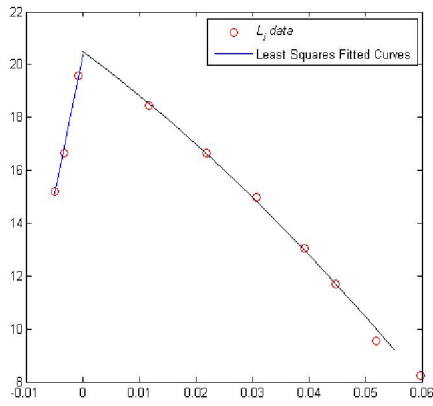
The 10 groups' values of  $L_i$  and  $J_i$  are acquired from the data and curve shown in Figure A-3(a). Table A-1 presents these values. The negative contraction length  $x_i$  is presented in the last two columns. This denotes that the PMA is in an elongated status, i.e. the PMA is stretched and immobilised at a longer length than the nominal length. The force-displacement characteristics of the PMA when elongated are different from when it is shortened. It is found that the elongation length is related to external force in a different pattern. Generally, the slope of the force-displacement line drops more dramatically in the elongation period than in the contraction period, given the same amount of displacement change. Yet, thanks to the inelastic characteristics of the outer mesh nylon shell, the elongation displacement range is very small (up to around 10 mm for the  $\Phi 6-300$  mm PMA) compared to the contraction length range. Therefore, in the practical operation where the other end of the PMA can move freely and sufficient activation compressed air is provided, the PMA experiences a quick transition from elongation to contraction. As such, it is

assumed that the model for the contraction period characterises the main feature of the PMA. Thus, we only present the contraction model in this research. The 10 lengths are roughly equally spanned between the contraction ratios from 0% to 30%.

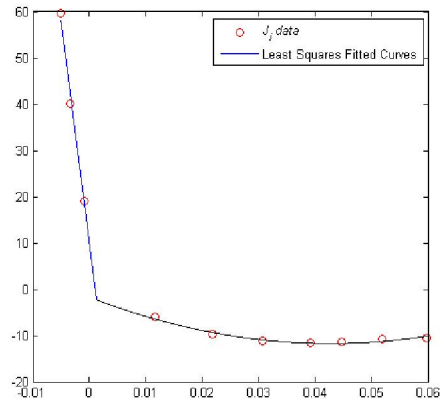
Table A-1: The linear fitting results of  $L_i$  and  $J_i$  for the relaxation process of the PMA  $\Phi 6-300\text{ mm}$

$i$	1	2	3	4	5	6	7	8	9	10
$x_i\text{ (mm)}$	5.01	11.7	21.7	30.6	39.3	44.8	51.8	59.8	-3.4	-0.8
$L_i\text{ (N/bar)}$	15.2	18.5	16.7	15.0	13.1	11.7	9.5	8.2	16.7	19.6
$J_i\text{ (N)}$	59.8	-6.0	-9.7	-11.2	-11.6	-11.4	-10.7	-10.6	40.1	19.0
$x_j\text{ (mm)}$	-2.03	-17.9	-6.78	11.34	34.77	43.77	71.10	104.11	/	/
$L_j\text{ (N/bar)}$	20.54	16.96	19.82	19.43	16.31	15.31	12.01	7.79	/	/
$J_j\text{ (N)}$	2.41	39.80	5.59	-4.53	-6.66	-6.91	-6.58	-5.03	/	/

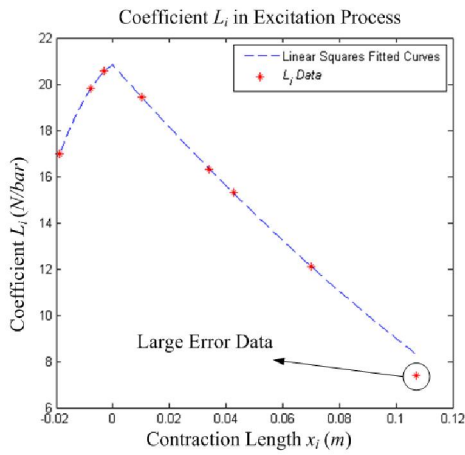
The slope ( $L_i/L_j$ ) and intercept ( $J_i/J_j$ ) of the force-displacement linear lines are plotted in Figure A-3. The nonlinear least squares fitting approach based on the polynomial functions in Figure A-3 is performed to obtain the relations of  $L_i/L_j$  and  $x_i/x_j$ , as well as the relations of  $J_i/J_j$  and  $x_i/x_j$ . The corresponding fitted curves are plotted in Figure A-4 as well. Different coefficients are developed for both the elongation period and the contraction period. Figure A-4 shows the polynomial fitting plots of  $L_i/L_j$  and  $J_i/J_j$  with different muscle length, respectively. In the excitation process, we discarded data that was evidently away from the general pattern.



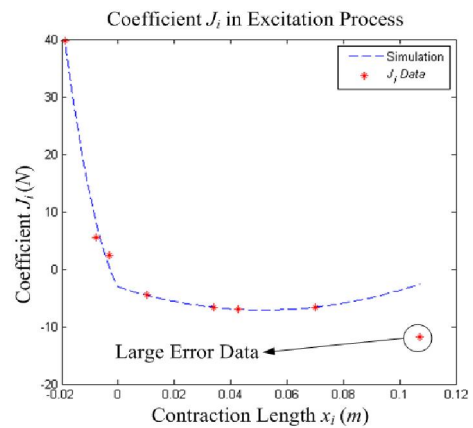
(a) Fitting plot of  $L_i$  in relaxation process



(b) Fitting plot of  $J_i$  in relaxation process



(c) Fitting plot of  $L_j$  in excitation process



(d) Fitting plot of  $J_j$  in excitation process

Figure A-4: A polynomial fitting of  $L_i$ ,  $J_i$ ,  $L_j$  and  $J_j$  for the static model

Table A-2 presents the model coefficients for the contraction period by the least squares fitting technique.

Table A-2: Coefficients of the static model for the PMA  $\Phi 6-300$  mm

Relaxation	$K_1 = -846.37 \times 10^{-5}$	$K_2 = -158.68 \times 10^{-5}$	$C_1 = 20.4 \times 10^{-5}$	$S_1 = 5511$	$S_2 = -471.5$	$S_3 = -1.635$
Excitation	$K_1 = 51.962 \times 10^{-5}$	$K_2 = -131.122 \times 10^{-5}$	$C_1 = 20.8 \times 10^{-5}$	$S_1 = 1162$	$S_2 = -137.9$	$S_3 = -3.2$

The coefficients for the higher order terms ( $K_1$ ,  $K_2$ ,  $S_1$  and  $S_2$ ) are found to be different between the relaxation and excitation models. However, the impact of these differences on the resultant force is comparatively smaller than coefficients for the lower order terms ( $K_3$  and  $S_3$ ) because the higher order terms of contraction displacement scaled them down. The values in the relaxation and

excitation processes are slightly different, this can be explained by difference of the coulomb friction [59].

The developed static model for the PMA  $\Phi 6-300$  mm is:

$$F_{static-relax} = (-846.37x^2(t) - 158.68x(t) + 20.4)P(t) \cdot 10^{-5} + 5511x^2(t) - 471.5x(t) - 1.635 \quad (A-5)$$

$$F_{static-excit} = (51.926x^2(t) - 131.122x(t) + 20.81)P(t) \cdot 10^{-5} + 1162.1x^2(t) - 137.9x(t) - 3.2 \quad (A-6)$$

### A.3 Static Model Verification

To verify this model, an experiment with a constant load is carried out. A load weighing  $40\text{ N}$  (totalling  $42.3\text{ N}$  with weight holders) was hung vertically on the free end of the  $\Phi 6-300$  mm PMA; the free end is also rigidly connected to a vertically mounted linear position transducer. The air supply to the PMA in this test is the same as the experimental schematic shown in Figure A-5. The test rig setup for this static model verification test is also illustrated in Figure A-5.

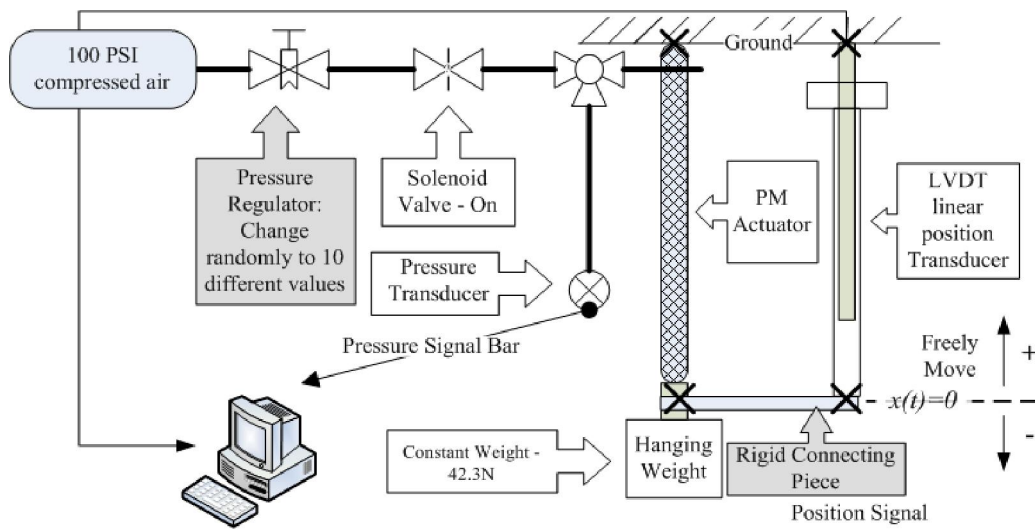


Figure A-5: Test rig setup for the static model verification test

In this experiment, the regulator was slowly adjusted to increase the pressure to an arbitrary value.

After the PMA and weights were stabilised under such pressure, the displacement and pressure were measured by linear transducer and pressure transducer, respectively. Ten different arbitrary pressure values and their corresponding stable displacements were reached in the experiment. Based on pressure and contraction length data, the force on the free end of the PMA is calculated from the static model equation. The calculated force results are presented in Table A-3, together with the measured contraction lengths and pressure values.

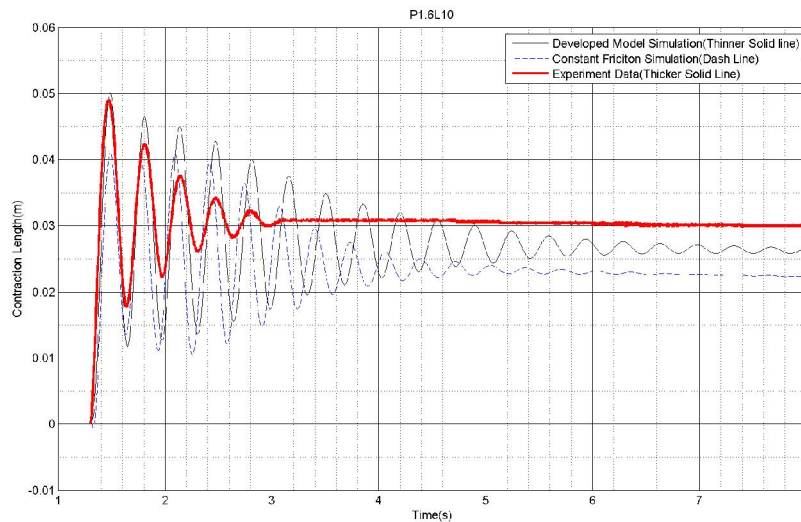
Table A-3: Verification results of the PMA quasi-static model

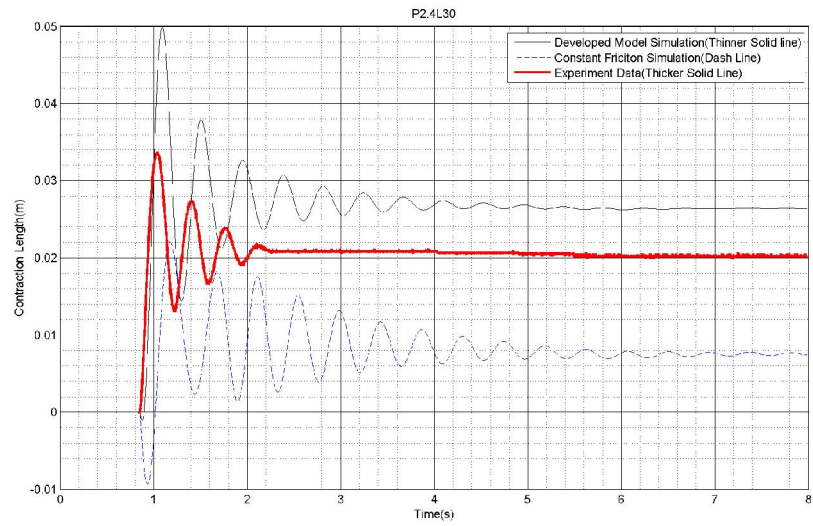
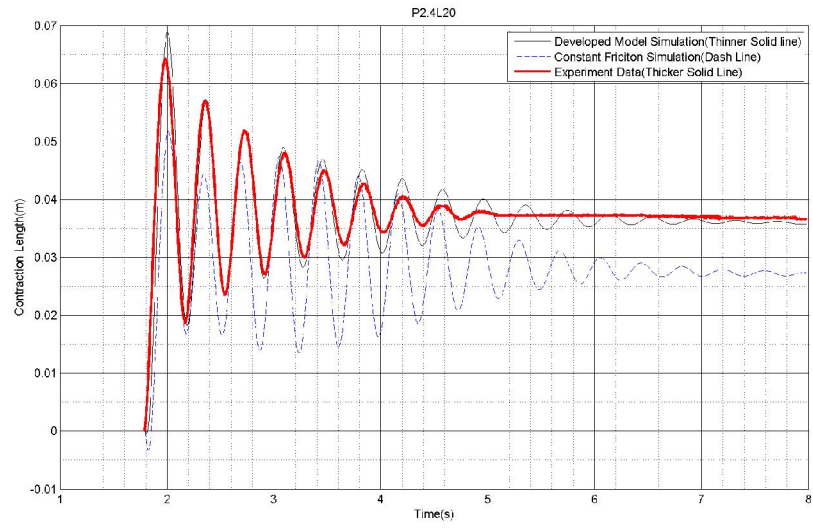
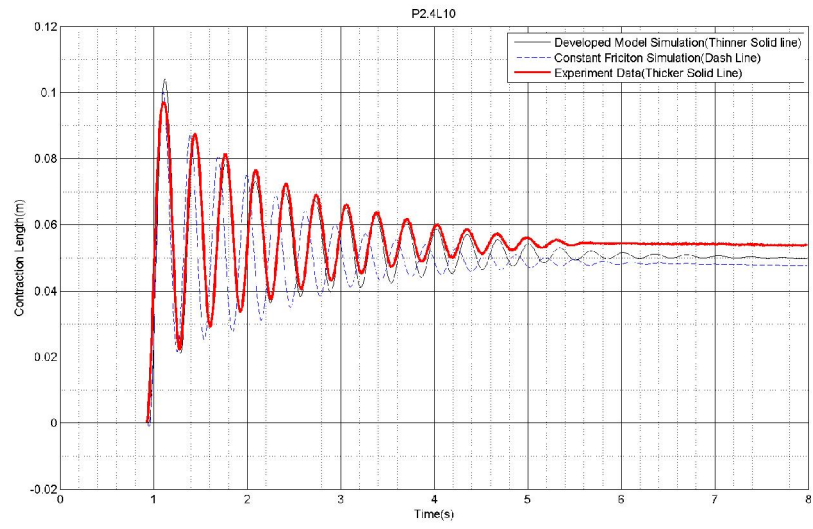
Contraction Length ( <i>mm</i> )	5.15	9.07	11.60	15.20	18.05	22.40	26.90	31.10	34.40	37.55
Pressure ( <i>Bar</i> )	2.30	2.561	2.69	2.86	2.99	3.17	3.43	3.61	3.81	3.99
Calculated force ( <i>N</i> )	41.34	43.18	43.56	43.66	43.60	42.96	43.27	42.38	42.07	41.66
Actual Weight ( <i>N</i> )	42.3 <i>N</i>									

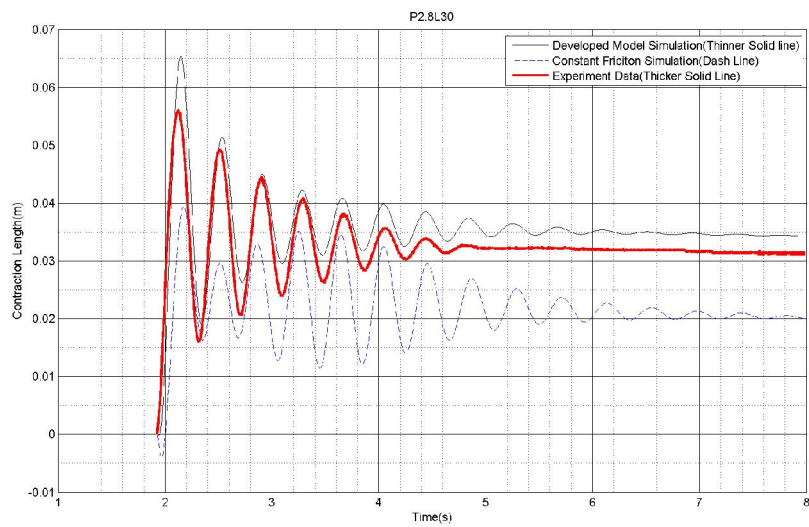
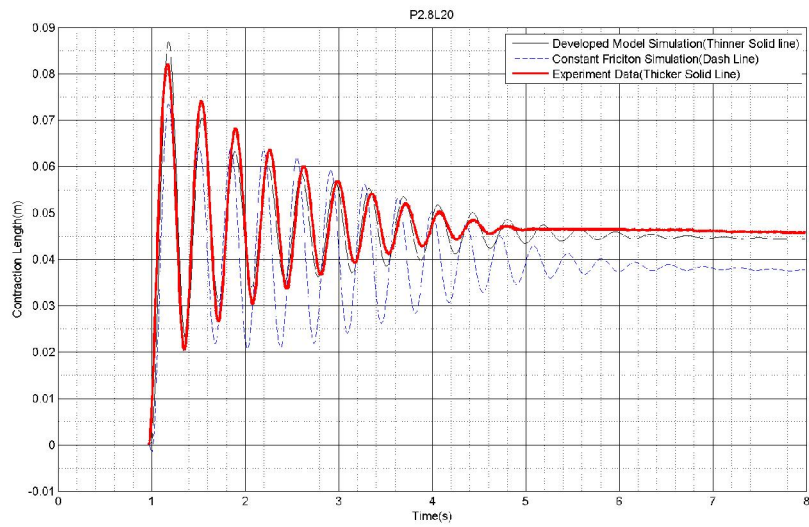
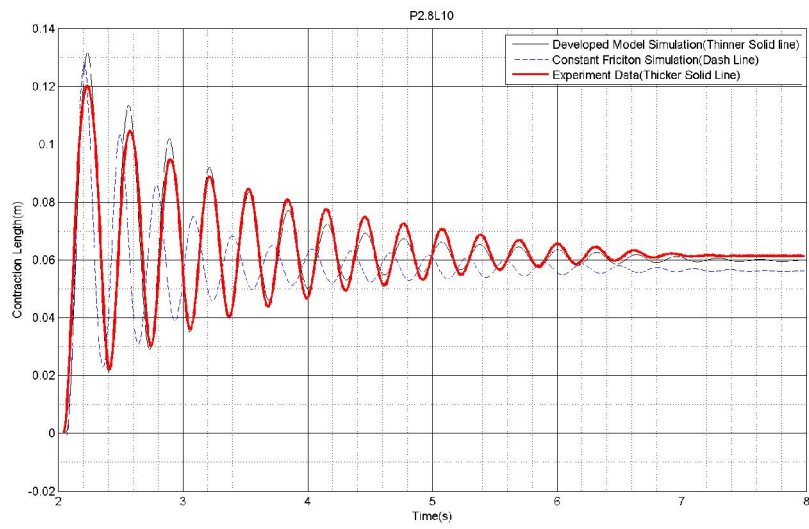
By comparing the calculated force from the model with actual load of 42.3 *N*, the results from the model are proven to be valid. The error between the mean force calculated from the model and the actual weight (42.3 *N*) is about 1.5% and the standard deviation is 1.42 *N*. This error is therefore acceptable. The standard deviation is relative large, which may be attributed by the use of a 2<sup>nd</sup> order polynomial regression. If a higher polynomial function is used, it will lead to higher accuracy. Furthermore, several other factors in the experiment could have contributed to the error, such as misalignment of the PMA, the error of the position transducer, and twisting at the free end of the PMA.

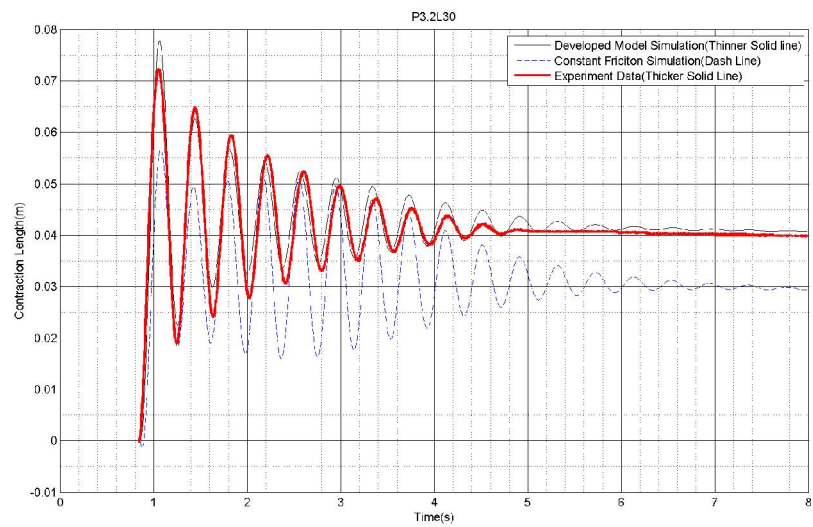
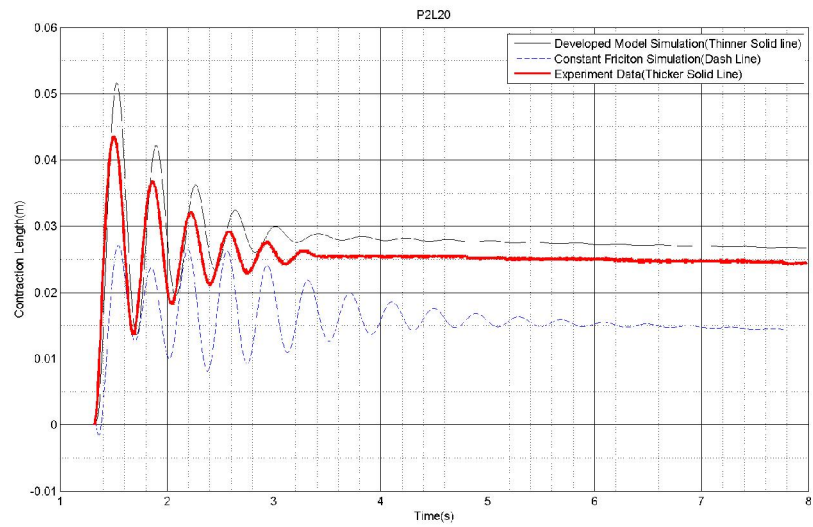
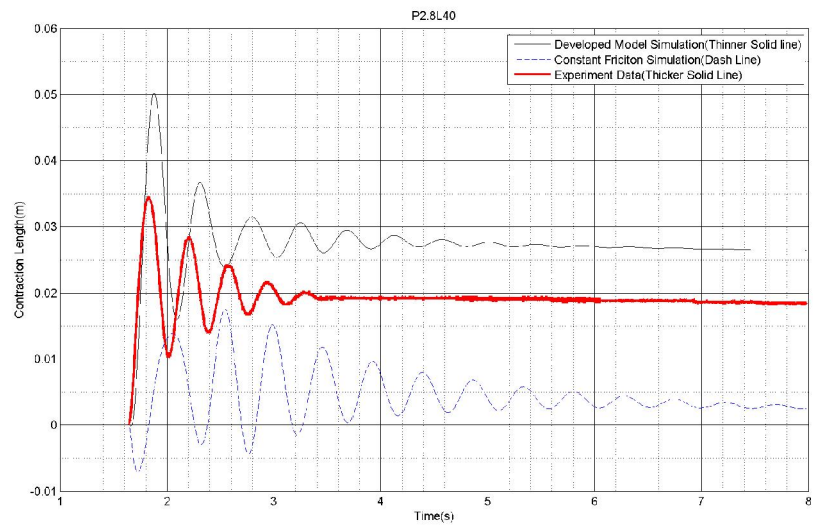
## Appendix B Estimation Results of the PMA's Dynamic Model

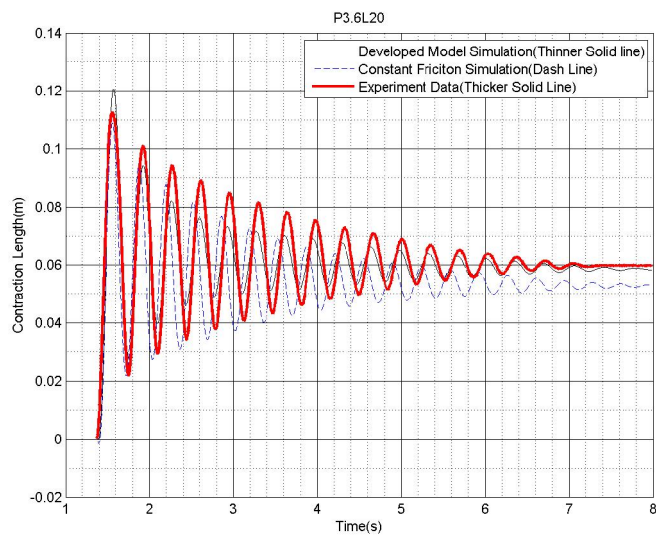
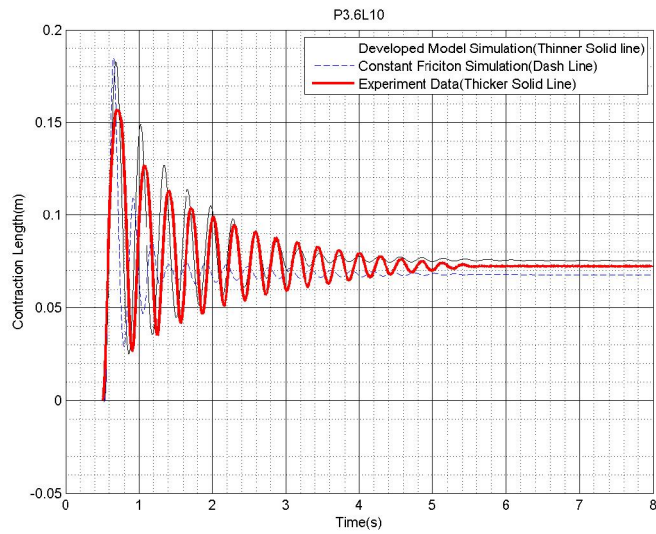
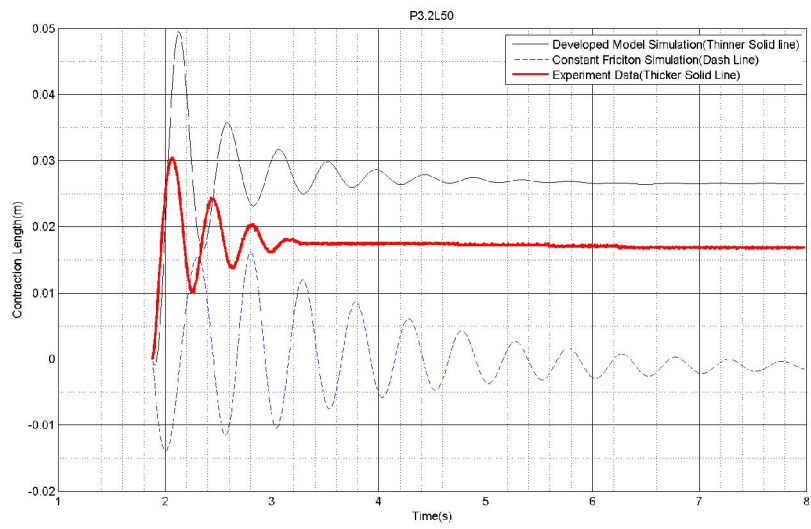
Appendix B presents the results of the instant compressed air flow input experiments for determining the coefficients ( $N_2, N_1, N_0, D_1, D_2$ ) of the PMA  $\Phi 6-300\text{ mm}$ . The experiment process is elaborated in Section 3.2. As was demonstrated, we used the least squares fitting approach to find the best group of coefficients ( $N_2, N_1, N_0, D_1, D_2$ ) that minimises the residuals between the experimental contraction length response  $x(t)$  and the simulation contraction length response based on the guessed group of ( $N_2, N_1, N_0, D_1, D_2$ ), calculated from the dynamic equation of motion (equation(3-22)). The groups of tests that achieve reasonable results in this series of experiment are all presented here in Appendix B. The figures in this Section shows the response in each group of test. The simulation contraction length response in comparison with experimental contraction length response, as well as the simulation from another form of dynamic model, in which the Coulomb friction element is  $2.5N$  are all displayed.

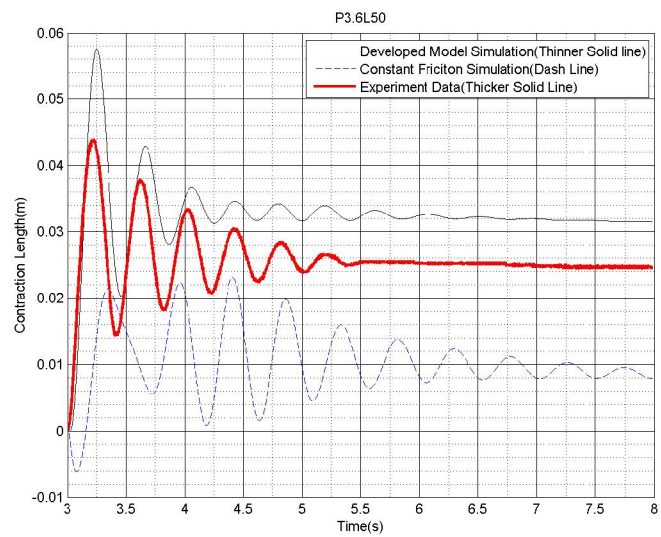
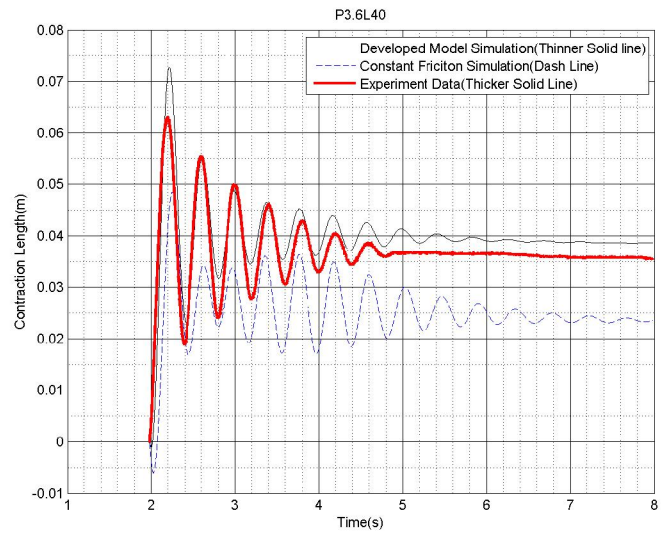
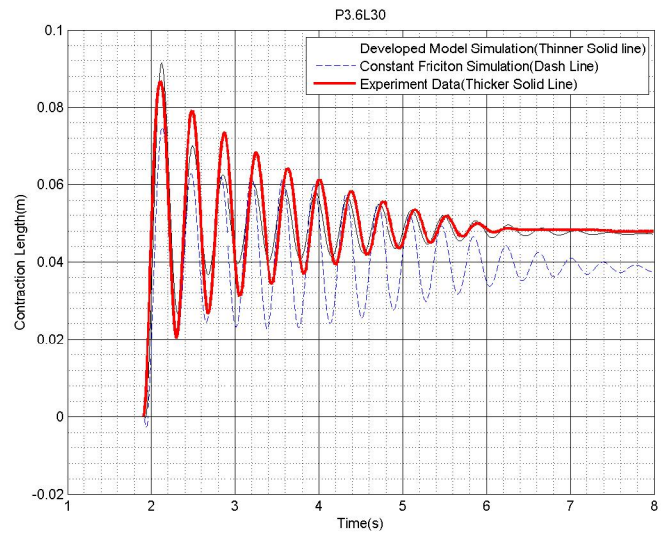


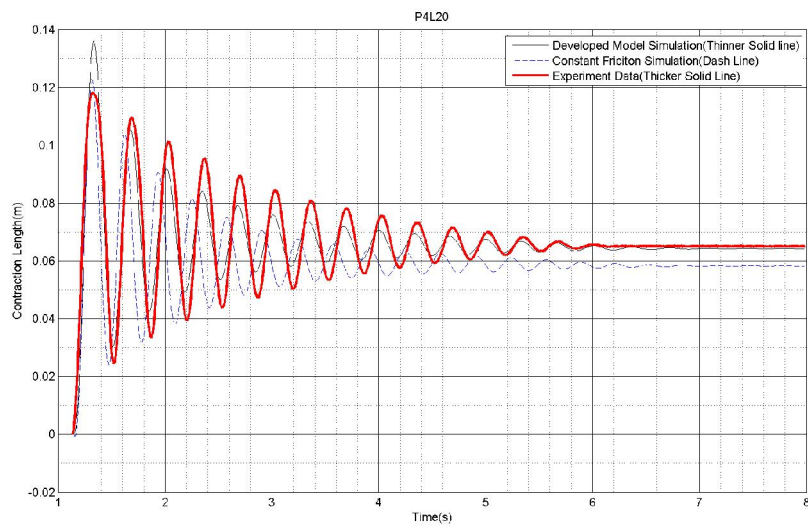
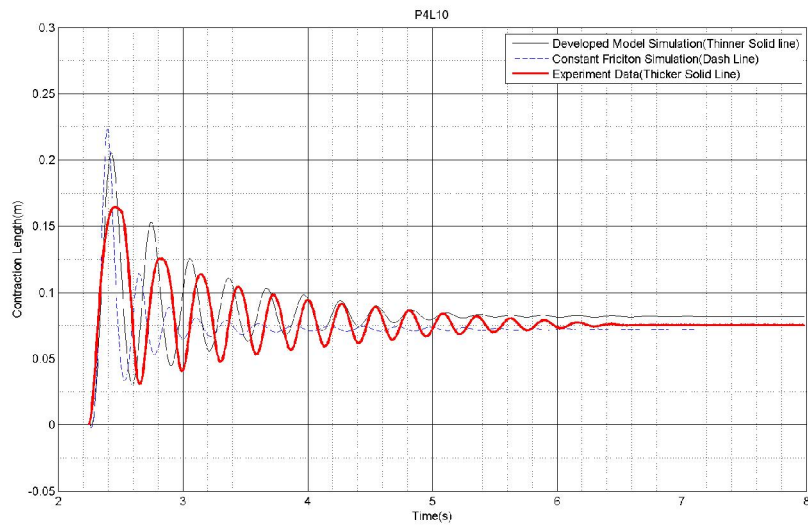
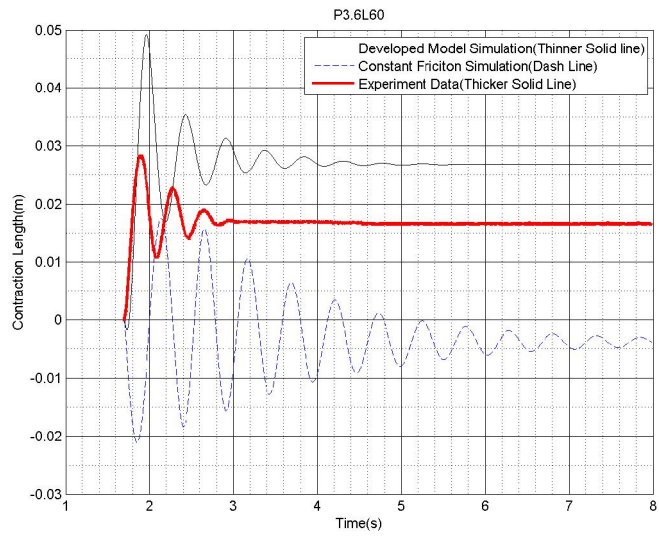


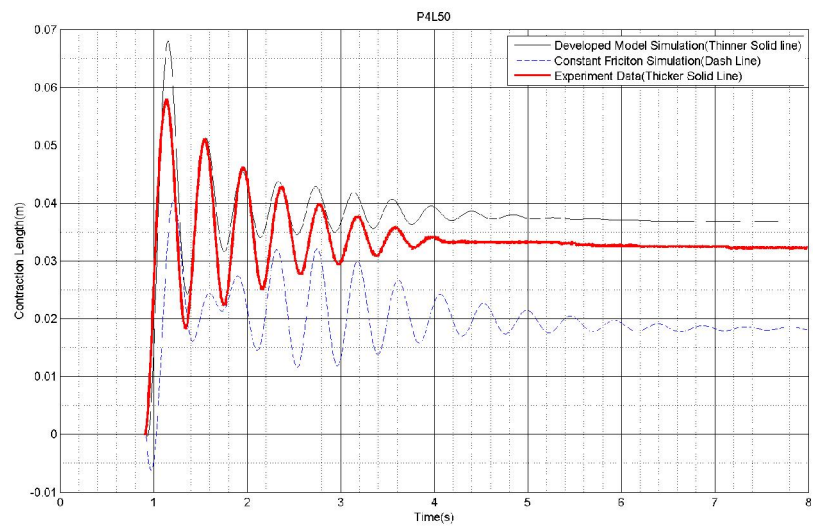
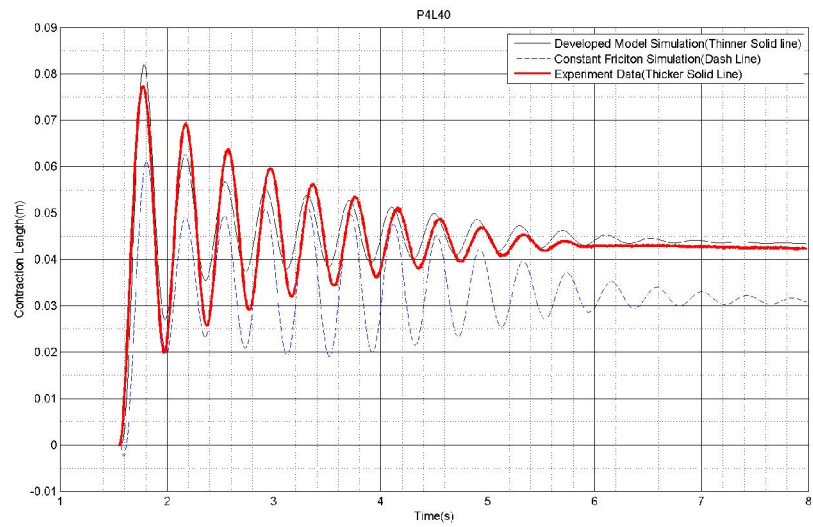
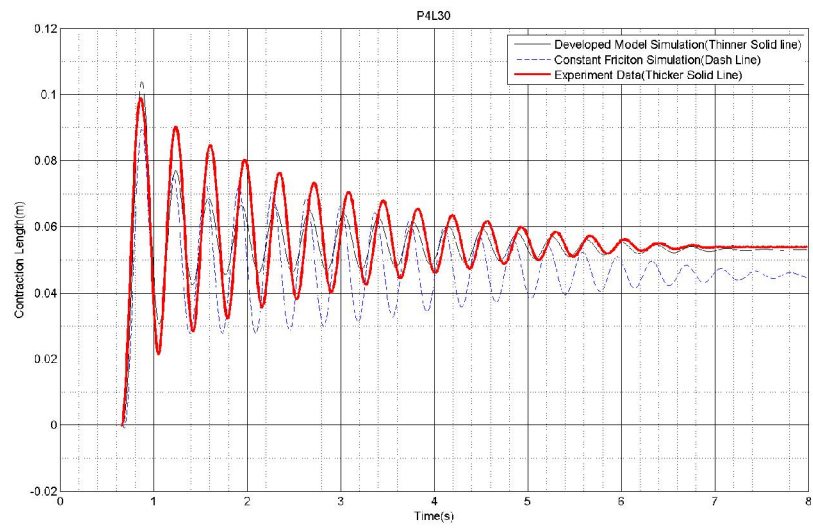












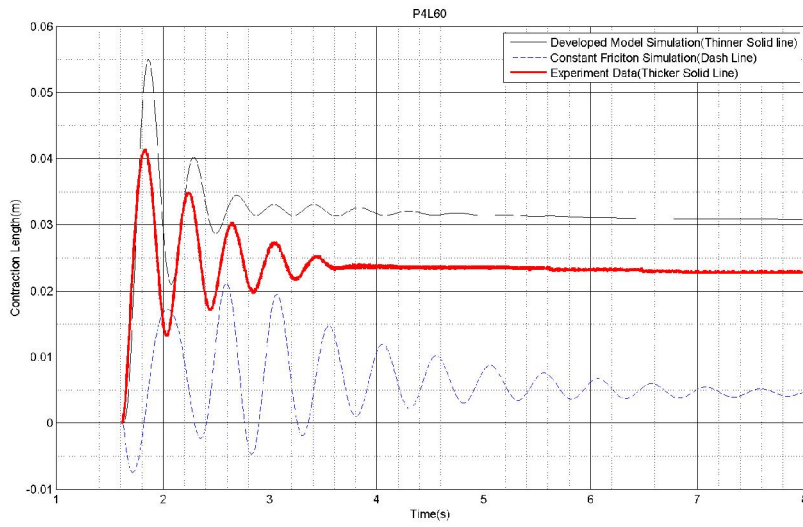


Table B-1: Fitted results of coefficients  $N_1, N_2, N_0, D_1$  and  $D_2$  from the experiment

$N_2, N_1, N_0$ , $D_1, D_2$	12.74N	22.74N	32.74N	42.74N	52.74N
1.6Bar	228.9342, -90.43, 6.87, -1.01, 0.80	/	/	/	/
2Bar	/	228.9342, -90.43, 6.87, -1.01, 0.80	/	/	/
2.4Bar	228.9342, -90.43, 6.87, -1.01, 0.80	228.9342, -90.43, 6.87, -1.01, 0.80	/	/	/
2.8Bar	228.9342, -90.43, 6.87, -1.01, 0.80	228.9342, -90.43, 6.87, -1.01, 0.80	228.9342, -90.43, 6.87, -1.01, 0.80	/	/
3.2Bar	228.9342, -90.43, 6.87, -1.01, 0.80	/	228.9342, -90.43, 6.87, -1.01, 0.80	/	/
3.6Bar	228.9342, -90.43, 6.87, -1.01, 0.80				
4Bar	228.9342, -90.43, 6.87, -1.01, 0.80				

The obtained coefficients ( $N_1, N_2, N_3, D_1$  and  $D_2$ ) by the least squares fitting approach are also displayed.

## Appendix C Workspace Optimisation for the 3UPU wrist Mechanism

Appendix C elaborates on the process of obtaining optimal geometric values for mechanical design so that the estimated workspace can reach maximum. The obtained values were not practically applied to the prototype in this thesis due to manufacturing limitations. However, the approach of workspace optimisation is still significant for designing prototypes in the future.

In order to design the *3UPU wrist* mechanism's geometry so that its workspace matches with the workspace of human activities of daily life (ADL), an optimisation was conducted. Appendix C presents a workspace volume evaluation index as the objective function of the optimisation. The selected geometric parameters and their anthropometric ranges are also presented. The conditions to determine whether a position is within a reachable workspace are introduced; and finally, the optimisation process and results are presented. The workspace performance of the *3UPU wrist* mechanism is evaluated by workspace volume, which is depicted as the proportion of reachable position of the mechanism in a given ADL range. It ranges from 0 to 1; the closer to 1, the greater it is that the generated workspace matches with the ADL workspace. Its mathematical form is expressed as:

$$\Phi(r_A, r_B, h_A, h_B, \alpha_{1A}, \alpha_{2A}, \alpha_{3A}) = \frac{\int_W dW}{W_{ADL}} \quad (C-1)$$

$W_{ADL}$  is the ADL workspace volume and is created based on the summarised ADL angle ranges of the shoulder joint (from Table 2-1), specifically,  $-110^\circ \sim 0^\circ$  for  $\theta_y$ ,  $-4^\circ \sim +96^\circ$  for  $\theta_x$ , and  $-85^\circ \sim +20^\circ$  for  $\theta_z$ . Arrays in equal increments of  $2^\circ$  within each rotation's angle range are generated, and the possible combinations of  $(\theta_x, \theta_y, \theta_z)$  from these arrays consist of the ADL workspace. In total, 19 656 configurations are generated.

The geometric parameters for the workspace index in Equation (C-1) are variables  $(r_A, r_B, h_A, h_B, \alpha_{1A}, \alpha_{2A}, \alpha_{3A})$ , which are the base plane radius, platform radius, their plane distances to rotation centre and the aligned angles of the universal joint on the *3UPU wrist* mechanism, respectively. Detailed geometric nomenclatures can be found in Section 4.1. Due to the numerous possibilities created by so many parameters, we applied parameter searching boundaries

for each parameter based on the anthropometric relationships in [112]. We assumed the height of the user as 1.7 m, and used the body section proportion relation to obtain the length of the upper limb, the width of shoulder and head and chest. Based on these dimensions, we created rough boundaries for the dimensions of the base and platform so that the exoskeleton will not interfere with the human. These boundaries are shown in Table C-1.

Table C-1: Boundaries of variables in workspace optimisation

Geometric parameters	$rA$	$rB$	$hA$	$hB$	$\alpha1A$	$\alpha2A$	$\alpha3A$
Boundary	50–180 mm	90–200 mm	41–60 mm	58–108 mm	$-20^\circ \sim 0^\circ$	$30^\circ \sim 60^\circ$	$90^\circ \sim 120^\circ$

The units of variables that were used were: millimetres for length and degrees for angles, in order that the magnitude of length and angles were approximately equal. As limited by practical manufacturing conditions, we presume variations smaller than 1 mm and  $1^\circ$  cannot be achieved, therefore, the minimum change in the variable is set as one (1) in the optimisation.

We also considered several constraint conditions in practically developing the exoskeleton. Firstly the angle restriction of the passive universal joints connected at the two ends of the actuator is discussed. To model the practical rotation range of universal joints, we studied one common type of off-the-shelf universal joint. Its clevis yokes mechanically interfere with each other, thus the two orthogonal revolute joints in the universal joint are actually constraining each other's rotating angle ranges. Its interference pattern is approximated as the following expression:

$$\begin{cases} 90^\circ - |\psi_y| \leq \psi_x \leq 90^\circ + |\psi_y| \\ -95^\circ \leq \psi_y \leq 95^\circ \end{cases} \quad (C-2)$$

In which,  $\psi_x$  and  $\psi_y$  are the two revolute joint rotation angles in the universal joint, and the ( $\psi_x = 0^\circ$ ,  $\psi_y = 0^\circ$ ) position is defined as the position where the two yokes of the universal joint are aligned with each other as a straight line. In the optimisation, this constraining pattern has been applied to all the six universal joints connected at the two ends of the limb actuator, expressed as ( $\theta_{xAi}$ ,  $\theta_{yAi}$ ,  $\theta_{xBi}$ ,  $\theta_{yBi}$ ,  $i = 1, 2, 3$ ).

The stroke of the actuators must also be considered. The stroke of a single PMA is within 75% to

105% of its nominal length. In practical operation, the PMA can achieve any length below 75% passively if it is not actuated; therefore, we only judge one pose to be infeasible if all PMAs are shorter than their 75% nominal length.

Given the reachable space conditions, the generated valid reachable poses are counted, and the sum of it proportional to the ADL workspace volume is maximised in the optimisation. Considering the comparatively large-scale problem size, the interior-point algorithm was used in Matlab™ function “Fmincon” to accomplish the parameter optimisation. We placed several groups of initial values near the boundaries of the parameter to obtain optimal results. The obtained optimal results were compared by their workspace volume. Finally, we selected the group with the best workspace performance. The following Figure C-1 illustrates the procedures of optimisation.

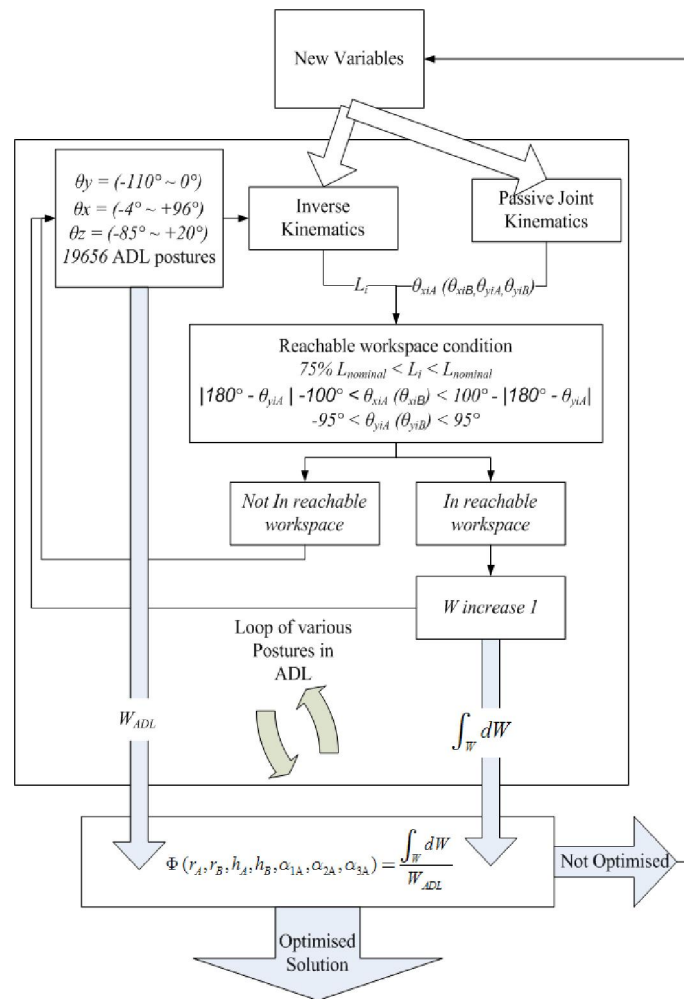


Figure C-1: Illustration of workspace optimisation procedures

The obtained optimisation results are listed in Table C-2.

Table C-2: Workspace optimisation results

<i>Geometric variables</i>	$rA$	$rB$	$hA$	$hB$	$\alpha1A$	$\alpha2A$	$\alpha3A$
<i>Optimisation results</i>	81.8 mm	95.3 mm	99.9 mm	81.8 mm	-4.7°	36.8°	115.2°

The optimised results lead to about 61.6% reachable workspace volume of the whole workspace. It is observed that when viewing on the same magnitude, the radius of the base and platform are the most insensitive parameters, and they are barely optimised from the initial values. The distance from the base to the rotation centre is optimised to be around 29 mm with multiple trials. The optimal distance from the platform to the rotation centre tends to favour a smaller value. Among the three angles for universal joint positions, the universal joint position in the middle is insensitive in this optimisation, and the other two angles tend to reach as far from the middle plane as possible.

As for presentation of the 3D rotational workspace, we used the presentation method introduced in [113]. Since sequential Euler angle coordinate does not exist in a vector space, this method transforms the Euler angle coordinate into a special workspace that visually indicates the attainable workspace [113]. Attained positions are plotted in Figure C-. This graphical representation is essentially a portion of a solid sphere with radius equal to  $\pi$ , and each solid point  $\omega$  within the sphere represents a rotation by the according angle  $||\omega||$  about the line passing from the origin through  $\omega$  [113]. The top, right and front views are presented as well. Following the Euler angle sequence  $Y-X-Z$ , we can observe that the obtainable positions are spanned all through rotation around the  $Y$ -direction, from  $-2/\pi$  to  $2/\pi$ . From the exoskeleton's point of view, it means that the robot is capable of acting in forward and backward flexion, as we know both are significant for tasks in daily activity. For rotation around  $X$ , the section from  $-2/\pi$  to  $0$  is far less than the section of  $(0, 2/\pi)$ ; this geometrically makes sense because moving the arm inwards towards the torso is not as useful as reach outwards on the side plane. Therefore, generally this optimal workspace volume matches a human's daily activity. Figure C- shows the workspace volume of initially selected non-optimal geometric parameters. The workspace volume proportion attained is about 25.3%. In this figure, we can observe evidently smaller volume.

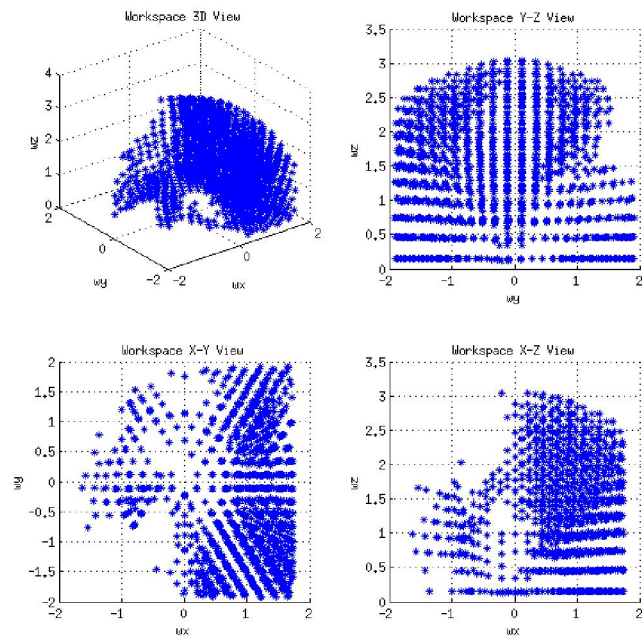


Figure C-2: Optimal workspace representation

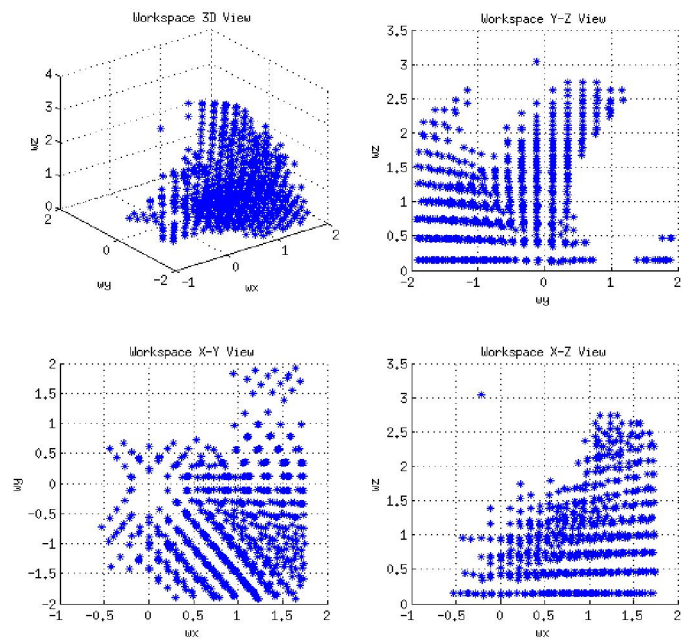


Figure C-3: Comparison of workspace volume

## Appendix D Shoulder Joint Reaction Force Analysis

When the shoulder joint assistive robot is implemented on a human shoulder, safety issues in mechanical design turn out to be quite essential for the *3UPU wrist* mechanism. For a parallel mechanism, one critical safety issue is the resultant reaction force transmitted from the mechanism onto the shoulder joint. In Appendix D we suggest a way of calculating the shoulder joint reaction force.

This topic has been addressed previously in [49], in which an *nSPS + S* parallel mechanism was integrated to assist a human upper limb. For explaining the *nSPS + S* parallel mechanism, please refer to Section 2.2.2 (Figure 2-4). In order to minimise the transmitted force from the platform to the shoulder joint and elbow joint, the author has derived an index containing expressions of the joint reaction forces and torques. By performing a minimisation optimisation, the optimal group of cable forces that generates the least joint reaction forces and torques can be obtained. In the first subsection, we first briefly reviewed the inverse dynamic and reaction force of the *3SPS + S* mechanism, so that by comparison, the case of applying the *3UPU wrist* mechanism on a shoulder joint is clearly demonstrated. Then we derived the reaction force analysis for the *3UPU wrist* mechanism application on the shoulder joint in the static case. Finally, we discussed the case of using cable-like elastic actuators to drive the *3UPU wrist* mechanism and case studied the proposed numeric approach to obtain all tension forces for redundant actuators.

### D.1 Reaction Force Review of *3SPS + S* Mechanism

Figure D-(a) illustrates a schematic *3SPS + S* design installed on two spherical joint-connected dummy parts. The immobile dummy part represents the torso, while the movable dummy part represents the upper arm. The base of the *3SPS + S* mechanism is securely attached to the torso, while the platform of the mechanism is fixed to the upper arm. Consequently, we regard the platform of the *3SPS + S* mechanism and the upper arm dummy as one integrated component in the force analysis, which is called the ‘moving part’, and the rest of the model is regarded as the ‘immobile part’. The moving part is then connected to the immobile part by the four spherical joints (Figure D-(b)).

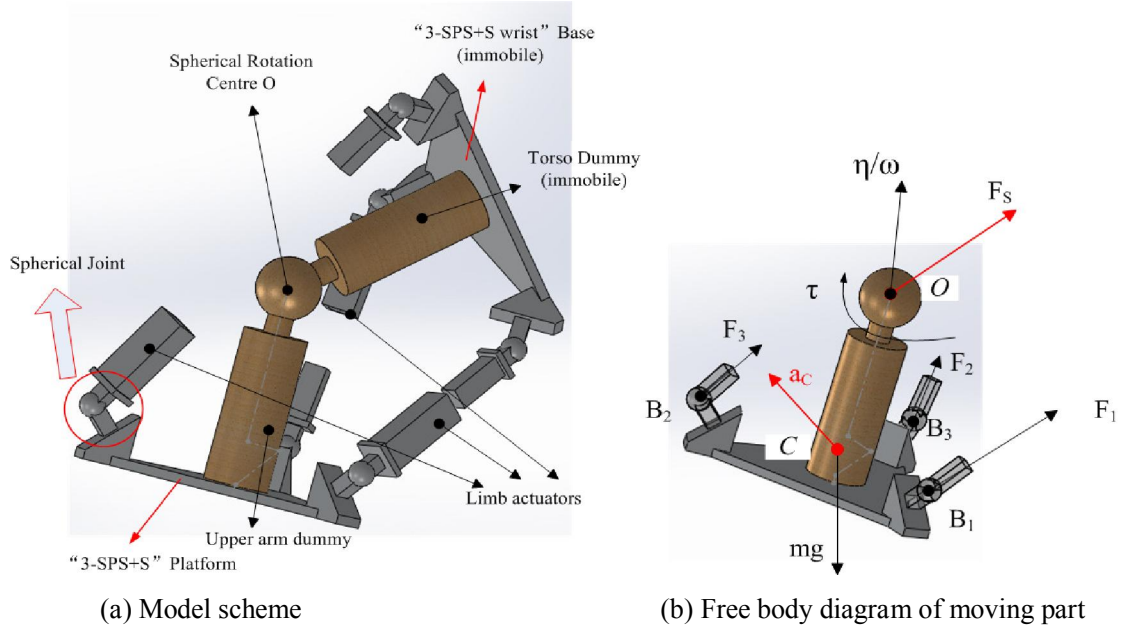


Figure D-1: Reaction force analysis model for the 3SPS + S wrist mechanism

Suppose the moving part is at the rotation angles of  $(\theta_x, \theta_y, \theta_z)$ , while the angular velocity and angular acceleration of the moving parts are  $\bar{\omega}$  and  $\bar{\eta}$ , respectively. According to the free body diagram analysis in Figure D-(b), we obtained the following Euler-Newton equations in the global coordinate frame (coordinate frame  $\{O_A\}$ ).

$$m\bar{a}_C = \sum_i \bar{F}_i + mg\bar{C} - \bar{F}_s \quad (i=1,2,3) \quad (D-1)$$

$$I \cdot \bar{\eta} + \bar{\omega} \times I \cdot \bar{\omega} = \sum_i \bar{B}_i \times \bar{F}_i - \bar{M}_e \quad (i=1,2,3) \quad (D-2)$$

In Equation (D-2), the moment centre is  $O$ . In Equations (D-1) and (D-2),  $m$  and  $I$  denote the mass and inertia matrix of the moving part.  $\bar{C}$ ,  $\bar{V}_C$ ,  $\bar{a}_C$  denote the position, velocity and acceleration at the centre of mass, respectively.  $\bar{B}_i$  and  $\bar{A}_i$  are the universal joint centres on the platform and base respectively, and  $\bar{F}_i$  is the actuator force vector on each platform universal joint.  $\bar{F}_s$  is the reaction force from the spherical shoulder joint on the upper arm.  $\bar{M}_e$  is the external torque applied to the shoulder joint  $O$ .

Since the rotation angles  $(\theta_x, \theta_y, \theta_z)$  are known, the position of  $C, B_i$  and inertia matrix are obtained

as:

$$\bar{C} = \bar{C}^{\{O_A\}} = R(\theta_x, \theta_y, \theta_z) \bar{C}^{\{O_B\}} \quad 7 \quad (D-3)$$

$$\bar{B}_i = \bar{B}_i^{\{O_A\}} = R(\theta_x, \theta_y, \theta_z) \bar{B}_i^{\{O_B\}} \quad (i = 1, 2, 3) \quad (D-4)$$

$$\mathbf{I} = \mathbf{I}^{\{O_A\}} = R(\theta_x, \theta_y, \theta_z) \mathbf{I}^{\{O_B\}} R^T(\theta_x, \theta_y, \theta_z) \quad (D-5)$$

$$\bar{F}_i = f_i \cdot (\bar{A}_i - \bar{B}_i) = f_i \cdot (\bar{A}_i - R(\theta_x, \theta_y, \theta_z) \bar{B}_i^{\{O_B\}}) \quad (i = 1, 2, 3) \quad (D-6)$$

Substituting these equations into Equation (D-2), the actuator forces  $f_i$  can then be uniquely determined, providing that the mechanism is not at a singular pose.

According to (D-1),  $\bar{F}_s$  is expressed as:

$$\bar{F}_s = \sum_i \bar{F}_i + mg\bar{C} - m\bar{a}_c \quad (i = 1, 2, 3) \quad (D-7)$$

Since both  $\bar{F}_i$  and  $\bar{C}$  are determined, the acceleration at mass centre is calculated as:

$$\bar{a}_c = \dot{\bar{V}}_c = -\dot{\bar{\omega}} \times \bar{C} - \bar{\omega} \times \bar{V}_c = -\bar{\eta} \times \bar{C} + \bar{\omega} \times (\bar{\omega} \times \bar{C}) \quad (D-8)$$

Then the reaction force is obtained. In static cases, where  $\bar{\omega} = \mathbf{0}$ ,  $\bar{\eta} = \mathbf{0}$ , the shoulder joint reaction force is:

$$\bar{F}_s = \sum_i \bar{F}_i + mg\bar{C} \quad (i = 1, 2, 3) \quad (D-9)$$

In which the actuator forces are calculated in:

$$\sum_i \bar{B}_i \times \bar{F}_i = \bar{M}_e \quad (i = 1, 2, 3) \quad (D-10)$$

## D.2 Reaction Force Analysis of 3UPU Wrist Mechanism

In the 3UPU wrist mechanism, as opposed to the 3SPS + S mechanism, universal joints rather than spherical joints are used to connect the prismatic actuators to the base and platform. Therefore, besides the force ( $\overline{F}_i$ ) transmitted to the centre of the universal joint (e.g. joint  $B_i$ ), a moment couple ( $\overline{M}_{B_i}$ ) that is perpendicular to the revolute joint pair axes ( $\overline{X}_{B_i}$ ,  $\overline{Y}_{B_i}$ ) is also applied on the universal joint. Figure D-2 provides an illustration of the forces on a spherical joint and the force and moment applied on a universal joint.

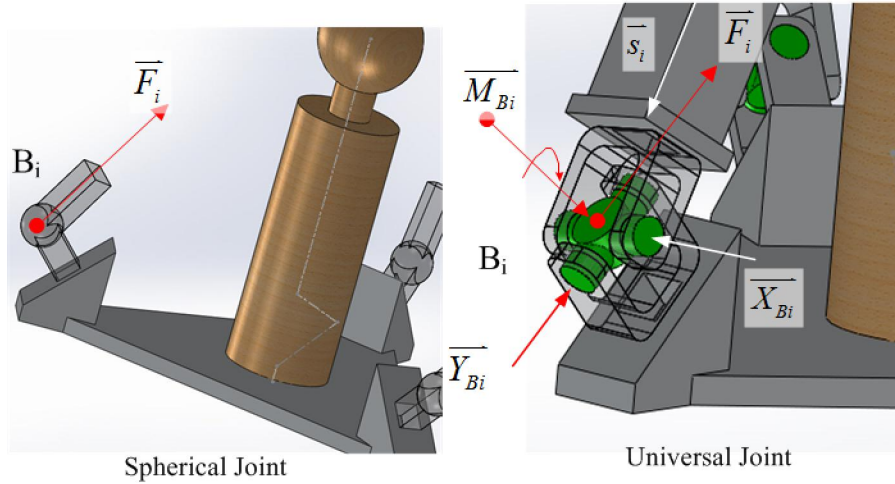


Figure D-2: Force and moments applied on a spherical joint and universal joint

Unit vectors  $\overline{X}_{B_i}$  and  $\overline{Y}_{B_i}$  represent the directions of the cross-component at the centre of the universal joint. In comparison with the definition of axes in the local coordinate frame  $\{A_i: X_{A_i} Y_{A_i} Z_{A_i}\}$  ( $\{B_i: X_{B_i} Y_{B_i} Z_{B_i}\}$ ) defined in Section 4.1,  $\overline{Y}_{B_i}$  is pointing from  $B_i$  to  $O$ .  $\overline{X}_{B_i}$  is in the direction of the other revolute axis, and according to the geometric condition of the 3UPU wrist mechanism, it is in parallel with the revolute axis in the universal joint positioned at  $A_i$  (Figure D-3). Thus, we define:

$$\overline{X}_{A_i} = \overline{X}_{B_i} \quad (i = 1, 2, 3) \quad (\text{D-11})$$

In which  $\overline{X}_{A_i}$  is defined in the direction that the cross-product  $\overline{X}_{A_i} \times \overline{Y}_{A_i}$  is pointing to the

platform, and  $\bar{s}_i$  is the unit vector denoting the limb's direction.

$$\bar{s}_i = \frac{\bar{B}_i - \bar{A}_i}{|\bar{B}_i - \bar{A}_i|} = \frac{\bar{B}_i - \bar{A}_i}{l_i} \quad (i = 1, 2, 3) \quad (\text{D-12})$$

Twist moment  $\bar{M}_{Bi}$  is generated by the twisting forces inside the connected linear actuators that do not align with the universal joints' rotation orientation. Therefore, it is perpendicular to both revolute axes.

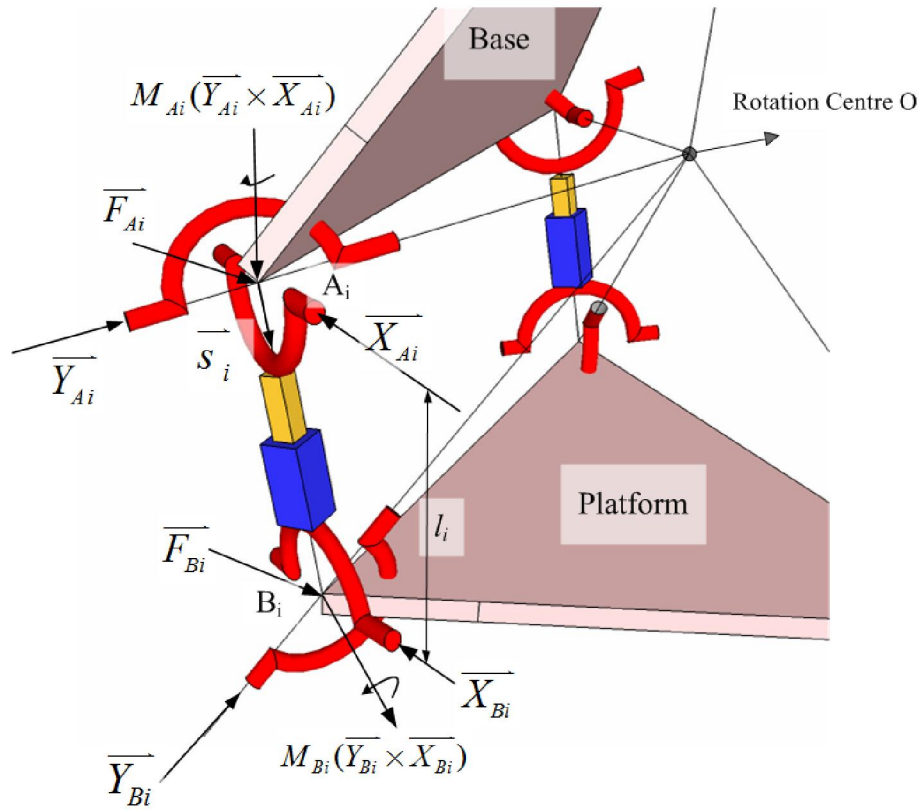
$$\bar{M}_{Bi} = M_{Bi} \bar{Y}_{Bi} \times \bar{X}_{Bi} \quad (\text{D-13})$$

To study the forces and moments in the *3UPU wrist* mechanism, Gregorio [98] has firstly studied each single limb and developed corresponding equilibrium equations of them in the static case (Equations (D-14) and (D-15)) based on the free body diagram of the *i*th limb illustrated in Figure D-.

$$\bar{F}_{Bi} + \bar{F}_{Ai} = 0 \quad (i = 1, 2, 3) \quad (\text{D-14})$$

$$(\bar{B}_i - \bar{A}_i) \times \bar{F}_{Bi} + M_{Ai} (\bar{Y}_{Ai} \times \bar{X}_{Ai}) + M_{Bi} (\bar{Y}_{Bi} \times \bar{X}_{Bi}) = 0 \quad (i = 1, 2, 3) \quad (\text{D-15})$$

In Equation (D-15), the moment centre is point  $A_i$ .


 Figure D-3: Free body diagram for the  $i$ th limb in the 3UPU wrist mechanism

Dot multiplying both sides of Equation (D-15) by  $\overline{X_{Ai}}$  and substituting Equations (D-14) and (D-11) into the results, Gregorio obtained the following results, which demonstrate that  $\overline{F_{Bi}}$  is in the plane of  $\overline{X_{Ai}}$  and  $(\overline{B_i} - \overline{A_i})$ :

$$\overline{F_{Bi}} \cdot (\overline{B_i} - \overline{A_i}) \times \overline{X_{Ai}} = 0 \quad (i=1,2,3) \quad (\text{D-16})$$

Therefore, the applied force on the platform universal joint  $\overline{F_{Bi}}$  is expressed as:

$$\overline{F_{Bi}} = f_i \overline{s_i} + g_i \overline{X_{Ai}} \quad (i=1,2,3) \quad (\text{D-17})$$

Where  $\overline{s_i}$  is the unit vector of the limb vector, and  $f_i$  and  $g_i$  are unknown scalars and need to be determined.

Moment scalars  $M_{Bi}$  are solved by substituting Equation (D-17) into Equation (D-15), as:

$$M_{B_i} = g_i |OB_i| \quad (i = 1, 2, 3) \quad (D-18)$$

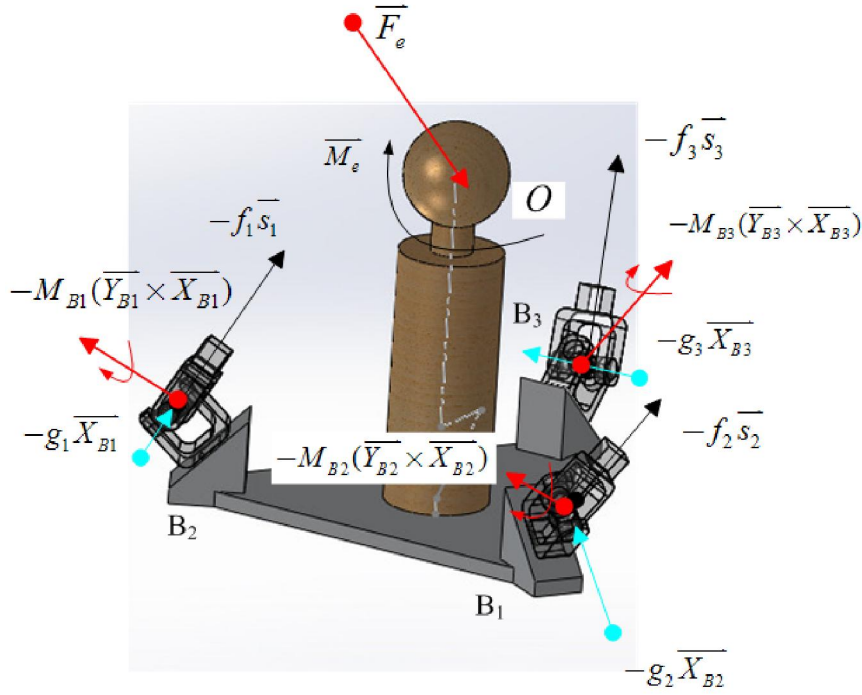


Figure D-4: Free body diagram of the 3UPU wrist mechanism assisted arm in static status

Applying the reaction force and moment of each limb on the platform, we obtained the moving component's free body diagram as illustrated in Figure D-, and the following equilibrium equations are obtained:

$$\sum_{i=1}^3 f_i \bar{s}_i + \sum_{i=1}^3 g_i \bar{X}_{B_i} = \bar{F}_e \quad (i = 1, 2, 3) \quad (D-19)$$

$$\sum_{i=1}^3 \bar{B}_i \times f_i \bar{s}_i + \sum_{i=1}^3 \bar{B}_i \times g_i \bar{X}_{B_i} + \sum_{i=1}^3 M_{B_i} (\bar{Y}_{B_i} \times \bar{X}_{B_i}) = \bar{M}_e \quad (i = 1, 2, 3) \quad (D-20)$$

In Equation (D-19), the moment centre is point  $O$ , and  $\bar{F}_e$  and  $\bar{M}_e$  are the external force and external moment applied relative to point  $O$ .

Introducing Equation (D-18) into Equation (D-20), we obtain:

$$\sum_{i=1}^3 f_i |OB_i| \bar{s}_i \times \bar{Y}_{Bi} = \bar{M}_e \quad (i = 1, 2, 3) \quad (D-21)$$

So we can obtain  $f_i$  as:

$$f_i = \frac{M_e \cdot \bar{X}_{Aj} \times \bar{X}_{Ak}}{|OB_i| \bar{s}_i \times \bar{Y}_{Bi} \cdot \bar{X}_{Aj} \times \bar{X}_{Ak}} \quad (i, j, k = 1, 2, 3; i \neq j; j \neq k; i \neq k) \quad (D-22)$$

Then the actuator forces are determined. We firstly assume that the *3UPU wrist* mechanism and the upper arm dummy are not articulated with the immobile part by the spherical joint with centre  $O$ .

Then the external force would be gravity only. In this case:

$$\bar{F}_e = m\bar{g} \quad (D-23)$$

$$\bar{M}_e = \overline{COG} \times m\bar{g} \quad (D-24)$$

Where  $\overline{COG}$  is the position of the mass centre.

Substitute Equations (D-22) and (D-23) into Equation (D-19), then  $g_i$  can be determined:

$$\begin{cases} g_i = \frac{N \cdot \bar{X}_{Bj} \times \bar{X}_{Bk}}{\bar{X}_{Bi} \cdot \bar{X}_{Bj} \times \bar{X}_{Bk}} \\ N = m\bar{g} - \sum_{i=1}^3 f_i \bar{s}_i \end{cases} \quad (i, j, k = 1, 2, 3; i \neq j; j \neq k; i \neq k) \quad (D-25)$$

Substitute the results of Equations (D-25) and (D-22) into Equation (D-17), then at this static position, the reaction force transmitted from the universal joints ( $\bar{F}_{Bi}$ ) on the platform are solved.

However, in practical circumstances, since the moving part is still interfering with the shoulder spherical joint, the shoulder reaction force produced on the interfering surface should also be considered as contributing to the external force.

$$\bar{F}_e = \bar{F}_s + m\bar{g} \quad (D-26)$$

Substituting Equation (D-26) into Equation (D-19), we obtain:

$$\overline{F}_s - \sum_{i=1}^3 \overline{g}_i \overline{X}_{Bi} = \sum_{i=1}^3 \overline{f}_i \overline{s}_i - \overline{m} \overline{g} \quad (D-27)$$

In which, we have six undetermined passive force scalars ( $F_{sx}$ ,  $F_{sy}$ ,  $F_{sz}$ ,  $g_1$ ,  $g_2$ ,  $g_3$ ) on the left side of the equation. Derived from Equation (D-27), we obtain three equations:

$$\begin{cases} F_{sx} - \sum_{i=1}^3 g_i X_{Bix} = \sum_{i=1}^3 f_i s_{ix} - mg_x \\ F_{sy} - \sum_{i=1}^3 g_i X_{Biy} = \sum_{i=1}^3 f_i s_{iy} - mg_y \\ F_{sz} - \sum_{i=1}^3 g_i X_{Biz} = \sum_{i=1}^3 f_i s_{iz} - mg_z \end{cases} \quad (D-28)$$

The reaction force is solved as:

$$F_s = \begin{pmatrix} \sum_{i=1}^3 g_i X_{Aix} - mg_x + \sum_{i=1}^3 f_i s_{ix} \\ \sum_{i=1}^3 g_i X_{Aiy} - mg_y + \sum_{i=1}^3 f_i s_{iy} \\ \sum_{i=1}^3 g_i X_{Aiz} - mg_z + \sum_{i=1}^3 f_i s_{iz} \end{pmatrix} \quad (D-29)$$

The  $3SPS + S$  mechanism can be considered as a special case of the  $3UPU$  wrist mechanism applied on a human shoulder joint, where there are no forces in the direction of  $\overline{X}_{Ai}$  because it would immediately transform into torques, in other words,  $g_i = 0$ , and the obtained shoulder reaction forces are:

$$F_s = \begin{pmatrix} -mg_x + \sum_{i=1}^3 f_i s_{ix} \\ -mg_y + \sum_{i=1}^3 f_i s_{iy} \\ -mg_z + \sum_{i=1}^3 f_i s_{iz} \end{pmatrix} \quad (D-30)$$

This is consistent with the result in Equation (D-10) obtained in the beginning of this section.

Therefore, the reaction force cannot be solved until  $g_i$  ( $i = 1, 2, 3$ ) are determined.

Assuming we have a *3UPU wrist* mechanism installed on the shoulder, staying at the position denoted by the Euler angle of  $(\theta_x = 2\pi/7, \theta_y = 1\pi/4, \theta_z = -\pi/3)$ , the geometry of the mechanism, namely  $A_i$  and  $B_i^{\{OB\}}$  is expressed as:

$$\begin{cases} A_1 = (0.13 & -0.05 & 0)^T \\ A_2 = (0.05 & -0.05 & 0.12)^T \\ A_3 = (-0.12 & -0.05 & 0.05)^T \end{cases} \quad \begin{cases} B_1^{\{OB\}} = (0.05 & 0.05 & -0.1)^T \\ B_2^{\{OB\}} = (0.05 & -0.05 & -0.1)^T \\ B_3^{\{OB\}} = (-0.05 & -0.05 & -0.1)^T \end{cases} \quad (D-31)$$

Which are in units of metres. The total mass of the platform and the upper limb is 2 kg. The centre of mass  $\overline{COG}^{\{OB\}}$  is assumed as  $(0, 0.01, -0.12)^T$ .

Firstly, by substituting these model constants in this example into Equation (D-22), we obtain actuator forces  $f_i$  ( $i = 1, 2, 3$ ) as:

$$f_1 = 9.51\text{N}, f_2 = 25.6\text{N}, f_3 = 19.8\text{N} \quad (D-32)$$

Then the shoulder reaction force  $\overline{F}_{s0}$  when applying the *3SPS + S* mechanism is calculated from Equation (D-10) as:

$$\overline{F}_{s0} = (1.4\text{N}, 34.3\text{N} \ -36.35\text{N})^T \quad (D-33)$$

The objective function is expressed as the proportion of the shoulder reaction force when applying the *3UPU wrist* mechanism on a shoulder to the calculated shoulder reaction force when applying the *3SPS + S* mechanism.

$$\Gamma = \frac{|F_s|}{|F_{s0}|} \quad (D-34)$$

By using numeric methods to find the optimal group of  $g_i$  ( $i = 1, 2, 3$ ) values that minimises the objective function, we obtained the following results:

$$g_1 = -137.2 \text{ N}, g_2 = -13.5 \text{ N}, g_3 = -128.6 \text{ N} \quad (\text{D-35})$$

And the resultant reaction force is:

$$\bar{F}_{s-optimal} = (125.6, -2.5, -36.8) \times 10^{-6} \text{ N} \quad (\text{D-36})$$

which is close to zero.

In this numeric method, the values of  $g_i$  ( $i = 1, 2, 3$ ) can also be constrained according to various restrictions. For example, if we assume that  $g_i$  ( $i = 1, 2, 3$ ) should be no larger than  $f_i$  ( $i = 1, 2, 3$ ), applying this restriction, the following results are obtained:

When  $g_1 = -9.5 \text{ N}$ ,  $g_2 = 25.6 \text{ N}$  and  $g_3 = 19.8 \text{ N}$ , the optimal reaction force is  $|\bar{F}_{s-optimal}| = 34.8 \text{ N}$

and  $|\bar{F}_{s0}| = 50 \text{ N}$ .